Optimized magnetic resonance spectroscopy of 2-hydroxyglutarate

Master Thesis in Medical Technology
by
Celine Marie Bakken Skramstad

Department of Chemistry
University of Bergen, Norway

June 2024

Supervisor: Assoc. Prof. John Georg Seland

Acknowledgements

I wish to extend my sincerest gratitude to my supervisor, Assoc. Prof. John Georg Seland, at the Department of Chemistry, University of Bergen, for his invaluable guidance and support throughout this research project, and for introducing me to this project and the field of MRS.

I would like to thank Lars Ersland for his guidance on the 3T GE scanner and his continuous encouragement throughout the project. I am also grateful to Alexander R. Craven for his assistance and guidance with the analysis tools, LCModel and Osprey. Additionally, I would like to thank Assoc. Prof. Nils Åge Frøystein for providing the Python simulation script for the 1D spectra and for his guidance on the 60 MHz Nanalysis. My gratitude also goes to Morten Kristoffersen and Rolf Arne Haakonsen at the Medical Technology Department at Haukeland University Hospital for their help with the 3D printing, and the radiographers at the Department of Radiology at Haukeland University Hospital.

I am deeply grateful to my family and friends for their unwavering support, ideas, and encouragement, and to my twin brother Theodor for the sense of togetherness that has kept me motivated.

Lastly, I am thankful for the knowledge and skills I have acquired during this process. This journey has been incredibly rewarding, and I am grateful for the opportunities it has provided for my personal and professional growth.

Celine M. B. Skramstad
Bergen, 02.06.2024

Scientific environment

The work done in this study is carried out at NNP, the Department of Chemistry at the University of Bergen, and at the Radiology Department at Haukeland University Hospital (HUS) [47, 38, 37].

The work and results from the 600 MHz instrument were partly supported by the Bergen Research Foundation, Sparebankstiftinga Sogn og Fjordane, and the Research Council of Norway through the Norwegian NMR Platform, NNP (226244/F50).

The work and results from the 850 MHZ instrument were partly supported by the Research Council of Norway through the Norwegian NMR Platform, NNP (226244/F50).

The work and the results accumulated from the 3T GE scanner at Haukeland University Hospital were supported by Haukeland University Hospital and its Medical Technology Department.

Abstract

In recent years, non-invasive detection of 2-hydroxyglutarate (2HG) using ^1H-MRS has emerged as a promising method for differentiating IDH mutant and wild-type brain tumors. However, reliable detection and quantification of 2HG remain challenging due to its MR spectrum, which consists of five non-interchangeable protons at 4.02 ppm, 2.27 ppm, 2.22 ppm, 1.98 ppm, and 1.83 ppm, complex J-coupling patterns, and strong overlap with signals from other brain metabolites. There is currently no consensus on the optimal pulse sequence, spectral editing techniques, and corresponding spectral parameters for 2HG detection. Short-TE PRESS, MEGA-PRESS, sLASER, and MEGA-sLASER have been identified as the most promising pulse sequences. However, recommendations for echo times and other spectral parameters to optimize 2HG quantification remain unclear, particularly given the impact of higher-order J-couplings, which vary with magnetic field strength.

This thesis investigates the spectroscopic parameters required for optimal detection of 2HG by measuring the spectra of 2HG phantoms at magnetic field strengths of 60 MHz, 500 MHz, and 600 MHz, as well as using a 3T GE scanner for phantom studies. The study examines different pulse sequences (with and without spectral editing) and varying echo times to thoroughly explore the complex J-coupling patterns and their dependence on echo time and magnetic field strength. The results provide insights into choosing the optimal ^1H-MRS method for 2HG quantification and how to determine appropriate basis sets for spectral fitting.

Comprehensive spectral analysis tools, including TopSpin, LCModel, and Osprey, are used to evaluate the data, and calibration curves are developed for 2HG concentrations in both isolated and BRAINO solutions. The study also employs a 3D-printed phantom to validate experimental setups at the 3 T GE scanner and explores in vivo spectra to correlate findings with clinical observations.

The findings suggest optimized spectroscopic parameters for the detection of 2HG and propose potential improvements for future research. This work enhances the understanding of MRS in detecting the metabolite 2HG, offering valuable insights for clinical applications in the differentiation of brain tumors.

Contents

Abbreviations

2HG	-	2-hydroxyglutarate
α-KG	-	α-ketoglutarate
ADC	-	analog-to-digital converter
Avg.	-	Averages
AQ	-	Acquisition
CHESS	-	CHEmican Shift Selective
Cho	-	Choline chloride
CNS	-	Central Nervous System
COSY	-	COrrelated SpectroscopY
Cr	-	Creatine monohydrate
D_2O	-	Deuterium oxide
FID	-	Free induction decay
FLASH	-	Fast low-angle shot
FOV	-	Field of view
FT	-	Fourier transformation
GABA	-	γ-Aminobutyric acid
Glu	-	L-glutamate
GRE	-	GRadient Echo
HUS	-	Haukeland University Hospital
$HNa_2O_4P \cdot 7H_2O$	-	Sodium phosphate dibasic heptahydrate
IDH	-	Isocitrate dehydrogenase
In vivo	-	Inside a living organism
In vitro	-	Outside a living organism
Lac	-	Sodium Lactate
m-Ins	-	Myo-Inositol
MR	-	Magnetic Resonance
MRI	-	Magnetic Resonance Imaging
MRS	-	Magnetic Resonance Spectroscopy
MEGA-PRESS	-	MEscher-GArwood-PRESS
Met.	-	Metabolite
Na_2HPO_4	-	Disodium phosphate
NAA	-	N-acetyl-L-aspartic acid
$NaH_2PO_4 \cdot H_2O$	-	Sodium phosphate monobasic monohydrate
NNP	-	The Norwegian NMR Platform
NMR	-	Nuclear Magnetic Resonance
PP	-	Ping Pong Ball

ppm	-	parts-per-million
PRESS	-	Point RESolved Spectroscopy
RF	-	Radio frequency
SE	-	Spin Echo
SI	-	Signal intensity
sLaser	-	semi-LASER
STEAM	-	STimulated Echo Acquisition Method
TE	-	Echo time
TMS	-	tetramethylsilane
TR	-	Repetition time
TSP	-	3-(Trimethylsilyl)propionoic-2,2,3
UiB	-	The University in Bergen
WHO	-	World Health Organization

Symbols

$\vec{B}_0$	-	Static magnetic field
$\vec{B}_1$	-	Radio frequency field
$\vec{M}$	-	Net magnetization
$\vec{I}$	-	Spin
$\hbar$	-	Planck´s constant
$\vec{u}$	-	magnetic moment
γ	-	Gyromagnetic ratio
ω	-	Angular frequency
ω_0	-	Larmor frequency
ΔE	-	Energy difference
N_x	-	Number of protons in a shell/level
M_{xy}	-	Transverse magnetization
M_z	-	Longitudinal magnetization
r_i	-	Proton location
$\vec{G}$	-	Linear gradients
$\vec{G}_z$	-	Slice selection gradient
$\Delta\omega rf$	-	RF-pulses bandwidth
$\vec{G}_x$	-	Frequency encoding gradient or read out
$\vec{G}_y$	-	Phase encoding gradient
σ	-	Shielding
δ	-	Chemical shift in ppm
J	-	Coupling constant
v	-	Frequency
v_0	-	Reference frequency
$\hat{\rho}$	-	Density Operator
ψ	-	Wavefunction
α	-	Spin states up
c	-	Concentration
m	-	Mass
Mm	-	Molar mass
mM	-	mmol/L
V	-	Volume
t	-	Time
β	-	Spin state down
R^2	-	Linearity

List of Figures

List of Tables

Chapter 1

Introduction

1.1 Aim of Study

The aim of this study is to optimize the model for the detection of 2-hydroxyglutarate (2HG) with magnetic resonance spectroscopy (MRS).

Elevated concentrations of 2HG in the brain are associated with certain brain tumors, which are currently diagnosed through invasive brain biopsies [39]. This study will focus on optimizing the MRS parameters for detecting 2HG, laying the groundwork for developing a non-invasive diagnostic approach. By improving these parameters, the research will contribute to the initial phases of creating a less invasive diagnostic method, potentially reducing the need for brain biopsies in the future.

1.2 Background

The basic principles for measuring nuclear magnetic moments were first explored in 1938 by Rabi et al. [58]. Building on Rabi's work, Purcell et al. [57] and Bloch et al. [11] established the basic principles of Magnetic Resonance (MR) in 1946. Felix Bloch and Edward Mills Purcell were awarded the Nobel Prize in Physics in 1952 for their contributions to the development of nuclear magnetic precision measurement methods [65].

In the 1950s, Proctor and Yu discovered that the changes in resonance frequencies of atomic nuclei depending on their chemical bonds could be detected [54]. This magnetic technology, researched by Proctor and Yu, led to the development of Nuclear Magnetic Resonance (NMR) Spectroscopy, a method used to detect chemical compounds within a selected object. NMR has since been widely applied in various fields, including physics, chemistry, medicine, and petroleum.

In 2003, Paul Lauterbur and Peter Mansfield were awarded the Nobel Prize in Physiology or Medicine for their groundbreaking discoveries in Magnetic Resonance Imaging (MRI) [66]. Lauterbur first published his discovery in *Nature* in 1973, demonstrating a technique that linked chemical and spatial information [34]. He described an image as a graphical representation of the spatial distribution of interactions between matter and radiation fields [34]. Mansfield, intrigued by Lauterbur's work, further advanced the field by developing techniques to accelerate the acquisition of radio signals from nuclei and the formation of images, a method known as echo-planar imaging [66]. The key distinction between Nuclear Magnetic Resonance (NMR)

and Magnetic Resonance (MR) lies in spatial localization, a concept refined by the research of Lauterbur and Mansfield. Mansfield's innovations enabled the first human body imaging using MRI in the 1980s [66, 59].

In 1989, Frahm et al. demonstrated that localized proton-NMR could be used to measure metabolites in a normal human brain *in vivo*. They reported high regional selectivity, good measurement accuracy, and effective water suppression using the STEAM spectroscopy technique [22]. Frahm et al. concluded that "Localized proton spectroscopy as a diagnostic tool for a noninvasive metabolic characterization of cerebral infarcts and tumors bears a great potential for replacing needle biopsy" [22], giving rise to ideas from researchers since.

One of the first studies involving MRS on the human brain was conducted by Alger et al. in 1990 [3]. Initially, the high cost of the equipment necessary for MRS limited its use to research projects. However, by the mid-1990s, software for spectroscopy was developed for personal computers, making it compatible with existing MR equipment. This advancement made the clinical use of MRS for *in vivo* spectroscopy a viable method for acquiring metabolic information [59].

1.3 Brain metabolites

In order to simulate the environment *in vivo* under controlled conditions, a solution with brain metabolites has been used in this study. The brain metabolite solution is a brain phantom solution with a concentration of the metabolites corresponding to that *in vivo* [24].

The brain is composed of a variety of tissues that interfere with MRS signals, making the quantification and separation of each metabolite challenging. To analyze the behavior of 2HG in an optimal environment, a brain metabolite solution is often examined at a high magnetic field. This approach facilitates the separation of different metabolite signals and allows for detailed observation of 2HG behavior with various pulse sequences and echo times (TE) compared to other metabolites *in vivo*.

The metabolites that are included in the brain metabolite phantom are Creatine monohydrate (Cr), Choline chloride (Cho), N-acetyl-L-aspartic acid (NAA), Myo-Inositol (m-Ins), L-glutamate (Glu), Sodium L-actate (Lac) and γ-Amonobutyric acid (GABA). Table 1.1 shows the typical data for a brain metabolite phantom with the compounds abbreviations and their respective molar mass and molarity [24].

Table 1.1: Metabolite molar mass and molarity for the brain metabolite phantom

Metabolite	Abbreviation	*Mm* [g/mol]	Molarity [mM]
Creatine monohydrate	Cr	149,15	10,0
Choline chloride	Cho	139,62	3,0
N-acetyl-L-aspartic acid	NAA	175,14	12,5
Myo-Inositol	m-Ins	180,16	7,5
L-glutamate	Glu	187,13	12,5
Sodium L-actate	Lac	112,06	5,1
γ - Aminobutyric acid	GABA	103,12	2,0

Figure 1.1 shows the chemical structures of the metabolites [14]. The chemical structures, the proton chemical shift, and J-coupling values are obtained from the study, "Proton NMR chemical shifts and coupling constants for brain metabolites" by Govindaraju et al. [25] and Harris et al. [27], and are displayed in Table 1.2. The metabolites are described in detail below, based on Govindaraju et al. [25] and Harris et al. [27] studies.

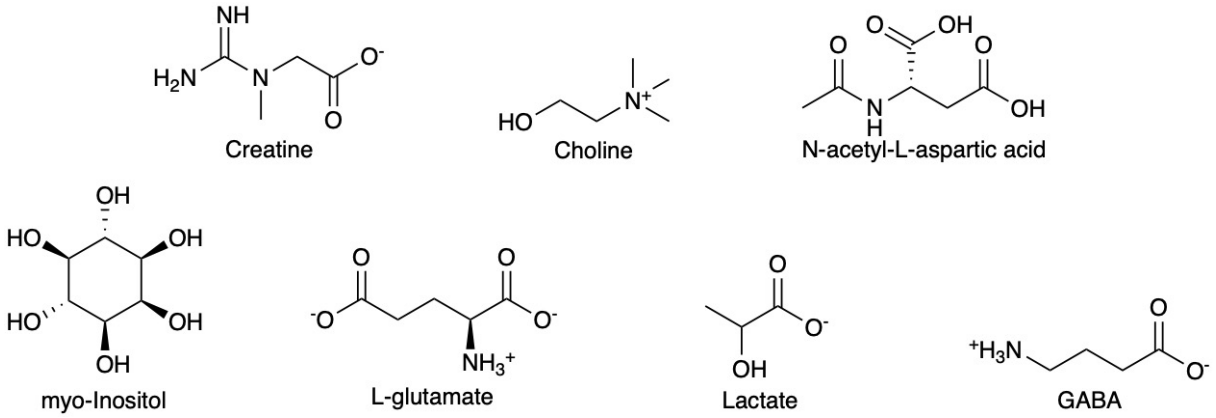

Figure 1.1: The chemical structure for the metabolites in a brain metabolite solution, Cr, Cho, NAA, m-Ins, Glu, Lac and GABA [14].

Figure 1.2 shows a ^1H-spectrum taken at 600MHz of a brain metabolite phantom assigned with their respective metabolites [19].

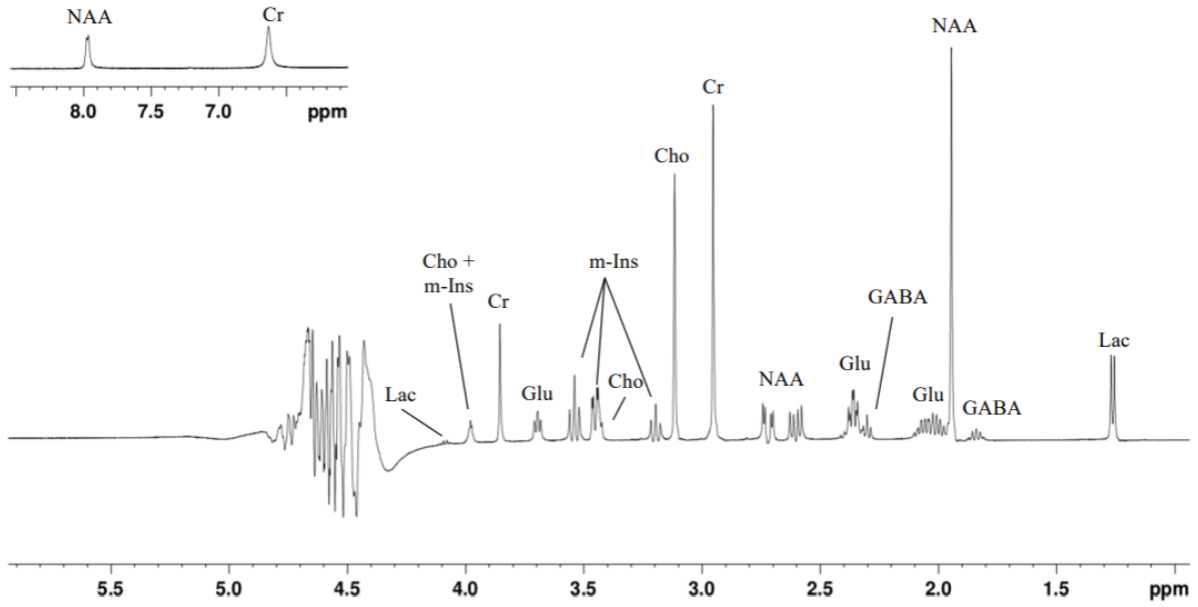

Figure 1.2: A spectrum at 600MHz of a brain metabolite phantom with assigned metabolites [19].

Creatine monohydrate (Cr) is an α-amino acid. It is notable with the two singlets at 3.03 ppm from the $N(CH_3)$ and 3.91 ppm from the $^2CH_2$ groups, displayed in Figure 1.1 and 1.2. For *in vivo* MRS the Cr peaks are reported to overlap with Phosphocreatine because of their methyl groups. The overlapping peaks can be separated with different editing techniques [25].

For *in vivo* MRS studies, the total choline that gives the recognizable singlet at 3.2 ppm comes from free choline, glycerophosphorylcholine, and phosphorylcholine [25]. In the brain metabolite phantom, Choline chloride (Cho) salt is used. Cho has been identified as one of the key nutrients that affect the brain process, and Cho deprivation during early development can lead to compromised cognitive function [17].

N-acetyl-L-aspartic acid (NAA) is a free amino acid. Second to Glu, NAA is the most concentrated metabolite in the human brain [25]. NAA´s highly intensified singlet at 2.0 ppm from the three protons from a N-acetyl CH_3 group, shown in Figure 1.1 and 1.2, makes it an easy metabolite to observe with MRS *in vivo*. NAA has been studied for many clinical neurological and neuropsychiatric applications [25].

Myo-Inositol (m-Ins) is a cyclohexane derivative with a hydroxygroup substitution on each carbon. It is one of the nine isomers of Inositol, and it is detected in the human brain with shorter TE acquisitions [25]. m-Ins is located mainly in glial cells, and the *in vivo* concentration is altered in many brain disorders, including Alzheimer´s disease and brain tumors [26].

L-glutamate (Glu) is an amino acid. It is one of the most concentrated metabolites in brain tissue and the primary excitatory neurotransmitter [25, 27]. The levels of Glu are seen in comparison with neural health, and low levels are a sign of a degenerative disease [27]. Glu consists of two methylene groups and one methine group, shown in Figure 1.1, which contribute to a complex spectrum that results in low intensities for each individual peak. The chemical shifts overlap with GABA, NAA, and glutamine, making it hard to identify the individual signal contribution *in vivo* without a form of editing [25].

Sodium Lactate (Lac) is a byproduct of an anaerobic glycolysis, that in brain tissue normally is presented in a low concentration [25]. Since Lac is a byproduct of an anaerobic metabolism, an increase in Lac indicates an altered metabolism, which among others, happens with cancer [27]. Lac´s spin system and detection are normally carried out from the doublet group from the methyl group at 1.31 ppm [25].

γ-Aminobutyric acid (GABA) is a primary inhibitory neurotransmitter in the human brain [25, 27] and it has a concentration of 1-2 mM [25]. Alternated concentrations are associated with developmental disorders, psychiatric disorders, and neurological diseases [27]. Since the chemical shifts for GABA, shown in Table 1.2, overlap with other more intensified metabolites, spectral editing techniques are often used to observe GABA´s multiplet group at 3.01 ppm [25].

1.4 2-hydroxyglutarate in Glioma Biology

2-Hydroxyglutarate (2HG), also known as DL-α-hydroxyglutaric acid, is a type of 2-hydroxicarboxylic acid derived from glutaric acid. In this structure, a hydrogen atom attached to a carboxylic acid group is replaced by a hydroxy group, [56], as depicted in Figure 1.3. 2HG primarily forms in the brain as a result of mutations in the isocitrate dehydrogenase (IDH) enzymes located within the mitochondria and the cytosol [27], as displayed in Figure 1.4.

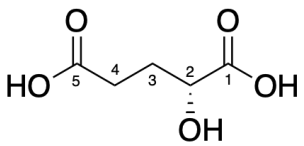

Figure 1.3: 2HG

As previously mentioned, 2HG is produced due to IDH-mutations. IDH exists in three isoforms: IDH1, IDH2, and IDH3. The oxidative decarboxylation of isocitrate is catalyzed in cells to α-ketoglutarate (α-KG), and highly frequent mutations of IDH1 and IDH2 result in altered enzymatic activities of IDH1 and IDH2. This altered enzymatic activity of

IDH1 and IDH2 catalyzes the reduction of α-KG to 2HG, instead of facilitating the production of α-KG [30]. Figure 1.4 displays these metabolic pathways. Due to its role in the disrupted metabolism found in IDH-mutated gliomas, 2HG is classified as an oncometabolite [27].

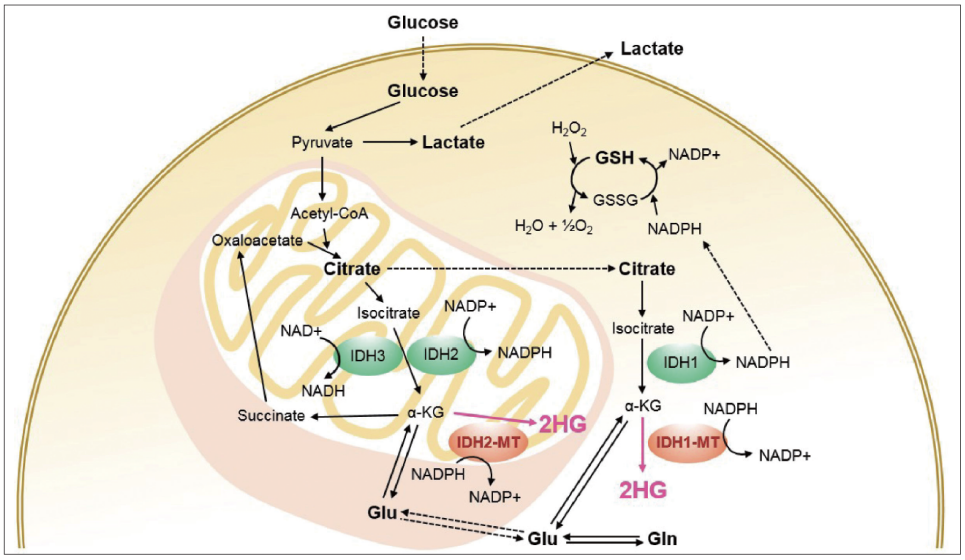

Figure 1.4: A simplified display of the metabolic pathways associated with IDH and 2HG [30].

The 2021 World Health Organization (WHO) classification system for neuropathology relies heavily on molecular markers, including the IDH status, to classify tumors such as gliomas [39]. Gliomas are brain tumors that arise from the malignant transformation of glial cells. Glioblastoma is the most malignant form of these gliomas, characterized by the absence of IDH mutations with the presence of IDH-wildtype [39]. In contrast, the less malignant gliomas, such as oligodendroglioma and astrocytoma, exhibit IDH mutations. Notably, astrocytoma can progress into glioblastoma while retaining the IDH mutation, which is associated with a better prognosis compared to glioblastoma IDH-wildtype [39]. This underscores the significance of early detection of metabolite markers, benefiting both patient outcomes and surgical strategies.

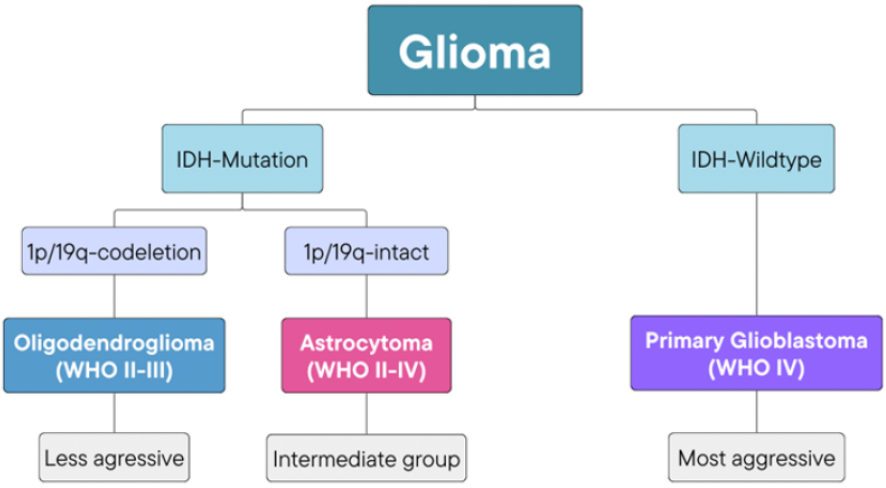

Figure 1.5: A Glioma classification overview based on the classification system from WHO in 2021 developed by PhD student Gunnhild Victoria Trym Ager-Wick.

The classification overview developed by PhD student Gunnhild Victoria Trym Ager-Wick, as shown in Figure 1.5, illustrates the distinctions based on the latest WHO guidelines in 2021. Identifying mutations in IDH directly has proven challenging. However, since these mutations result in the production of 2HG, advanced MRS techniques have been investigated as a potential method for quantifying 2HG. Despite its promise, this method has not yet been adopted in clinical practice due to complexities inherent in the quantification process. To refine and optimize the sequence parameters for the detection, this thesis consists of phantom studies focused on 2HG quantification.

1.5 Earlier studies

In preparation for the laboratory work for 2HG, several earlier studies were reviewed. From earlier studies done at the University of Bergen, Ida Landmark Fjermestad´s master thesis "Spectral editing of brain metabolites using weighted Nuclear Magnetic Resonance" was used in regard to her detection of the different brain metabolites with NMR, and Magnus Svensen´s master thesis "Quantitative diffusion-weighted J-difference spectroscopy of common brain metabolites" was used in regard of his study with spectral editing. Previously published research articles on brain metabolites, especially 2HG and the use of MRS in the detection of brain tumors, were reviewed in regard to the best approach for the 2HG-detection models.

In Fjermestad´s master thesis, she performed a peak assignment of the compounds in a brain metabolite solution, as well as a J-difference editing on each compound. Her results were taken into account in the analysis of the results in this thesis [19]. The calibration curves in this master thesis were made based on a similar approach done by Svensen on calibration curves for GABA [63].

The chemical structures, the proton chemical shift, and J-coupling values for the brain metabolites are obtained from the study "Proton NMR chemical shifts and coupling constants for brain metabolites" by Govindaraju et al. [25], and are displayed in Table 1.2. The chemical shifts were reported with reference to DSS-trimethyl with a singlet at 0 ppm, and the multiplicity was observed in a conventional one-dimensional spectrum recorded at 500 and/or 600 MHz.

Table 1.2: Overview of the proton chemical shift, J-coupling values, and multiplicity for metabolites in the brain metabolite solution. The information is obtained from the study: Proton NMR chemical shifts and coupling constants for brain metabolites by [25].

Compound	Group	δ [ppm]	Structure	J [Hz]	Connectivity
Cr	$N(CH_3)$	3,0270	s	-	-
	$^2CH_2$	3,9130	s	-	-
	NH	6,6490	s	-	-
Cho	$^7CH_2$	4,312	m	3,10	7–8, 7′–8′
				2,67	7, 7′-N
	$^8CH_2$	3,659	m	5,90	7–8′, 7′–8
	$N(CH_3)_3$	3,212	s	6,03	3, 3′-P; 7, 7′-P
NAA	$^2CH_3$	2,0080	s	-	-
	^2CH	4,3817	dd	3,861	$2-3$
	$^3CH_2$	2,6727	dd	9,821	$2-3'$

Continued on next page

Table 1.2 – continued from previous page

Compound	Group	δ [ppm]	Structure	J [Hz]	Connectivity
		2,4863	dd	-15,592	$3-3'$
	NH	7,8205	d	6,400	NH-2
m-Ins	^{1}CH	3,5217	dd	2,889	$1-2$
	^{2}CH	4,0538	t	9,998	$1-6$
	^{3}CH	3,5217	dd	3,006	$2-3$
	^{4}CH	3,6144	t	9,997	$3-4$
	^{5}CH	3,2690	t	9,485	$4-5$
	^{6}CH	3,6144	t	9,482	$5-6$
Glu	^{2}CH	3,7433	dd	7,331	$2-3$
	$^{3}CH_2$	2,0375	m	4,651	$2-3'$
		2,1200		-14,849	$3-3'$
	$^{4}CH_2$	2,3378	m	8,406	$3-4'$
		2,3520		6,875	$3'-4'$
				6,413	$3-4$
				8,478	$3'-4$
				-15,915	$4-4'$
Lac	^{2}CH	4,0974	q	6,933	$2-3$
	$^{3}CH_3$	1,3142	d	6,933	$2-3$
GABA	$^{2}CH_2$	3,0128	m	5,372	$2-3$
				7,127	$2-3'$
	$^{3}CH_2$	1,8890	qu	10,578	$2'-3$
				6,982	$2'-3'$
	$^{4}CH_2$	2,2840	t	7,755	$3-4$
				7,432	$3-4'$
				6,173	$3'-4$
				7,933	$3'-4'$

Some earlier studies have researched the optimal spectral parameters for the 2HG detection *in vivo* with MRS regarding tumors. The pulse sequences and spectral parameters used in earlier studies were analyzed to find a starting point regarding the spectral parameters, and especially pulse sequences and TE, in this project. Choi et al. [15] published a study of 30 subjects with different graded tumors in 2012. For each case of 2HG detection, they confirmed IDH1 and IDH2 mutation, and failure to detect 2HG was confirmed with the detection of wild-type IDH1 and IDH2. Their optimized TE time for the PRESS sequence was 97 ms and for the MEGA-PRESS editing sequence was 106 ms [15]. Pope et al. [53] studied 27 consecutive adult patients with intracranial glioma, with a double-echo PRESS sequence at TE = 30 ms [53]. Nguyen et al. [45] published in 2018 a study with 58 subjects analyzed with MEGA-PRESS, TE = 60 ms, and routine clinical brain tumor MR sequences at 3 T. For the spectral editing, a 20 ms Gaussian 180° pulse was applied at 1.9 ppm for the edit-on condition [45]. In 2022 Juskanic et al. [31] published a study on the diagnostic performance of edited 2HG MRS where they studied 39 MR spectra of patients with suspected glioma with a 3 T system with the MEGA-PRESS sequence with TE = 68 ms and editing pulse at 1.9 ppm for the edit-on conditions [31]. Autry et al. [5]

used the PRESS sequence with TE = 65 ms to acquire 2HG-specific 3D MRSI data in a study published in 2022 [5]. In 2021 Bhandaril et al. [9] summarized some of the *in vivo* studies done on the detection of 2HG. The sequences and TE referred to by Bhandaril et al. were PRESS with TE = 128 ms, 384 ms, 96 ms, 144 ms and MEGA-PRESS with TE = 64 ms and 128 ms [9]. Shams et al. [62] studied 2HG at 7 T with the pulse sequences sLaser with TE = 110 ms and MEGA-sLaser with TE = 74 ms [62].

The difficulties in the separation of the 2HG signals from other metabolites were explored with a comparison of the signals at a 3 T and 7 T field by Berrington et al. [7] and published in 2018. 9 patient scans from a sLaser with long TE = 110 ms were studied as well as phantom data with the same parameters [7].

Some researchers have also studied brain tumor tissues with NMR. Kalinina et al. [32] published in 2012 a study of 75 individual brain tissue samples with NMR as one of the first brain tissue studies of 2HG with NMR. The sequences used were HRMAS NMR and 2D COSY [32]. Park et al. [50] studied 4 brain tumor tissues at 900 MHz with $^1H-^1H$ COSY and $^1H-^{13}C$ HSQC, and ^1H 1D experiments in two of the samples [50].

One of the first articles with a study of 2HG with NMR spectroscopy was written by Bal et al. [6] and published in 2002. The study was done in regard to the diagnosis of two metabolic diseases, 2-D-hydroxyglutaric aciduria and 2-L-hydroxyglutaric aciduria. These diseases are diagnosed by the concentration of 2HG in the urine of a newborn child [6]. During their study, Bal et al. determined the chemical shifts and coupling constants for 2HG at 400 MHz, displayed in Table 1.3. The chemical shifts and coupling constants in Table 1.3 from [6] were used as a starting point for the calculations done with Daisy for the simulated spectra in this thesis.

Table 1.3: Chemical shifts, δ, and coupling constants, J, for 2HG at 400 MHz [6].

Parameter	position	2HG [pH 7.0]
δ [ppm]	2	4.022
	3	1.825
	3´	1.977
	4	2.221
	4´	2.272
J [Hz]	2, 3	7.6
	2, 3´	4.1
	2, 4	0.0
	2, 4´	0.0
	3, 3´	-14.0
	3, 4	5.3
	3, 4´	10.4
	3´, 4	10.6
	3´, 4´	6.0
	4, 4´	-15.0

Neuberg et al. [44] published in 2017 a phantom study on 2HG at 9.4 T. In their study a PRESS sequence with TE = 11.5 ms resulted in the biggest area under the curve, and for the J-difference editing they used the MEGA-PRESS sequence with a TE = 60 ms and the edit-on

conditions were at 1.9 ppm [44]. As mentioned Berrington et al. [7] and Shams et al. [62] studied phantom data of 2HG as well as *in vivo* spectra of suspected Glioma patients.

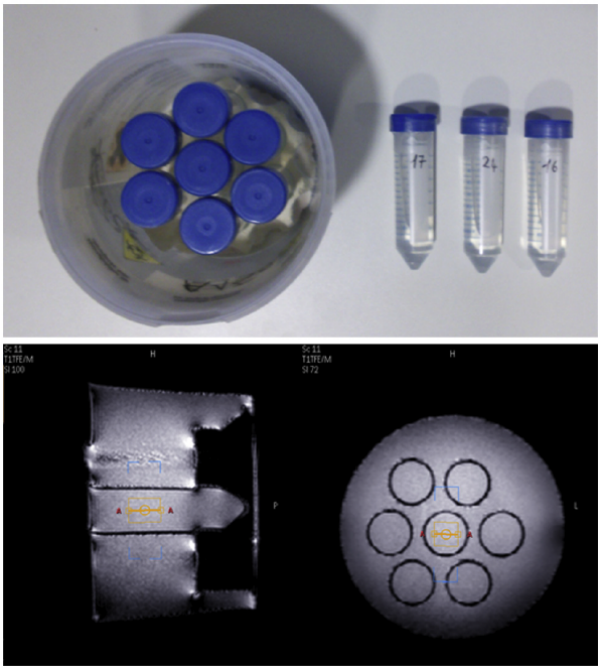

Figure 1.6: The setup and an MRI of the phantom used in Bertolini et al. [8].

Bertolino et al. [8], did a phantom study on 2HG in 2014 with smaller compartments placed with polystyrene supports in a cylindrical plastic bucket filled with 3 L of deionized water, displayed in Figure 1.6. Bertolino et al. looked at the overlapping signals from NAA and Glu with 2HG, and how the different concentrations affected the signals. This study inspired the idea for the 3D-printed phantom developed in this study.

Chapter 2

Theory

This chapter outlines the theoretical concepts that is the foundation for the research performed in this thesis. It is written based on the books by Keeler [33], Bjørnerud [10], Rule and Hitchens [60], and Chang et al. [12].

2.1 Magnetic Resonance

Magnetic resonance (MR) is based on the interaction of an applied magnetic field and a nucleus that possesses spin. The nuclear spin angular momentum depends on the atomic composition. An atom has at least one occurring isotope that possesses spin, and thus every element has the ability to be examined using MR [12]. Magnetic resonance can be used to obtain both images and specters, respectively magnetic resonance imaging (MRI) and magnetic resonance spectroscopy (MRS).

2.1.1 Spin and magnetic moment

Based on Dalton´s atomic theory, an atom can be defined as the basic unit of an element that can occur in chemical combinations. A series of investigations beginning in the 1850s and extending into the twentieth century demonstrated that atoms consisted of subatomic particles called protons, neutrons, and electrons [13]. The protons have a positive charge, neutrons have no charge and electrons have a negative charge. The protons and neutrons are located in the atomic core, the nucleus, and the subatomic particle, electrons, are located in orbitals surrounding the nucleus [12, 13]. Each atom can be identified by the number of protons and neutrons they contain. The number of protons in the nucleus is called the atomic number, and all atoms in an element have the same atomic number. In a neutral atom, the number of protons is equal to the number of electrons, which means that the atomic number also indicates the number of electrons present in the atom. The atomic mass number is the total number of protons and neutrons in the nucleus. This indicates that the number of neutrons in an atom is given by the difference between the mass number and the atomic number. Atoms that have the same atomic number, but different mass numbers are called isotopes [13]. The display of the mass number and atomic number in the Periodic table is displayed in Figure 2.1.

Figure 2.1: The placement of the atomic number and mass number for an element in the Periodic table [43].

Nuclei with an odd number of protons or neutrons have a spin angular momentum. This means that the nuclei appear to rotate around an axis with a constant rate, and this self-rotating axis is perpendicular to the direction of the rotation [12], see Figure 2.2a. The spin angular moment value is given by the quantum number, $\vec{I}$, seen in Equation 2.1 [4], where h is Planck´s constant and $\hbar = \frac{h}{2\pi}$.

$$J = \sqrt{I(I+1)}^{\frac{1}{2}}\hbar \tag{2.1}$$

If the nucleus has an even atomic weight and an odd atomic number it has an integral value for I(e.g., 1, 2, 3) and if the nucleus has an odd atomic weight it has a half-integral value for I(e.g., $\frac{1}{2}, \frac{3}{2}, \frac{5}{2}$) [12]. Since the ^1H nucleus consists of a single proton the spin angular momentum for ^1H is $I = \frac{1}{2}$. The human body is composed of tissues mainly containing water and fat, which both contain hydrogen. Hydrogen is therefore often used in MRS, and most of the MRI experiments are based on the ^1H nucleus [12].

A nucleus can have a positive charge that produces a local composing magnetic field known as the magnetic moment orientated parallel to the axis of rotation. The axis of rotation can be viewed as a vector with a definite orientation and magnitude. The orientation of the spin and the changes it undergoes due to the experimental manipulation is the basis for the signal in MR [12].

The magnetic moment of a spin is given by Equation 2.2,

$$\vec{\mu} = \gamma\vec{J} \tag{2.2}$$

where γ is the gyromagnetic ratio. The gyromagnetic ratio has its own characteristics for each nuclear isotope possessing a spin [10].

In the absence of an external magnetic field to affect the magnetic moment, the sum of the magnetic moments of the spins is given by the vector $\vec{M}$,

$$\vec{M} = \sum \vec{\mu} = 0 \tag{2.3}$$

An arbitrary volume of tissue containing protons, ^1H, where each proton has a spin vector of equal magnitude, and the spin vectors for the protons in the tissue are randomly orientated in all directions are visualized in Figure 2.2B. Given a vector addition of these spin vectors, the sum equals zero and it has no net magnetization [12], as explained in Equation 2.3.

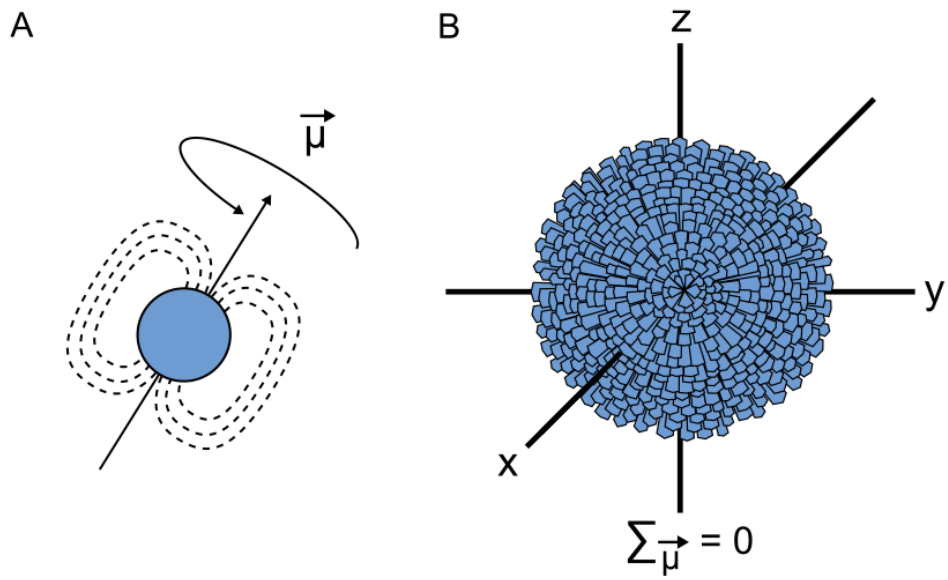

Figure 2.2: Nucleus with spin angular momentum expressed as a magnetic moment in the absence of an external magnetic field (A) [64]. Example of how the nuclei in a macroscopic sample are randomly arranged in the absence of an external magnetic field (B) [64].

A nucleus with a spin, $\vec{I}$, and a magnetic moment, $\vec{\mu}$, can be affected in three different ways. With a static magnetic field, $\vec{B}_0$, a radio frequency field, $\vec{B}_1$, and linear gradients, $\vec{G}$.

2.1.2 The dynamics of the magnetic moment in the static magnetic field

When a spin with a magnetic moment, $\vec{\mu}$, is placed inside a static magnetic field, $\vec{B}_0$, directed along the z-axis in a Cartesian coordinate system the time-dependent $\vec{\mu}$ is given by Equation 2.4, seen in Figure 2.3A.

$$\frac{d\vec{\mu}}{dt} = \gamma\vec{\mu}x\vec{B}_0 \tag{2.4}$$

Equation 2.4 can be solved in a rotating coordinate system, where the xy-plane rotates with an angular frequency, $\vec{\omega}$, given in Equation 2.5.

$$\vec{\omega} = -\gamma\vec{B}_0 \tag{2.5}$$

Equation 2.4 can be transferred to Equation 2.6.

$$\frac{d\vec{\mu}}{dt} = \gamma\vec{\mu}x(\vec{B}_0 + \vec{\omega}) \tag{2.6}$$

When $\vec{\omega} = -\gamma\vec{B}_0$,

$$\frac{d\vec{\mu}}{dt} = 0 \tag{2.7}$$

and the solution is given by the constant $\vec{\omega}$. That means that $\vec{\mu}$ precess around $\vec{B}_0$ with a frequency equal to the rotating coordinate system, $\vec{\omega}$. Equation 2.5 corresponds with the Larmor frequency given in Equation 2.8 [33, 12].

$$\upsilon_0 = \frac{\gamma B_0}{2\pi} \tag{2.8}$$

The observed nucleus is ${}^1H$ with a gyromagnetic ratio, $\gamma = 267,522 \cdot 10^6\ rad \cdot s^{-1} \cdot T^{-1}$ [55], and at 600 MHz the Larmor frequency of protons in Tesla, T, are approximately 14.1 T, calculated with Equation 2.8.

With a static magnetic field, $\vec{B}_0$, and no outer field, the time-dependent M in the rotating reference system is given in Equation 2.9,

$$\frac{d\vec{M}}{dt} = 0 \tag{2.9}$$

where $\vec{M}$ is statically aligned the z-axis, Figure 2.3C, and have no components along the xy-plane.

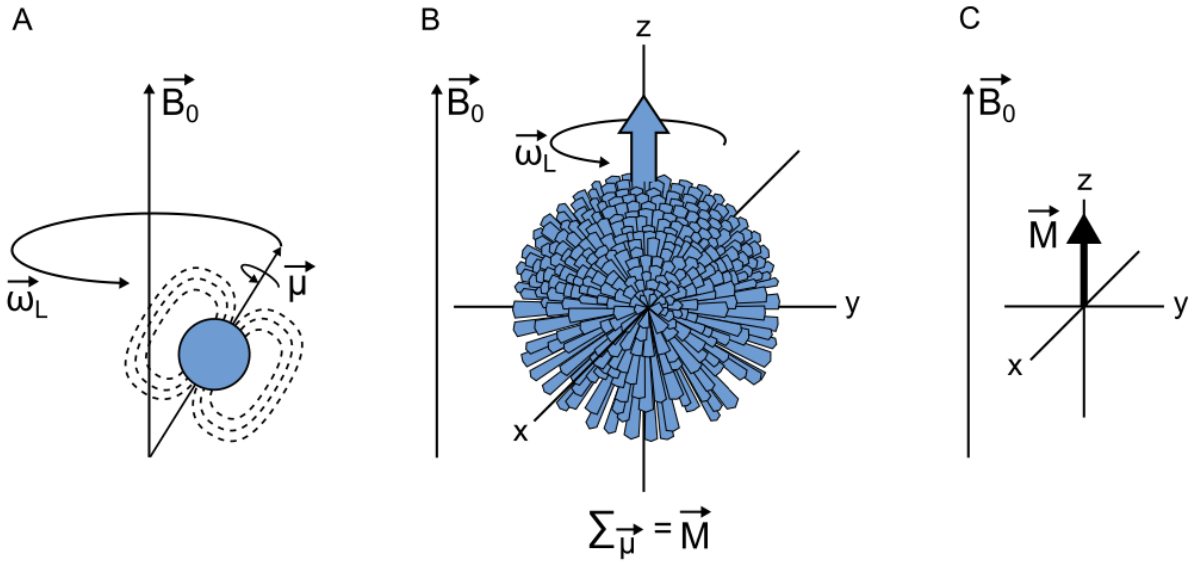

Figure 2.3: Display of how a nucleus with spin $I = \frac{1}{2}$ in a static magnetic field, $\vec{B}_0$, precess (A) [64]. Display of how the sum of the precessing nuclei in a macroscopic sample forms the net magnetization vector, $\vec{M}$, in the presence of an external magnetic field, $\vec{B}_0$ (B) [64]. The net magnetization vector is depicted as a vector in a Cartesian coordination system (C) [64].

The motion of each proton can also be explained by a set of coordinates perpendicular, x- and y-components, and parallel, z-component, to $\vec{B}_0$. If there is performed a vector addition of the spin vectors inside the magnetic field, the spin orientations to the perpendicular components will be randomly distributed because they are out of phase. Since there is an orientation to the precessional axis that is constant with time, there is a constant nonzero interaction between the proton and $\vec{B}_0$, known as the Zeeman interaction [12]. The Zeeman interaction causes a difference in the energy between protons aligned parallel and anti-parallel to the $\vec{B}_0$-field. The energy difference ΔE, Equation 2.10 [4, 33], is proportional to $\vec{B}_0$.

$$\Delta E = \hbar \gamma B_0 \tag{2.10}$$

The magnetic field induces a polarization of the spin orientation for a collection of protons, which align a plural of the protons parallel to the $\vec{B}_0$-field. The Boltzmann distribution, Equation 2.11 [4], gives the exact number of protons in each level.

$$\frac{N_{upper}}{N_{lower}} = e^{-\frac{\Delta E}{kT}} \tag{2.11}$$

Because of the unequal number of protons in each energy level, the vector addition of the spins will be nonzero and parallel with the magnetic field, $\vec{B}_0$. The induced polarization done by the magnetic field gives the sample placed in the MR machine a net magnetization, $\vec{M}$, and this induced magnetization and its manipulation is the source of signal for all MR experiments [12]. As long as the net magnetization is parallel to the $\vec{B}_0$-field, the net magnetization, $\vec{M}$, is static and not detectable.

2.1.3 The Radio Frequency field

Signal detection in MR is achieved when nuclei emit energy after an RF pulse, with a Larmor frequency, is turned off. This RF pulse, consisting of electromagnetic radiation in the RF range, is applied perpendicular to the static magnetic field along the x-axis, known as an excitation pulse. The RF pulse generates an additional magnetic field, denoted as $\vec{B}_1$, the Radio Frequency field. To detect a signal, the net magnetization $\vec{M}$ must be oriented into the xy-plane. The RF field is applied, creating phase coherence among the $\vec{\mu}$. The time-dependent $\vec{M}$ can then be expressed as,

$$\frac{d\vec{M}}{dt} = \gamma \vec{M} x \vec{B_{1x}} \tag{2.12}$$

This corresponds to a rotation of the vector around the $\vec{B_{1x}}$ in the yz-plane with an angular frequency equal to the Larmor frequency, $\vec{\omega}_1 = \gamma \cdot \vec{B}_1$. The rotation angle is given in Equation 2.13, where t_p is the duration of the RF pulse.

$$\theta = \gamma \cdot B_1 \cdot t_p \tag{2.13}$$

The Larmor frequency and orientation difference facilitates the interaction between the RF pulse and the net magnetization, $\vec{M}$. The absorption of RF energy causes $\vec{M}$ to rotate away from its equilibrium orientation along $\vec{B}_0$, perpendicular to both $\vec{B}_0$ and $\vec{B}_1$ [12, 33, 10]. If the RF pulse is left on long enough and with a high enough amplitude, the absorbed energy will cause $\vec{M}$ to rotate fully into the xy-plane. This is known as a 90° RF pulse.

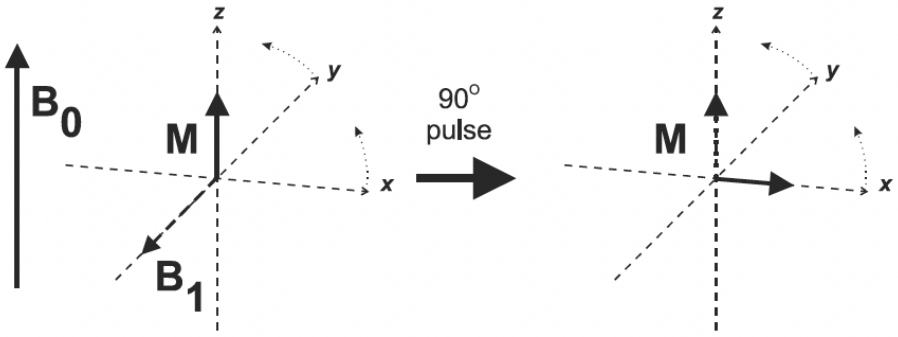

Figure 2.4: The behavior of $\vec{M}$ after the absorption of the RF energy from the 90° pulse [12].

After the 90° RF pulse there will, as shown in Figure 2.4, be a component of $\vec{M}$ present in the xy-plane, $\vec{M}_{xy}$ rotating about the z-axis. This rotating nature makes it possible to detect the presence of the magnetization component through the induction of a current in a coil placed within the oscillating field [10]. If this receiver coil is placed perpendicular to the xy-plane, the

protons from $\vec{M}_{xy}$ induce a voltage in the coil during their precession, and this induced voltage is known as the Free induction decay, FID, and are the MR signal [12].

The three most common types of RF pulses are presented in Figure 2.5. The rectangular pulses in Figure 2.5a, also called hard pulses are used when no spatial or spectral selection is necessary. A short rectangular hard pulse excites all the nuclei in a sample, the whole range of frequencies and chemical shifts. The corresponding frequency profile to the hard rectangular pulse is a sinc [40, 64]. When a spatial or spectral selection is done a sinc or Gaussian RF pulse is used, Figure 2.5b and 2.5c. The sinc and Gaussian pulses are also called soft pulses, and they have a narrow bandwidth that only excites nuclei with a certain range of frequencies [64]. The frequency profile produced by the sinc RF pulse is a rectangle, Figure 2.5b, while a Gaussian RF pulse produces the frequency profile in a Gaussian form [40].

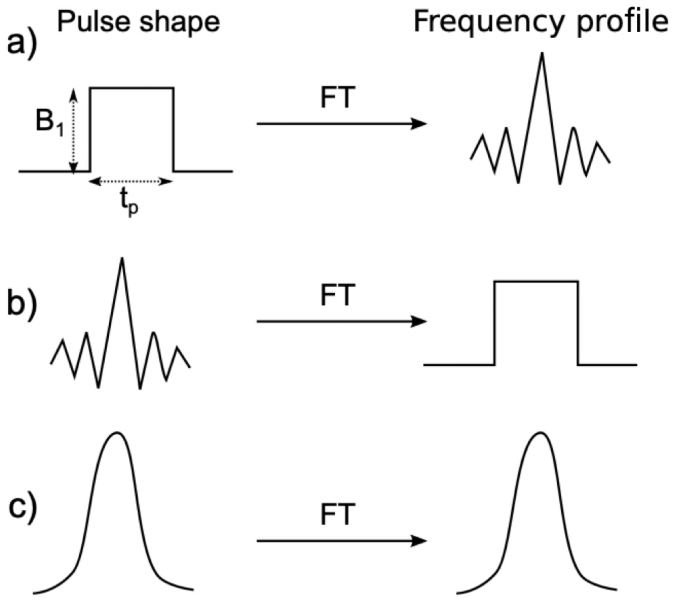

Figure 2.5: RF pulses shapes and corresponding frequency profiles: rectangular RF pulse that produces a sinc-shaped frequency profile (a) [40], sinc RF pulse that produces a rectangular frequency profile (b) [40], and a Gaussian RF pulse and frequency profile (c) [40].

When the RF pulse is turned off the protons immediately begin to reorient themselves to their equilibrium orientation along $\vec{B}_0$.

2.1.4 Relaxation

The free induction decay, FID, is the response of the net magnetization $\vec{M}$ to an RF pulse as a function of time, and it is proportional to the amount of transverse magnetization, $\vec{M}_{xy}$, generated by the pulse [12]. The initial magnitude of the FID signal depends on the value of $\vec{M}$ immediately before the 90° pulse. The FID signal decays with time as more and more protons give up their absorbed energy through a process known as relaxation, which makes the coherence of the proton's motions decrease, as shown in Figure 2.6A.

The Fourier transformation, FT, converts the digital version of the MR signal, the FID, from a function of time to a function of frequency, Figure 2.6.

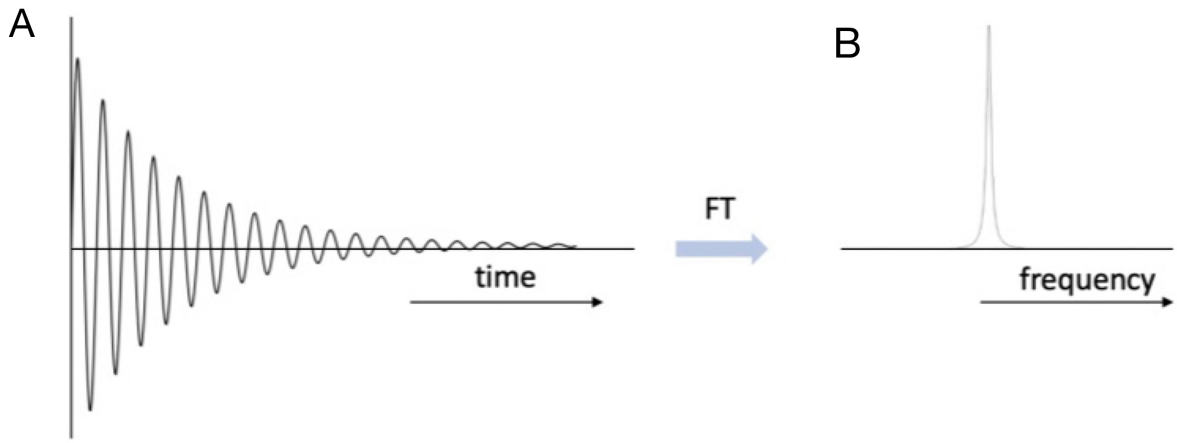

Figure 2.6: Schematic presentation of the Fourier transformation from time domain (A) to frequency domain signal (B) [19].

After a single excitation pulse one can observe that the induced electrical signal, FID, rapidly decays to zero, Figure 2.6a. This signal decay is due to the proton relaxation and is the result of the proton's emission of the absorbed energy from the excitation pulse. The macroscopic effect of the relaxation is that $\vec{M}_{xy}$ gradually disappears and, $\vec{M}_z$ gradually recovers [10], Figure 2.7.

Figure 2.7 shows the evolution of the transverse, $\vec{M}_{xy}$, and the longitudinal, $\vec{M}_z$, magnetization components after an RF excitation pulse. The longitudinal magnetization returns to its equilibrium magnetization with the time-constant T_1, and the transverse magnetization decays with a time-constant T_2^* [10].

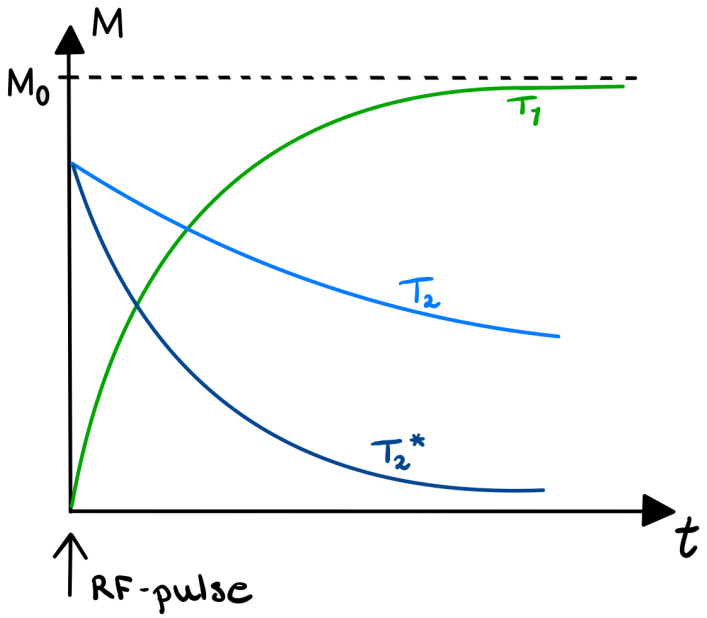

Figure 2.7: The T_1, T_2 and T_2^* relaxation after an excitation pulse [10].

When the RF field is turned off the relaxation processes are introduced according to the well-known Bloch Equations 2.14, 2.15, 2.16, where M_0 is the magnetization at thermal equilibrium.

$$\frac{dM_x}{dt} = \frac{-M_x}{T_2} \tag{2.14}$$

$$\frac{dM_y}{dt} = \frac{-M_y}{T_2} \tag{2.15}$$

$$\frac{dM_z}{dt} = \frac{M_0 - M_z}{T_1} \tag{2.16}$$

T_2 relaxation refers to the process where a stimulated, excited, proton transfers energy to the neighboring protons, resulting in the decay of the transverse magnetization, $\vec{M}_{xy}$, Equation 2.17 [10]. Immediately after the excitation pulse, $\vec{M}$ is rotated down to the xy-plane, and a coherence is in place. This coherence disappears simultaneously with the reorientation of $\vec{M}$ and the proton's emission of energy. As the coherence disappears and $\vec{M}_{xy} \longrightarrow 0$, the FID accumulates. By defining $M_x + iM_y = M_{xy}$, the solution for M_{xy} is given by Equation 2.17, where M_0 is the value of the xy-magnetization at $t = 0$.

$$M_{xy} = M_0 \cdot e^{\frac{-\tau}{T_2}} \tag{2.17}$$

In an inhomogeneous magnetic field, Equation 2.17 changes to

$$M_{xy} = M_0 \cdot e^{\frac{-\tau}{T_2^*}} \tag{2.18}$$

The apparent transverse relaxation time, T_2^*, defines the overall decay rate due to inhomogeneous contributions [10]. This relaxation time accounts for the bulk inhomogeneities, ΔB_0, in the static magnetic field, $\vec{B}_0$. As depicted in Figure 2.7 T_2^* relaxation occurs faster than T_2 relaxation because of the inhomogeneities. Variations in the Larmor frequency, caused by field inhomogeneities, lead to a loss of phase coherence among spins. Consequently, the transverse magnetization, $\vec{M}_{xy}$, decays more quickly than the longitudinal magnetization, $\vec{M}_z$, recovers, making T_2^* shorter than T_1 *in vivo*, confirming that $T_1 \neq T_2$. Additionally, the transverse relaxation time varies with tissue composition, being generally longer in fluids than in solid tissues [12, 10].

$$\frac{1}{T_2^*} = \frac{1}{T_2} + \gamma \Delta B_0 \tag{2.19}$$

T_1 relaxation refers to the process where a stimulated, excited, proton emits energy to the surroundings [12], resulting in a recovery of the longitudinal magnetization, $\vec{M}_z$, Equation 2.16. The solution of the z-magnetization is given by Equation 2.20,

$$M_z(\tau) = M_0(1 - A_0 \cdot e^{\frac{-\tau}{T_1}}) \tag{2.20}$$

where A_0 is an integration constant that depends on the initial conditions. After a 90°-pulse $M_z(0) = 0, A_0 = 1$, and after a 180°-pulse $M_z(0) = -M_0, A_0 = 2$.

In MR experiments a series of RF pulses is applied in a sequence, referred to as a pulse sequence. The influence the transverse, $\vec{M}_{xy}$, and the longitudinal, $\vec{M}_z$, magnetization have from the RF pulses depends on the repetition time, TR, and the echo time, TE. TR is the time interval between successive RF excitation in a pulse sequence, while TE is the time delay from the excitation pulse and the actual recording of the signal [10].

2.2 Magnetic Resonance Imaging

Magnetic resonance imaging, MRI, uses a spatially dependent magnetic field by applying the magnetic field gradients. These gradients are small linear disturbances on the static magnetic field, which means that the exact magnetic field is linearly dependent on the location in the magnetic field, given by Equation 2.21, where $\vec{B}_i$ is the magnetic field at location r_i and G_T is the total gradient amplitude [12].

$$\vec{B}_i = \vec{B}_0 + \gamma \vec{G}_T \times \vec{r}_i \tag{2.21}$$

The presence of magnetic field gradients gives an expanded version of the Larmor equation, formerly given by Equation 2.8. In the expanded Larmor equation, Equation 2.22, $\vec{\omega}_i$ is the frequency of the proton at the location r_i, and $\vec{G}$ represents the total gradient amplitude and direction [12].

$$\vec{\omega}_i = \gamma(\vec{B}_0 + \vec{G}r_i) \tag{2.22}$$

An MR image is a frequency and phase map of the protons generated by unique magnetic fields at each voxel throughout the image.

The building blocks for MRI are the static magnetic field, $\vec{B}_0$, the RF field, $\vec{B}_1$, and the linear gradients, $\vec{G}$. How the static magnetic field, $\vec{B}_0$, and the RF field, $\vec{B}_1$, affect the nuclei was explained in chapter 2.1.

2.2.1 Slice selection

The magnetization that is detected, $\vec{M}$, is an average of the whole magnetization in the object. The whole object has the same resonance frequency which makes it hard to separate the different voxels in the object from each other.

To differentiate the sections, various gradients are applied, each affecting the voxels in distinct ways. In the z-direction, known as the slice direction, a slice selection gradient is used. In the x-direction, referred to as the readout direction, a frequency encoding gradient is applied. Meanwhile, in the y-direction, a phase encoding gradient is applied.

The first step in MRI is to localize the RF excitation to a region of space. That is done with a frequency-selective excitation and a slice selection gradient. The slice selection gradient is referred to as G_z.

The slice selection is determined by Equation 2.23,

$$\Delta z = \frac{\Delta\omega_{rf}}{\gamma G_z} \tag{2.23}$$

where G_z is the gradient amplitude, Δz is the thickness of the slice, and $\Delta\omega_{rf}$ is the RF pulses bandwidth. The bandwidth, $\Delta\omega_{rf}$, decides in which range in frequency the RF pulse affects the spins. When a slice is selected, the gradient and the bandwidth are adjusted individually, and the applied RF pulse is a soft pulse.

2.2.2 k-space

To obtain the required information to reconstruct an MR image the phase and frequency distribution is modified with gradients. The letter k is used to represent the coordinates in the Fourier domain, which is denoted $k-space$ in MRI [10]. The Swedish physicist Stig Ljungren first introduced the $k-space$ in 1983 as a way to visualize the trajectories of spins under the influence of gradients. Since MRI is a 3-dimensional acquisition technique, a 3D reconstruction of the magnetization distribution in the object can be visualized in a $k-space$ [10], defined by

$$k = \frac{\gamma}{2\pi}\int_0^t G(t)dt \tag{2.24}$$

where G is the maximum magnetic field strength.

The $k-space$ is acquired using Equation 2.26 and Equation 2.28, where the x-coordinated k_x represents different complex time points in the readout direction and the y-coordinate k_y represents different phase encoding gradient amplitudes [12].

The frequency encoding, also referred to as the readout, is denoted as G_x, and this is the signal detection part of MRI [12]. While the echo is accumulated G_x is applied perpendicular to the slice selection, G_z. The protons precess with different frequencies based on their position in the field, given by Equation 2.25, which comes from Equation 2.22 [12, 10].

$$\omega_x = \gamma(\vec{B}_0 + G_x r_x) = \vec{\omega}_0 + \gamma G_x r_x \tag{2.25}$$

In a readout process, the signal detection for the frequency encoding is done with Equation 2.26.

$$k_x = \frac{\gamma}{2\pi} G_x \cdot DW \cdot N \tag{2.26}$$

In Equation 2.26 [10] DW is the distance between the digital points acquired over an acquisition time, AQ. N is the number of readout samples, which through the whole AQ is references TD, and change Equation 2.26 to $k_x = \gamma\vec{G}_x \cdot DW \cdot TD$.

After an excitation, each proton in the excited volume precess at the same frequency. As explained, during the accumulation of the echo the gradient is applied, which causes a variation in frequency for the protons that generate the echo signal. According to Equation 2.25, the frequency of precession, $\vec{\omega}_x$, for each proton depends on its position, noted in Equation 2.25 as r_x [12].

The phase encoding is denoted as G_y. The gradient is applied perpendicular to both G_z and G_x [10, 12]. It changes the amplitude during a 2D image sequence.

The proton's precession is periodic in nature. Before the phase encoding gradient is applied along the y-axis, the proton precess with a frequency equal Equation 2.4. When the gradient is turned on the proton will precess with a frequency equal to Equation 2.27.

$$\omega_y = \gamma(\vec{B}_0 + G_y y) = \vec{\omega}_0 + \gamma G_y y \tag{2.27}$$

After the phase encoding is turned off the proton will precess back to the original frequency ω_0 as explained, but the different protons will have a changed phase relative to the phase they had before the gradient was turned on. The phase change, Θ_i, is dependent on the position of the proton, y_i, in the slice. The proton positioned in the isocenter experience no effect from the gradient and thus experience no phase shift either.

The amount of change in phase shift depends on the magnitude and duration of the gradient, G_y, and the proton location [12]. Protons that are located in different places in the slice experience different amounts of phase shift for the same gradient pulse. Protons located on the edge of the field of view (FOV) get to experience a maximum of the phase encoding step [12]. In MRI, the image information is obtained by repeating the slice selection and the frequency encoding multiple times, each with different amplitudes of G_y [12].

$$k_y = \frac{\gamma}{2\pi} G_y \cdot t_p \tag{2.28}$$

The information for the image in an MRI is obtained with Equation 2.28 [10], where t_p is the length of the phase encoding gradient, G_y. The phase encoding gradient is usually varied systematical from a large positive value to a large negative value.

When an image is acquired in MRI it is done in a $k-space$ with the gradients as explained earlier.

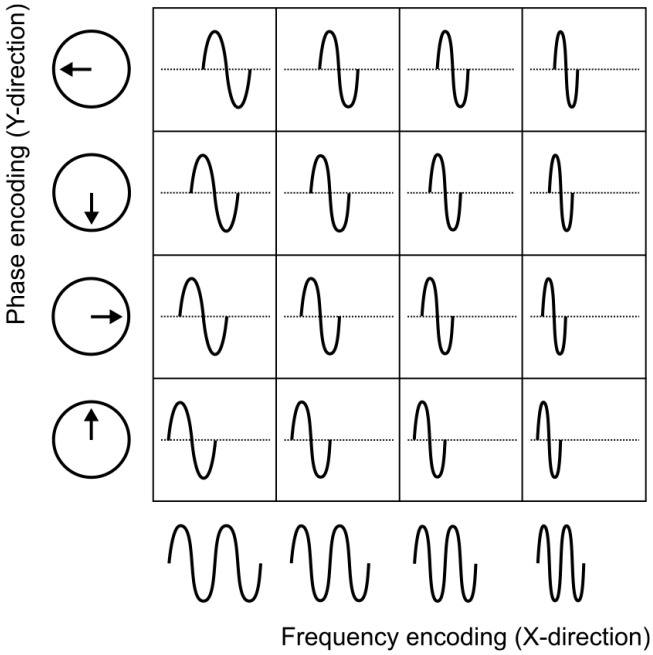

Figure 2.8: The principles of phase and frequency encoding displayed in a $4_x \times 4_y$ image. The locations in the x-direction is determined by the frequency and the y-direction locations are determined by the signal phase [64].

Figure 2.8 displays the principles of phase and frequency encoding displayed in a $4_x \times 4_y$ image. The locations in the x-direction is determined by the frequency and the y-direction locations are determined by the signal phase [64].

The $k-space$ is viewed as the Fourier transformation of the MR image. It represents the spatial frequency distribution of the MR image. In a $k-space$ the central parts contain the low spatial frequencies, the contrast in the image. The outer parts in a $k-space$ contain high spatial frequencies, which are the details and the edges [10]. Each coordinate, or point, in the $k-space$, is collected in a pulse sequence. There exist numerous ways to sample a $k-space$.

2.2.3 Pulse sequences

To reconstruct the spin density of an object the $k-space$ has to be sampled evenly. To achieve the required spatial resolution and coverage for this, it is sat well-defined constraints on the distance between consecutive samples, gradient strengths, and their duration, and the number of sample points in the $k-space$ [10]. The number of sample points in a $k-space$ is referred to as the matrix size. A pulse sequence is the process of applying gradients and RF pulses in a certain sequence at certain intervals to achieve the necessary sampling of a $k-space$.

Pulse sequence diagrams, also called timing diagrams, are used for the comparison of pulse sequences. It is a schematic representation of the basic steps performed by the different hardware components during the execution of the sequence. The elapsed time during the sequence is illustrated from left to right along the horizontal axis. The horizontal lines represent the different hardware; the RF transmitter, and each gradient. Often additional lines are added to represent hardware like analog-to-digital converter (ADC) sampling as well [12]. Figure 2.9 is an example of a diagram like this.

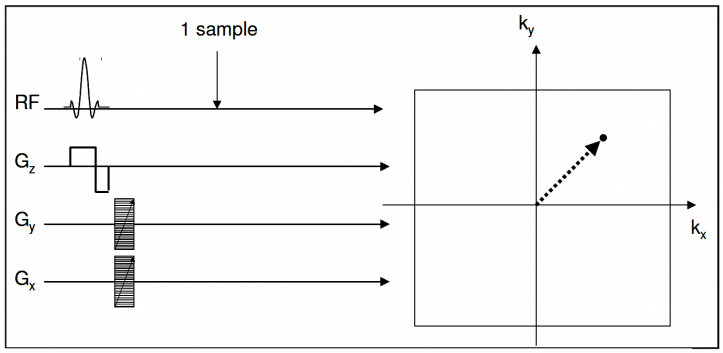

Figure 2.9: A simplified pulse sequence to obtain a single point in a $k-space$ [10].

A simplified pulse sequence diagram is shown in Figure 2.9. The combination of gradients applied in Figure 2.9 will acquire a single point in a $k-space$. It is not efficient to obtain a full $k-space$ with this method. It would have to be repeated $N_x \times N_y$ times to achieve an $N_x \times N_y$ matrix. It would acquire $N_x \times N_y$ RF pulses with a given time interval in-between each pulse [10]. This would be time-consuming and result in a high acquisition time. By sampling multiple $k-space$ points for each RF pulse, the acquisition time will be reduced considerably. This approach is used in all practical pulse sequences today, one of the main sequences is Spin Echo (SE) sequencing, which samples one line in the $k-space$ for each RF pulse.

In an SE sequence, the signal echo is generated by a second RF pulse, instead of switching the polarity of the read-out gradient, as in a gradient echo (GRE) sequence [10]. A 90° RF pulse is followed by a 180° RF pulse, which is often denoted as a refocusing pulse [12]. The purpose of the 180° RF pulse is the same as switching the polarity in GRE sequencing, to move the k-vector, as shown in Figure 2.10. In SE sequencing a refocusing pulse is required for every echo that is generated. To refocus the protons at the same time as the echo. SE sequencing also utilizes gradients of opposite polarization in the read-out and slice selection directions [12].

Figure 2.10 shows a pulse sequence diagram for a SE sequence. As shown the purpose of the 180° RF pulse is to invert the position in the $k-space$ from 1^{th} to 4^{th} quadrant, which enables the read-out of one k_x-line to be sampled in each TR-interval, where TR is the time interval between each 90° RF pulse [10]. Note that in Figure 2.10 the polarity of the G_x gradient is the

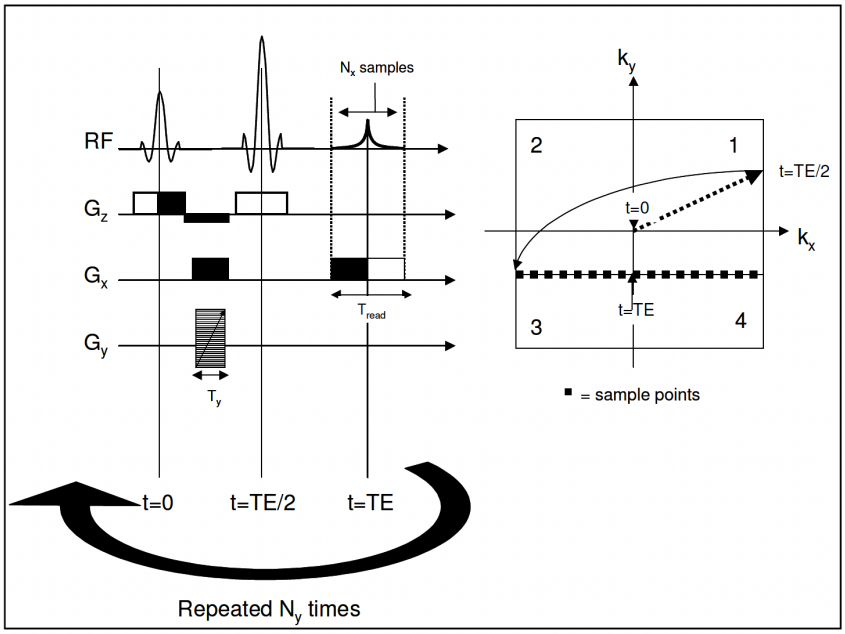

Figure 2.10: A SE sequence displayed in a pulse sequence diagram and the corresponding readout line in a k-space [10].

same before and after the 180° RF pulse, since a 180° RF pulse inverts the phase.

In Figure 2.10 it is shown that the sequence start at $[k_x, k_y] = [0,0]$. During the phase encoding, gradient G_y, the first phase encoding step moves the k-space position to $[0, k_{y,i}]$. Then by the first x-gradient, the system is moved to $[k_{x,max}, k_{y,i}]$. The 180° refocusing pulse then flips the system to the inverted position, $[-k_{x,max}, -k_{y,i}]$ before the first k-space line is recorded during the readout process with the frequency encoding gradient, G_x. The relationship between the k-space point separation (Δk_x and Δk_y) and the image FOV is expressed by Equation 2.29, where i is the spatial dimension in the x- or y-direction [64].

$$\Delta k_i = \frac{1}{FOV_i} \tag{2.29}$$

An image contains information in three directions. When averaged normal to the slice, the z-direction, the signal, S, is given by Equation 2.30, the two-dimensional Fourier transform of $\rho(x,y)$ [64, 10].

$$S(k_x, k_y) = \int_{-\infty}^{\infty} \int_{-\infty}^{\infty} \rho(x,y) e^{i2\pi(k_x x + k_y y)} dx dy \tag{2.30}$$

To reconstruction $\rho(x,y)$ from $S(k_x, k_y)$ a two-dimensional inverse Laplace transformation is performed, Equation 2.31 [64, 10].

$$\rho(x,y) = \int_{-\infty}^{\infty} \int_{-\infty}^{\infty} S(k_x, k_y) e^{i2\pi(k_x x + k_y y)} dk_x dk_y \tag{2.31}$$

2.3 Magnetic Resonance Spectroscopy

MRI is the most common application of MR phenomenon in clinics today, but NMR was the original application of MR [12]. MRS is a technique that can be used to investigate the structure, dynamics, and chemical kinetics of a wide range of biochemical systems [60]. The development of whole-body scanners has made it possible to study the biochemistry of diseases within a patient without the need for biopsies [12].

In MRS, contrary to MRI, relaxation effects are avoided as much as possible. The molecules that are observed in MRS studies are small in size and have relatively long T_1 and T_2 values. To minimize T_1 saturation effects, a long TR (from 1500 ms and up) is usually used [12].

The concepts of net magnetization produced by a collection of spins in a magnetic field, the signal production following the absorption of the RF energy, and the T_1 and T_2 relaxation are the same for MRS as described in Chapter 2.1. All of the molecules in a sample are detected in the same magnetic field, and the source of magnetic field variations in MRS comes from the chemical shifts and J-coupling between the spins. For MRI, water is detected. The water signal gives one singlet peak and is not coupled with other spins. The chemical shifts and coupling patterns are therefore not relevant in MRI.

2.3.1 Chemical shift

In MRS the different molecules are separated by the chemical shift differences between protons in different environments. The chemical shift is referred to as the resonance frequency of a nucleus measured to a reference frequency [12].

An important part of NMR spectroscopy is Chemical shielding. The absorption frequency of a nuclear spin depends on the magnetic field strength at the nuclei. The effective magnetic field, B_{eff}, is always lower than the applied field, $\vec{B_0}$. The precession of electrons during the applied magnetic field causes a shielding of the magnetic field strength by the electron density surrounding the nucleus resulting in an additional magnetic field usually opposing the applied field [60]. Equation 2.32 [60], gives the local magnetic field strength at the nuclei. In Equation 2.32, σ represents the shielding of the nuclear spin.

$$B_{eff} = (1 - \sigma) \cdot B_0 \tag{2.32}$$

When the electron density increases, the effective field decreases, which leads to lower resonance frequencies. This is the reason why the observed frequency is referred to as a chemical shift, the resonance frequency is dependent on the chemical environment of the nuclear spin [60].

To directly compare the position of resonance lines in spectra that are obtained at different field strengths, the position of the spectral lines is made independent of the magnetic field strength [60]. The spectral lines are made independent of the conversion from frequency to chemical shift, with the unit parts per million (ppm). This is done by Equation 2.33 [60, 33], where δ is the chemical shift in ppm, v is the frequency, and v_0 is a reference frequency.

$$\delta = \frac{v - v_0}{v_0} \cdot 10^{-6} \tag{2.33}$$

The reference frequency, v_0, is often the frequency of the line from a compound whose resonance is at one of the ends in the spectra. For ^1H tetramethylsilane (TMS) [60], or trimethylsilylpropanoic acid (TSP) are often used as a reference frequency set to zero ppm.

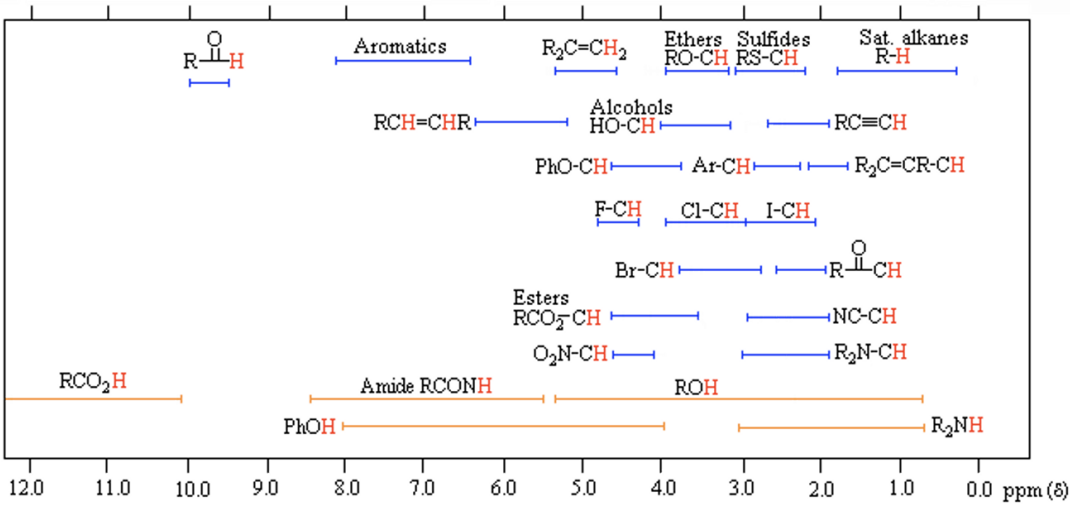

Figure 2.11: The chemical shift scale for ^1H [4].

To compare the spectra obtained from different field strengths, a chemical shift scale or a ppm (δ) scale is used. The chemical shift scale for protons, ^1H, is shown in Figure 2.11.

2.3.2 J-coupling

Another molecule interaction that affects the environment of a proton is the J-coupling, also referred to as spin coupling. Protons that are located on the same molecule will interact with each other through the chemical bond, and affect each other's local magnetic field. The spin coupling is independent of the magnetic field strength [12].

Spin coupling is a pairing interaction between spins on the same molecule, causing the MRS signal for each part to be divided. The number of signals and their relative amplitudes depend on the number of spins of each type [12]. The spins exchange information with nearby spins that are chemically equivalent, and the spins are either parallel (α) or anti-parallel (β) to $\vec{B}_0$. A summation of all the spin states leads to distinct splitting patterns separated by the splitting pattern [63].

The nomenclature that is used to describe the splitting amount between two spins is J, thereby the name J-coupling. A resonance line that is split due to a J-coupling is normally referred to as a multiplet. The effect the J-coupling has on the spectrum depends on the frequency separation of the spins, $\Delta\nu$ [60]. If the frequency difference between the two coupled spins is great, $\Delta\nu > J$, the system is referred to as an AX-system. The X signifies the great difference between the two spins. On the contrary, when coupled spins have nearly similar frequencies, $\Delta\nu \leq J$, the system is referred to as an AB-system, where the B signifies the vicinity of the coupled spins. When the coupled spins have identical resonance frequencies, $\Delta\nu = 0$, the observed coupling disappears [60]. When coupled spins don´t have identical resonance frequencies, the spins will develop a phase difference with a phase angle in a vector model given in Equation 2.34, where the θ is the angel and $t = TE$.

$$\theta = 2\pi Jt \tag{2.34}$$

The effect of first-ordered coupling on multiple spins on an NMR spectral line is easily obtained from Pascal´s triangle, illustrated in Figure 2.12.

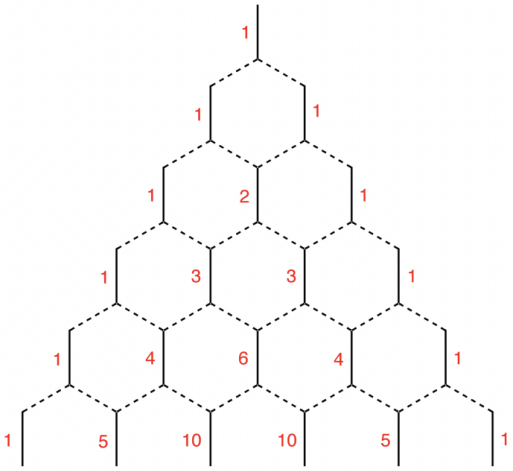

splitting pattern	the ratio of heights of llines in the peak
singlet	1
doublet	1:1
triplet	1:2:1
quartet	1:3:3:1
quintet	1:4:6:4:1
sextet	1:5:10:10:5:1

Figure 2.12: The NMR signal intensity distribution by Pascal´s Triangle [51]. The top of the triangle is the resonance line for a spin with no coupling partner, n=0, which gives a singlet. Each subsequent line represents the resonance line that would be obtained as a result of coupling to 1, 2, 3, ..., additional spins.

The description of the J-coupling already described is for spin coupled in a lower order. For higher-ordered coupled spins the density operator needs to be used to determine the coupling pattern of the spins. The details about the quantum mechanics of this can be read in "Understanding NMR Spectroscopy" by Keeler [33].

Quantum mechanics say that the properties of a nuclear spin can be gathered from its wavefunctions. An alternative to working directly with the wavefunctions is to use the density operator, Equation 2.35. An ensemble of a large number of spins can be calculated with the density operator [33].

$$\hat{\rho} = \overline{|\psi\rangle\langle\psi|} \tag{2.35}$$

The overbar indicates that an ensemble average is done. That means that the contributions from each spin in the sample are added and then divided by the number of spins. The wavefunctions $|\psi\rangle$ and $\langle\psi|$ are defined in Keeler [33] as,

$$|\psi\rangle = c_\alpha |\alpha\rangle + c_\beta |\beta\rangle \tag{2.36}$$

$$\langle\psi| = c_\alpha^* \langle\alpha| + c_\beta^* \langle\beta| \tag{2.37}$$

where α and β are spin states, and c_α and c_β are coefficients.

The density operator can be written as a linear combination of the basis operators [33],

$$\hat{\rho} = a_x(t)\hat{I}_x + a_y(t)\hat{I}_y + a_z(t)\hat{I}_z \tag{2.38}$$

where $\hat{I}_x$, $\hat{I}_y$ and $\hat{I}_z$ are the spin x-, y-, and z-angular momentum components, and a_x, a_y and a_z are numbers that vary with time, t, proportional to the respective magnetization components, Equation 2.39, 2.40 and 2.41 [33].

$$M_x(t) = a_x(t) \tag{2.39}$$

$$M_y(t) = a_y(t) \tag{2.40}$$

$$M_z(t) = a_z(t) \tag{2.41}$$

When the coefficients are known, the magnetization of the sample and its variation in time can be determined, and the density operator provides complete information about the spin system. To display how the magnetization varies with time, the density operator is expressed as a function of time, t, in Equation 2.42 [33].

$$\frac{d\hat{\rho}}{dt} = -i(\hat{H}\hat{\rho}(t) - \hat{\rho}(t)\hat{H}) \tag{2.42}$$

In Equation 2.42, $\hat{H}$ is known as the Hamiltonian operator which is an operator that represents the observable quantity energy, the ”hat” on the letter is added to display that the symbol represents an operator and not a function [33]. The Hamiltonian for a nuclear spin in a magnetic field, B_0, applied along the z-axis is written in Equation 2.43.

$$\hat{H}_{onespin} = -i\gamma B_0 \hat{I}_z \tag{2.43}$$

The solution of Equation 2.42 can be shown as,

$$\hat{\rho}(t) = \exp(-i\hat{H}t)\hat{\rho}(0)\exp(i\hat{H}t) \tag{2.44}$$

where $\hat{\rho}(t)$ is the density operator at time t and $\hat{\rho}(0)$ is the density operator at time zero [33].

2.3.3 Spin echo

How the chemical shifts and J-coupling affect the spectra can be explained with the vector model of a spin echo. Spin echo is one of the most famous pulsed NMR experiments, and it is a component in several more complex experiments [33].

After an RF pulse is applied to a spin system, the population difference between the energy levels in the spin system is affected. The spins will be affected by the chemical shift, the different distribution of electrons in the surroundings, and by the J-coupling, where the spins couple with their neighbor spin in the electron bindings. In the vector model, each peak in the specter is represented by a vector. Only one peak can be on resonance in the rotating coordination system, that vector will have the same frequency as the rotating coordination system, and therefore not develop a phase difference. A singlet signal and the signal at the reference will therefore not experience any phase shift. The rest of the peaks from the NMR spectrum will develop a phase difference in the vector model with a phase angel given in Equation 2.34, where the angel, θ, is the angle between the vectors in the system and t is in a spin echo sequence equal to $t = TE$.

Figure 2.13 displays the vector model for a non-coupled spin in a spin echo sequence. The initial 90° RF pulse aligns the magnetization vector for spin α along the y-axis, displayed in Figure 2.13a. During the first time interval, τ-delay, the magnetization vector precesses freely towards the x-axis, displayed in Figure 2.13b, with a phase angle given in Equation 2.34. The 180° RF pulse flips the magnetization vector to a mirror image position, Figure 2.13c, and during the second time interval, τ-delay, the vector continues to precess freely aligning itself along the y-axis, Figure 2.13d. Thus refocusing itself and making the magnetization vector independent.

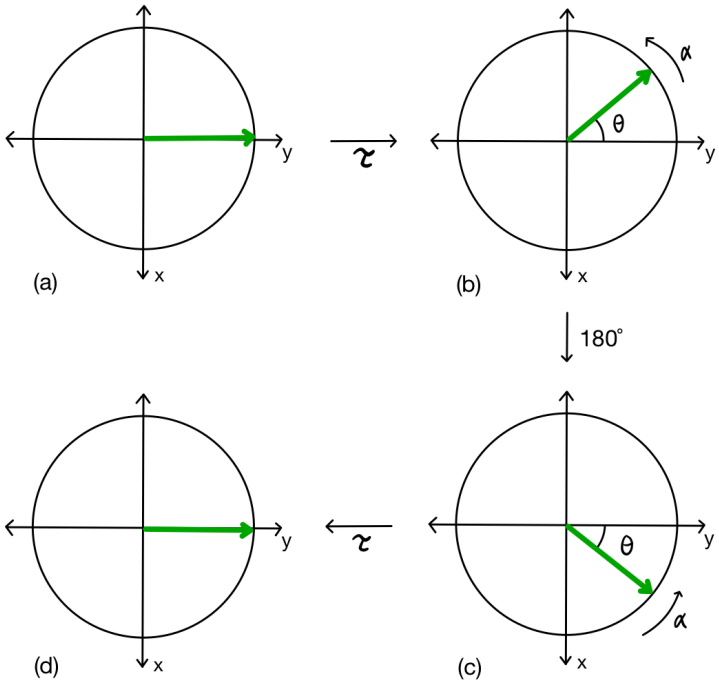

Figure 2.13: The vector model for a non coupled spin, α, in a spin echo sequence. The vector for spin α after a: 90° RF pulse (a), time τ (b), 180° RF pulse (c), and a time time τ (d).

The vector model for a coupled spin with a non-selective 180° RF pulse in a spin echo sequence is explained in Figure 2.14. The α represents the vectors coupled to the α population in the spins to the coupling partner for the vector, and β represents the β population in the spins to the coupling partner for the vector.

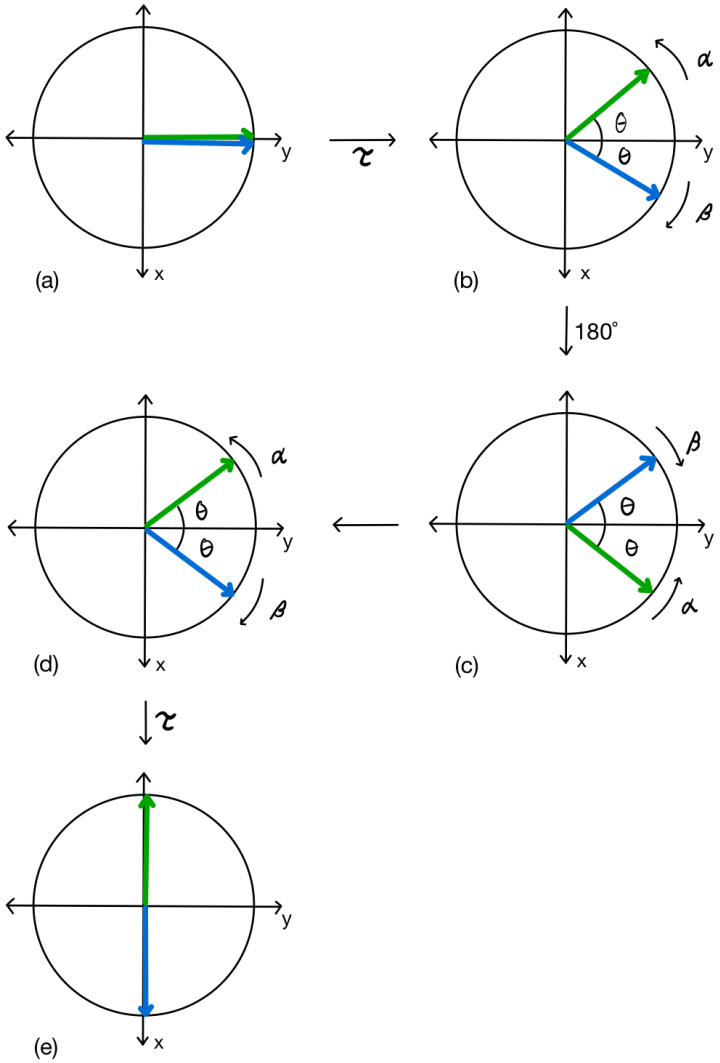

Figure 2.14: The vector model for a coupled spin with a non-selective 180° RF pulse in a spin echo sequence. The spin vectors parallel, α, and anti-parallel, β, after a: 90° RF pulse (a), time τ (b), 180° RF pulse (c, d), and a time τ (e).

After the 90° RF pulse the magnetization vectors for the α and β spins are aligned with the y-axis in the xy-plane, Figure 2.14a, and after a time interval, τ, the two vectors from the doublet has precessed towards the x-axis in its own direction, Figure 2.14b. When the 180° pulse is applied the vectors have mirrored the y-axis and they have switched places, Figure 2.14c, but since the coupled peaks also are affected, those spins, respectively α and β, are also switched and the phase angels are flipped again, Figure 2.14d. Resulting in no phase change by the 180° RF pulse, and the vectors phase continues as if the 180° RF pulse was not present, Figure 2.14e.

For a coupled spin with a selective 180° pulse in a spin echo sequence, Figure 2.15, are not both the coupled vector peaks affected, just the peak coupled to the reference. A selective RF pulse, soft pulse, is applied at a selected chemical shift, the reference peak, as explained in Chapter 2.1.3. The only signals affected by this type of RF pulse are the spins coupled to this reference. The phase angle for the vectors is therefore flipped, but the vectors are not mirrored on the y-axis, resulting in a refocusing of the resonance peaks but no other peaks in the spectrum. When the OFF and ON spectrum, OFF/ON selective pulses, are edited, the peaks not affected by the selective pulses will be equal to zero and the edited peaks will be refocused.

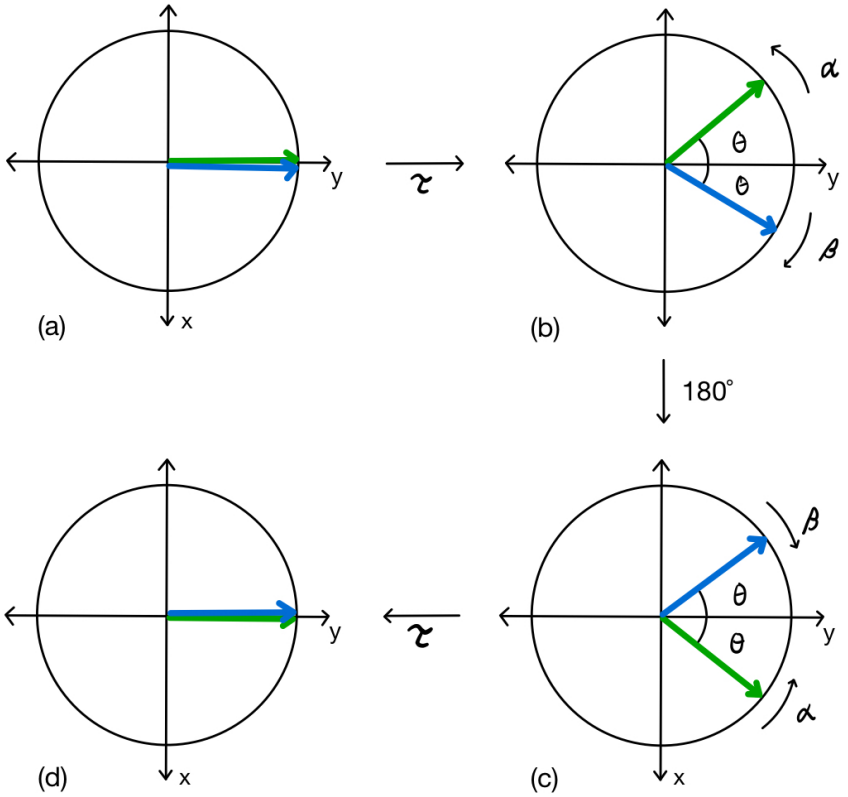

Figure 2.15: The vector model for a coupled spin with a selective 180° RF pulse in a spin echo sequence. The spin vectors α, parallel, and β, anti-parallel, after a: 90° RF pulse (a), time τ (b), 180° RF pulse (c), and a time τ (d).

In Figure 2.15 the vector model for a coupled spin with a selective 180° RF pulse in a spin echo sequence is displayed. After a 90° RF pulse, the magnetization vectors for spin α and β are aligned on the y-axis, Figure 2.15a. During the first time interval, τ, the magnetization vectors precesses freely towards the x-axis, displayed in Figure 2.15b, with a phase angle given in Equation 2.34. The 180° RF pulse flip the neighbouring spins α and β, so the α spin become a β spin and vice versa, Figure 2.15c. During the second time interval, τ, the vectors continue to precess freely aligning themselves along the y-axis, Figure 2.15.

2.3.4 Water suppression

In clinical MRI, the water and fat within a slice are visualized, this is feasible because of the high concentration of water and fat within the tissue. In MRS, the metabolites that are observed are 10 000 times less concentrated than water. This makes the detection of the metabolites in the presence of tissue water difficult. To accomplish the detection of metabolites, water suppression is utilized [12].

The most common water suppression method uses a frequency-selective RF pulse known as a Chemical shift selective (CHESS) pulse. The RF pulse is centered at the water resonance frequency to saturate the signals from the water protons. The water suppression factors are as high as 100 or more, which makes it an effective way of reducing the signal contamination from water [12]. A frequently used water suppression method today is the VAPOR technique. The VAPOR technique consists of 7 selected CHESS-pulses of variable power and optimized timing. The technique efficiently suppresses the water signal in spite of B_1 inhomogeneities of the surface coil. It permits the detection of signals in nearly the whole chemical shift scale, including signals close to the water signal [67].

2.3.5 Localization techniques

The spatial localization techniques used in MRS are similar to the ones used in MRI. To localize the RF energy to the desired volume, slice selective excitation pulses together with gradient pulses are used in the same way as described in Chapter 2.2. There are two different types of localization techniques in MRS, single voxel techniques and multiple voxel techniques. Single voxel techniques are the only ones used in this thesis.

Single voxel techniques acquire spectra from a single small volume through the intersection of three slice-selective RF excitation pulses [12]. Two of the most common approaches are the pulse sequences PRESS and STEAM, where PRESS uses a 90° and two 180° RF pulses, while STEAM uses three 90° RF pulses. Each pulse is applied with a different physical gradient as the slice selection. The stimulated echo is produced by the protons located at the intersection of the pulses [12].

In this thesis, the PRESS sequence was used, along with the MEGA-PRESS and sLaser sequences.

2.3.6 PRESS

A Point RESolved Spectroscopy (PRESS) sequence is built on the spin echo sequence with two 180° refocusing pulses. It is a single voxel spin echo technique with slice selective gradients, G_z, G_y and G_x. The protons in the intersection are the only ones who go through excitation at the desired TE due to the applied gradients [12]. This sequence produces a complete three-dimensional volume selection with the aid of one voxel. The PRESS technique uses a double echo: one 90° excitation pulse and two 180° refocusing pulses, as shown in Figure 2.16. The VAPOR pulse is used for water suppression, and it is explained in Chapter 2.3.4. The pulse is centered at the water resonant frequency to saturate the water protons [12].

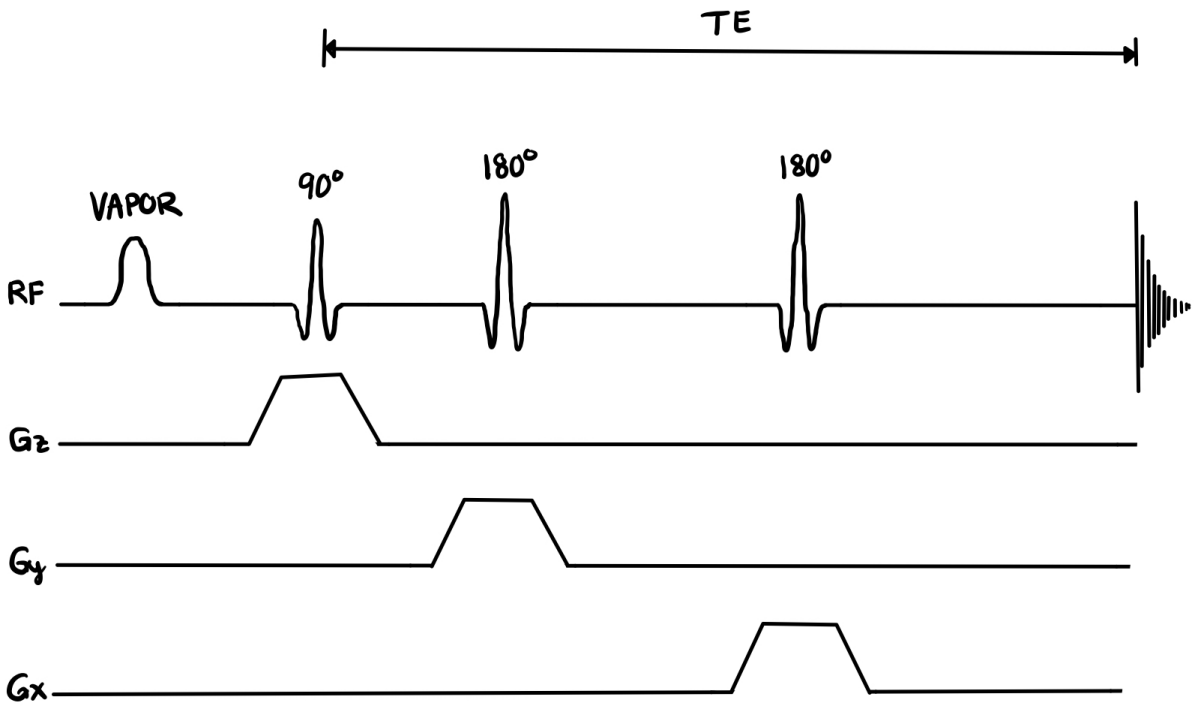

Figure 2.16: Pulse diagram for the PRESS sequence with three slice selective gradients, G_z, G_y, and G_x, and the water suppression pulse, VAPOR. Drawing inspired by the pulse diagram for PRESS by Brown and Semelka [12].

A PRESS sequence consists of normal slice selective gradients as explained. The 180° pulses have limited bandwidth to select the desired voxel, but the pulses are therefore selective and the signals far away from the resonance peak, water at 4.7 ppm, will not experience a full 180° refocusing pulse. Those signals will therefore not be flipped exactly 180° as explained in the spin echo sequence. In order to affect the whole spectrum with the refocusing pulses, adiabatic pulses are applied in a pulse sequence called sLaser.

2.3.7 sLaser

sLaser consists of 180° adiabatic selective refocusing pulses. An adiabatic pulse utilizes the adiabatic principle and is an amplitude- and frequency-modulated RF pulse that is relatively insensitive to B_1 inhomogeneity and frequency offset effects. In the adiabatic principle the magnetization, $\vec{M}$, is manipulated slowly which results in a manipulation of the spins with different resonance frequencies at different times. The sample is placed inside the static magnetic field, $\vec{B_0}$, as normal. The RF field is then applied very gradually, with a constant magnitude of B_1, and a gradually increasing frequency, ω, from below resonance to beyond. The magnetization precess the effective magnetization field, B_{eff}. When the frequency is beyond the resonance, the full magnetization will be 180° inverted, and all the spins have been affected [23, 1, 2]. The pulse diagram for the pulse sequence sLaser is depicted in Figure 2.17.

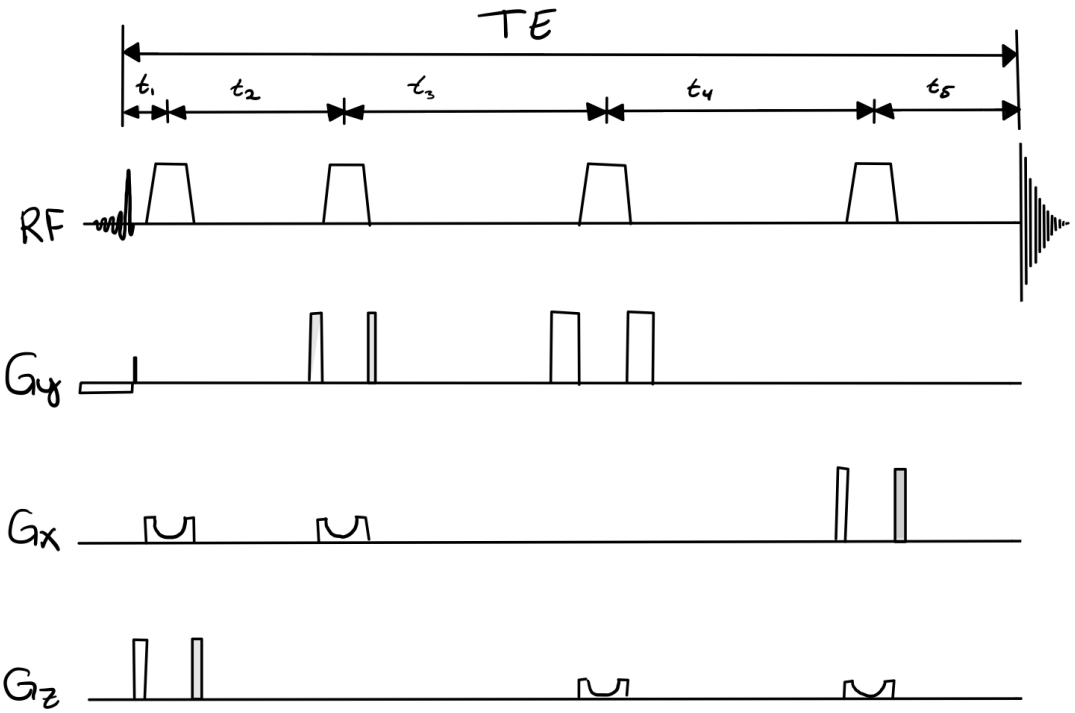

Figure 2.17: Pulse diagram for the sLASER sequence. Drawing inspired by Shams et al. [62].

2.3.8 MEGA-PRESS

MEscher-GArwood Point RESolved Spectroscopy (MEGA-PRESS) is a common editing pulse sequence used to edit spectra with metabolites overlapping the desired metabolite signals, its pulse diagram is displayed in Figure 2.18 [27].

A MEGA-PRESS sequence has a pair of frequency-selective editing pulses that refocus the evolution of the coupling, as explained for a coupled spin echo with selective 180° pulses displayed in Figure 2.15, in half of the transients, the ON-edit spectra. In the ON-spectra the editing pulse is applied on the neighbouring spins to the desired signal. The difference of the subtracted spectra with and without the refocusing pulse subtracts the overlapping metabolites to the metabolite of interest [27].

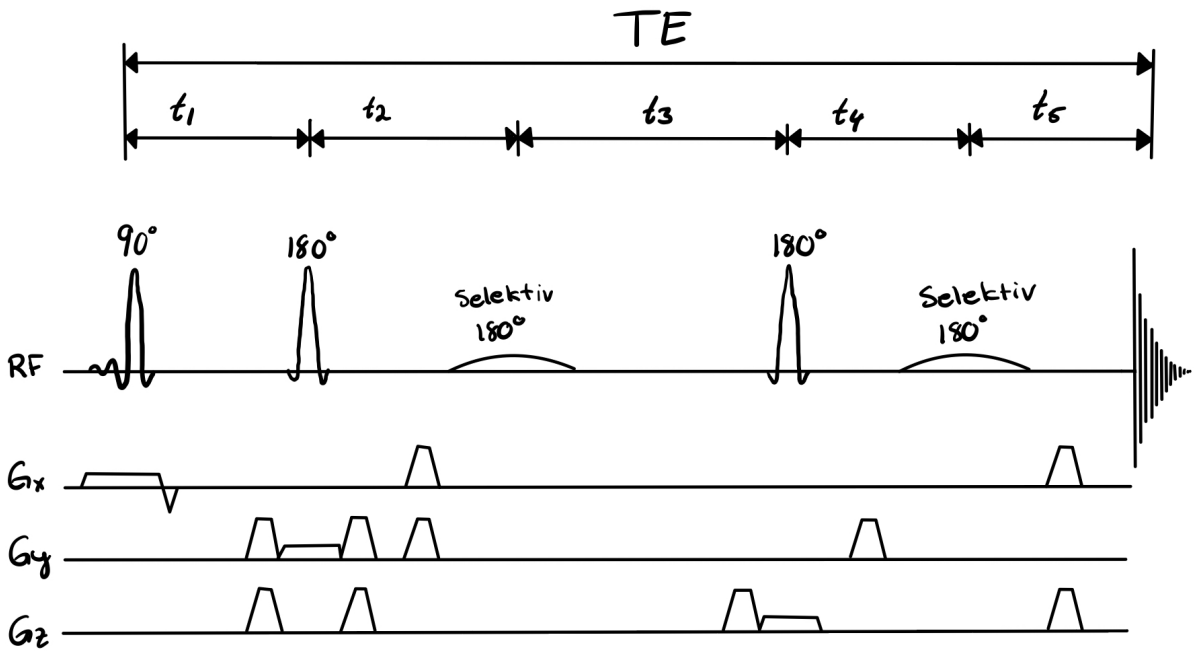

Figure 2.18: Pulse diagram for the MEGA-PRESS sequence with three non-selective RF pulses: one 90°, and two 180°, and two selective RF pulses, 180°. The drawing is inspired by the pulse diagram from Harris et al. [27].

The MEGA-PRESS sequence consists of, as explained, one 90° RF pulse, two 180° non-selective RF pulses, and two selective 180° RF pulses. The three non-selective RF pulses are used to select the voxel, as explained earlier. A non-selective 180° pulse behaves like a hard pulse, affecting the whole spectrum. The selective 180° pulses are used to edit the desired signal peaks in the spectrum.

In a MEGA-PRESS sequence for a doublet the edit-ON and edit-OFF affect the peaks in a specter as depicted in Figure 2.19. The edit-OFF spectrum is withdrawn from the edit-ON spectrum, resulting in an amplification in SI for the edited peaks.

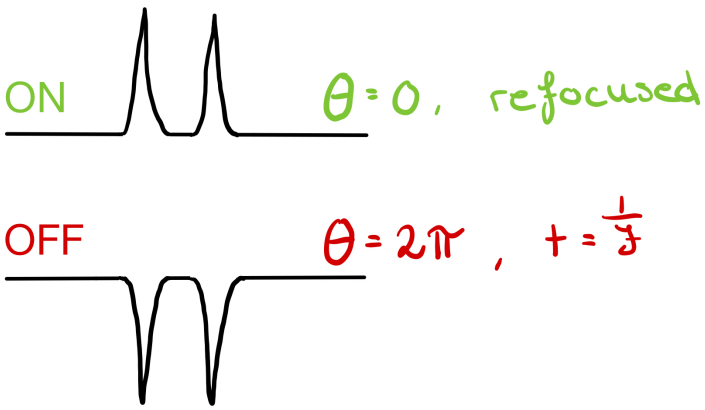

Figure 2.19: How the edit-ON and edit-OFF RF pulses affect the doublets in a spectrum.

2.3.9 Ultrahigh Magnetic field

MRS examinations benefit significantly from the use of ultrahigh B_0 fields. As previously mentioned, the net magnetization M is directly proportional to the static magnetic field B_0. A high static magnetic field increases the chemical shift difference, enhancing spectral resolution between different metabolites. Additionally, a high magnetic field results in narrower spectral linewidths, leading to an increased S/N ratio [12]. The heightened B_0 field also improves spatial resolution by allowing for smaller voxels to be scanned, resulting in MR spectra with equivalent S/N ratios using fewer signal averages, which can lead to shorter scan times [12].

The MR fields used in clinical settings today typically range from 1.5 T to 3 T. Some clinics have magnetic fields of 7 T; in Norway, Trondheim University Hospital is the only clinic using a 7 T scanner as of March 2024. While ultrahigh magnetic fields offer advantages in separating metabolites, as explained earlier, excessively high magnetic fields are not possible for clinical applications due to radiation exposure. For phantom analysis, however, an ultrahigh magnetic field is desirable. In this thesis, magnetic fields ranging from 60 MHz to 600 MHz are used, with 600 MHz corresponding to a magnetic field of 14.1 T [55].

Chapter 3

Materials and Methods

This chapter outlines the experimental parameters for the MRS analysis of pure 2HG and 2HG in a brain metabolite solution using two different buffers. The analyses were conducted at various magnetic field strengths: 60 MHz, 500 MHz, and 600 MHz at NNP in the Department of Chemistry at UiB, and at 3 T at HUS. Additionally, it covers the creation and use of a 3D-printed phantom designed for data analysis at 3 T at HUS, as well as Python simulations of 1D 2HG spectra.

3.1 Materials

The parameters of all solids and liquids used in this thesis are summarized in Table 3.1 and 3.2.

Table 3.1: Parameters for all solid compounds used in this thesis

Solids	Molar mass [g/mol]	Purity	Provider
2HG	192.08	$\geq 95\%$	Sigma-Aldrich
m-Ins	180.16	$\geq 99.0\%$	Sigma-Aldrich
Lac	112.06	$\geq 99.1\%$	Sigma-Aldrich
Cr	149.15	$\geq 98\%$	Sigma-Aldrich
NAA	175.14	$\geq 99.0\%$	Sigma-Aldrich
Cho	139.62	$\geq 99\%$	Sigma-Aldrich
GABA	103.12	$\geq 99\%$	Sigma-Aldrich
Glu	187.13	$\geq 98\%$	Sigma-Aldrich
TSP	172.27	98%	Sigma-Aldrich
NaN_3	65.01	$\geq 99.5\%$	Sigma-Aldrich
Na_2HPO_4	141.96	-	Sigma-Aldrich
$HNa_2O_4P \cdot 7H_2O$	268.07	$\geq 99\%$	Sigma-Aldrich
$NaH_2PO_4 \cdot H_2O$	137.99	$\geq 99\%$	Sigma-Aldrich
Sucrose	342.20	-	Eldorado

Table 3.2: Parameters for all liquid compounds used in this thesis

Liquids	Molar mass [g/mol]	Purity	Provider
Clariscan	558.6	-	GE Health Care AS
D_2O	20.03	99.0%	Sigma-Aldrich
Distilled water	18.02	-	UiB
Grease	-	-	HUS

The equations used for the mass and dilution calculations in the method are expressed in Equation 3.1, and Equation 3.2.

$$m = c \cdot Mm \cdot V \tag{3.1}$$

$$V_1 = \frac{c_2 \cdot V_2}{c_1} \tag{3.2}$$

(a) (b) (c) (d)

Figure 3.1: The MR machines used in this thesis are a: 60 MHz Nanalysis (a), 3 T GE scanner (b), 500 MHz Bruker BioSpin (c), and 600 MHz Bruker BioSpin (d).

The machines used in this thesis are displayed in Figure 3.1. Figure 3.1a shows the 60 MHz Nanalysis NMR machine. Figure 3.1b displays the 3 T GE scanner at HUS, used for research and clinical purposes. Figure 3.1c features the 500 MHz wide-bore AVANCE III HD spectrometer from Bruker BioSpin, which is used with the MICWB40 micro-imaging probehead and a MICRO2.5 gradient system (2.5 G/cm/A) with amplifiers (X, Y, Z) 2xGREAT-60 (60A). The software ParaVision is used for multi-dimensional MRI/MRS data acquisition, reconstruction, analysis, and visualization [46]. Finally, Figure 3.1d shows the 600 MHz AVANCE NEO spectrometer from Bruker BioSpin, equipped with a QCI-P CryoProbe (^1H, ^2H, ^{13}C, ^{15}N, and ^{31}P) and an automatic sample changer (SampleJet) [46].

3.2 Sample preparation

The samples were prepared shortly before the experiments to ensure they were as fresh as possible. The solutions were made with two different buffers, but primarily with the Plasma/Serum buffer. Details about the buffer solutions are explained in Chapter 3.2.1. An overview of the samples, including buffers, field strengths, and pulse sequences used, is displayed in Table 3.3. The mass of metabolites for each sample was added to the respective buffer solution. The molar mass of 2HG is 192.08 g/mol [18].

Table 3.3: Sample overview

No.	*Solution*	$[mM]$	*Buffer*	Field	Seq.
1	2HG	10,0	Phosphate	500 MHz	PRESS, MEGA-PRESS
2	2HG	10,0	Plasma/Serum	60 MHz, 600 MHz	sLaser, COSY, J-RES
3	2HG, BRAINO	5,0	Plasma/Serum	600 MHz	sLaser, COSY, J-RES
				500 MHz	PRESS
4	2HG	10,0	Phosphate	60 MHz, 600 MHz	sLaser
5	2HG	100,0	Plasma/Serum	60 MHz	sLaser
6	2HG	10,0	Plasma/Serum	500 MHz	PRESS MEGA-PRESS
7	2HG	20,0	Plasma/Serum	500 MHz	PRESS MEGA-PRESS
8	2HG	40,0	Plasma/Serum	500 MHz	PRESS MEGA-PRESS
9	2HG	60,0	Plasma/Serum	500 MHz	PRESS MEGA-PRESS
10	2HG	80,0	Plasma/Serum	500 MHz	PRESS MEGA-PRESS
11	2HG	2,0	Plasma/Serum	500 MHz	PRESS MEGA-PRESS
12	2HG	4,0	Plasma/Serum	500M Hz	PRESS MEGA-PRESS
13	2HG	6,0	Plasma/Serum	500 MHz	PRESS MEGA-PRESS
14	2HG	8,0	Plasma/Serum	500 MHz	PRESS MEGA-PRESS
15	2HG, BRAINO	2,0	Plasma/Serum	500 MHz	PRESS MEGA-PRESS
16	2HG, BRAINO	4,0	Plasma/Serum	500 MHz	PRESS MEGA-PRESS

Continued on next page

Table 3.3 – continued from previous page

No.	*Solution*	$[mM]$	*Buffer*	Field	Seq.
18	2HG, BRAINO	6,0	Plasma/Serum	500 MHz	PRESS MEGA-PRESS
19	2HG, BRAINO	8,0	Plasma/Serum	500 MHz	PRESS MEGA-PRESS
20	2HG, BRAINO	10,0	Plasma/Serum	500 MHz	PRESS MEGA-PRESS
21	Electrical tape	-	-	600 MHz	sLaser
22	Parafilm	-	-	600 MHz	sLaser
23	Loctite	-	-	600 MHz	sLaser
24	BRAINO	-	Plasma/Serum	3 T, 600 MHz	sLaser, PRESS, MEGA-PRESS, Asym,-PRESS, Short-STEAM
25	2HG	2,0	Plasma/Serum	3 T	sLaser, PRESS, Asym.-PRESS, Short-STEAM
				600 MHz	sLaser
26	2HG	4,0	Plasma/Serum	3 T	sLaser, PRESS, Asym.-PRESS, Short-STEAM
				600 MHz	sLaser
27	2HG	8,0	Plasma/Serum	3 T	sLaser, PRESS, MEGA-PRESS, Asym.-PRESS, Short-STEAM
				600 MHz	sLaser
28	Electrical tape	-	Plasma/Serum	600 MHz	sLaser
29	Ping pong ball	-	Plasma/Serum	600 MHz	sLaser
30	NAA, Glu	12,5 12,5	Plasma/Serum	3 T	sLaser, PRESS, Asym.-PRESS, Short-STEAM
31	2HG, NAA, Glu	4,0 12,5 12,5	Plasma/Serum	3 T	sLaser, PRESS, Asym.-PRESS, Short-STEAM
32	2HG, BRAINO	4,0	Plasma/Serum	3 T	sLaser, PRESS, MEGA-PRESS,

Continued on next page

Table 3.3 – continued from previous page

No.	*Solution*	$[mM]$	*Buffer*	Field	Seq.
					Asym.-PRESS, Short-STEAM
33	Glu	12,5	Phosphate	60 MHz	sLaser
34	2HG, Clariscan	4,0 0,5	Plasma/Serum	3 T	sLaser, PRESS, MEGA-PRESS, Asym.-PRESS, Short-STEAM
35	2HG, NAA, Glu, Clariscan	4,0 12,5 12,5 0,5	Plasma/Serum	3 T	sLaser, PRESS, MEGA-PRESS, Asym.-PRESS, Short-STEAM
36	2HG, BRAINO, Clariscan	4,0 0,5	Plasma/Serum	3 T	sLaser, PRESS, MEGA-PRESS, Asym.-PRESS, Short-STEAM

3.2.1 Buffer solutions

Inside the brain, the pH is 7.4. Since these analyses aim to determine the best method to detect 2HG in the brain, the pH of the samples was adjusted to 7.4.

To achieve a pH of 7.4 in the samples, a buffer was used, primarily a Plasma/Serum buffer. This Plasma/Serum buffer is typically diluted 50:50 with Plasma/Serum for blood analysis. In these experiments, the Plasma/Serum buffer was diluted 50:50 with distilled water. The Nanalysis machine, with a field strength of 60 MHz, does not have effective water saturation capabilities. Therefore, a buffer solution with minimal H_2O was created using D_2O and a phosphate buffer.

Plasma/Serum-buffer

The Plasma/Serum buffer was prepared with the compounds from Table 3.4.

Table 3.4: Compounds of Plasma/Serum buffer

Compound	Chemical formula	Concentration
Disodium phosphate	$Na_2HPO_4x7H_2O$	75 mM
TSP	$(CH_3)_3SiCD_2CD_2CO_2Na$	4.6 mM
Sodium azide	NaN_3	6.1 mM 0.04 %
Deuterium oxide	D_2O	20 %

10.05 g of $Na_2HPO_4 \cdot 7H_2O$ was dissolved in 380 mL of H_2O, 0.4 g of TSP was added, and the solution was mixed ultrasonically. Then, 5 mL of a 4% NaN_3/H_2O solution was added. The pH was adjusted to 7.4 with 1 M HCl/NaOH. The bottle was filled up to 400 mL with H_2O, and 100 mL of D_2O was added before the solution was mixed well.

The Plasma/Serum buffer was diluted 50:50 with distilled water, resulting in 10% deuterium. The 10% deuterium is present to enable the use of a deuterium lock.

Phosphate buffer in D2O

The phosphate buffer with deuterium oxide, D_2O, was prepared from [52] in accordance with Table 3.5.

Table 3.5: Preparation of phosphate buffer

Compound	Mm [g/mol]	m_r [g]	c_r [mol/L]
$HNa_2O_4P \cdot 7H_2O$	268.07	0.6716	0.07541
$NaH_2PO_4 \cdot H_2O$	137.99	0.1672	0.02459
NaN_3	65.01	0.0195	$6.5 \cdot 10^{-3}$

Sodium azide, NaN_3, was added to prevent the growth of bacteria in case the sample needed increased durability.

The buffer solutions were kept at 4°C.

3.2.2 Brain metabolite solution

The preparation of the brain metabolite solution also referred to as the BRAINO solution, was done in accordance with Table 3.6. To make the environment as realistic as possible a Plasma/Serum buffer was used to keep the pH to a physiological level of 7.4.

Table 3.6: Experimental data for a brain metabolite solution in a volume of 250 mL

Compound	Mm [g/mol]	m_r [g]	c_r [mol/L]
Cr	149.15	0.3722	$10.0 \cdot 10^{-3}$
Cho	139.62	0.1047	$3.0 \cdot 10^{-3}$
NAA	175.14	0.5482	$12.5 \cdot 10^{-3}$
m-Ins	180.16	0.3353	$7.4 \cdot 10^{-3}$
Glu	187.13	0.5906	$12.6 \cdot 10^{-3}$
Lac	112.06	0.1453	$5.2 \cdot 10^{-3}$
GABA	103.12	0.0515	$2.0 \cdot 10^{-3}$

The typical data from Table 1.1 was used for the calculations for the data in Table 3.6.

3.3 Pulse sequences

To analyze 2HG, different pulse sequences, and different field strengths have been used. Table 3.7 shows an overview of the different pulse sequences used at the different field strengths.

Table 3.7: Overview of different pulse sequences used to analyze 2HG at the different field strengths.

Pulse sequence	60 MHz	500 MHZ	600 MHZ	3 T
spin echo	✓	-	✓	-
PRESS	-	✓	-	✓
MEGA-PRESS	-	✓	-	✓
sLaser	-	-	-	✓
COSY	-	-	✓	-

The main pulse sequences used to analyze 2HG are a spin echo, PRESS, MEGA-PRESS, and sLaser, and the different field strengths used for the analysis are 60 MHz, 500 MHz, 600 MHz, and 3T. COSY was used to detect the J-coupling system of the protons in 2HG. The pulse diagrams for the spin echo, PRESS, MEGA-PRESS, and sLaser sequences are explained in Chapters 2.3.3 and 2.3.6-2.3.8 and displayed in Figure 2.10, 2.16, 2.18, and 2.17 respectively.

The spin echo data acquired at 60 MHz and 600 MHz are compared to the sLaser data from the 3T. This comparison is possible because of the small sample size used in the 60 MHz and 600 MHz NMR machines. The whole sample is assumed to be affected equally by the RF pulses and can be related to a sLaser sequence, which uses adiabatic pulses that affect the entire sample equally.

Table 3.8 and Table 3.9 display the experimental parameters for the spin echo, PRESS, MEGA-PRESS, and sLaser sequences. The spin echo sequence acquired at 60 MHz is referred to as the Hahn echo at the 60 MHz Nanalysis. The script for the spin echo sequence used at 600 MHz can be found in Appendix B. The TE times used for spin echo and PRESS range from 0 ms to 200 ms, and for sLaser, they are 30 ms, 80 ms, and 100 ms to 150 ms. For MEGA-PRESS, the TE times used during the experiments for the calibration curves are 60 ms, 74 ms, 80 ms, 97 ms, and 110 ms.

Table 3.8: Overview of the parameters used in the pulse sequences: PRESS, MEGA-PRESS and sLaser (* standard parameters at GE 3 T scanner at HUS used).

Parameters	PRESS	MEGA-PRESS	sLaser
TR [ms]	2500	5000	2500
AQ [s]	1.5	1.5	*
Voxel [mm^2]	$3 \times 3 \times 3$	$3 \times 3 \times 3$	$30 \times 30 \times 30$
Avg.	256	512	96
AQ points [k]	16384	16384	*

Table 3.9: Overview of the parameters used in the spin echo sequence on: 60 MHz and 600 MHz

Parameters	60 MHz	600 MHz
TR [*ms*]	3500	3750
AQ [*s*]	2.8	2.8
Avg.	1024	8
AQ points [k]	4096	65 536

3.4 Spectral analysis

The data analysis tools used in this study include the software package TopSpin 4.3.0 for the in-house machines at NNP, the 60 MHz, 500 MHz, and 600 MHz systems, and the software packages LCModel, Osprey, and Gannet for analyzing the 3T data acquired at Haukeland University Hospital (HUS). The software packages LCModel, Osprey, and Gannet were downloaded with the assistance of Alex Craven [16], from the Medical Technology department at HUS.

3.4.1 TopSpin

The data analysis tool used to analyze the data from the 60 MHz, 500 MHz, and 600 MHz systems was the software TopSpin 4.3.0.

TopSpin is Bruker's standard NMR software. It can be used for spectrometer control, as well as the processing and analysis of multidimensional NMR spectra [68]. In this thesis, the in-house software TopSpin 3.1PV was used for the control of the 600 MHz spectrometer, while ParaVision 6.0.1 was used for MRI control of the Bruker BioSpin 500 WB system. For post-processing and analysis of the NMR spectra from the 60 MHz, 500 MHz, and 600 MHz systems, TopSpin 4.3.0 was used.

During the processing and analysis of data acquired from the 60 MHz, 500 MHz, and 600 MHz systems, the NMR spectra were phase and baseline corrected using the commands *.ph* and *bas* integrated in TopSpin, and then further manually integrated in TopSpin. The manual integration in TopSpin yields a signal intensity (SI) relative to the initially integrated peak. Therefore, the integration of each spectrum was done systematically.

3.4.2 LCModel

LCModel is a commercially available analysis tool and is one of the most widely used software for MRS data analysis. It consists of codes operating in MATLAB R2024a [41], and with some code corrections done by Alex Craven [16], the Linux-operating LCModel software was made to work on MacOS for phantom data. LCModel was run through Osprey, utilizing Osprey's control sets.

The raw data, in p-file format, from the 3 T GE Scanner at HUS were post-processed with LCModel version 6.3 [35, 36], using a simulated basis set for 3 T brain spectroscopy from MRSCloud at MRICloud [42]. The basis sets were simulated for the PRESS and sLASER sequences with the analyzed echo times and included metabolites. LCModel processing included Fourier transformation (FT), phase correction, and baseline correction. This analysis process

was performed for each spectrum. The TSP peak at 0 ppm was used as an internal standard, with the same concentration for all the experiments performed at the 3 T GE scanner at HUS.

As Harris et al. explained, ”The LCModel has a ’black-box’ approach, it does not have retrospective frequency correction and depends on previous knowledge of the individual metabolite spectra with the used acquisition parameters (to form a basis set) to fit the edited signals” [27]. Because of this ”black-box” approach, LCModel was not selected for the analysis of the data acquired at NNP. The ”black-box” approach for the accumulation of the basis sets includes the density operator explained in Chapter 2.3.2.

3.4.3 Osprey

For the quantification of 2HG and other metabolites from the 3 T phantom data, the software package Osprey was used on the raw data. The software package was downloaded from Alex Craven’s GitHub repository ”osprey” [16].

Osprey was developed by Georg Oeltzschner, Helge J. Zöllner, Steve C.N. Huia, Mark Mikkelsen, Muhammad G. Saleh, Sofie Tapper, and Richard A.E. Edden in 2020. It is an open-source software environment for the pre-processing, linear-combination modeling, quantification, and visualization of MRS data [49]. The Osprey code is based on simple commands in MATLAB R2024a [41], and the software package is built on the functions and organizational structure of FID-A [49].

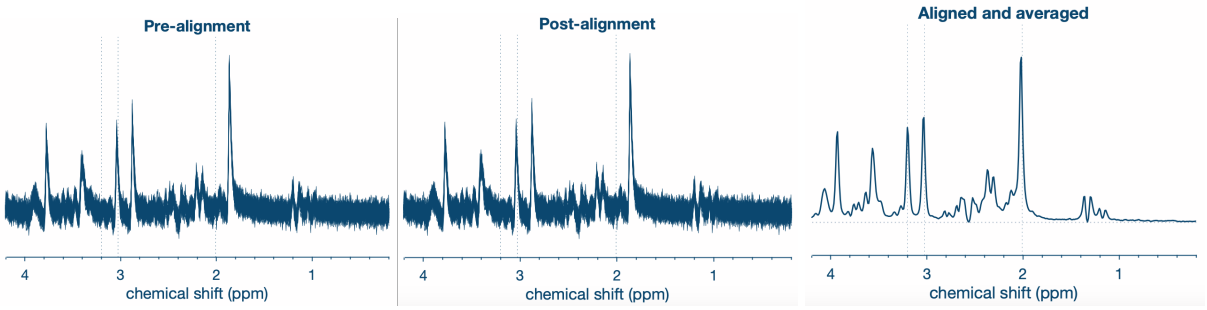

(a) (b) (c)

Figure 3.2: How the processes in the Osprey software affect a spectrum: raw data before alignment (a), after alignment (b) and averaged spectrum (c).

The raw data from the 3 T GE Scanner at HUS were loaded into the Osprey software package, along with a simulated basis set for 3 T brain spectroscopy from MRSCloud at MRICloud [42]. The basis sets were simulated for the PRESS and sLASER sequences with the analyzed echo times and included metabolites. As explained, the density operator was used to generate the basis sets. After the raw data were loaded, Osprey processed the data. The processing is similar to a ”black box” like the LCModel software. During processing, the data were aligned and averaged to reduce noise and align the peaks from each scan. After processing, the data were modeled and quantified based on the basis sets from MRSCloud [42]. Figure 3.2 shows how an example spectrum behaves: before alignment, raw data, Figure 3.2a, and after alignment, Figure 3.2b, and after the averaging, Figure 3.2c.

3.5 Calibration curves

Calibration curves for 2HG were constructed using two different sets of 2HG samples. The first set contained five samples of pure 2HG in Plasma/Serum buffer with increasing concentrations from 2-10 mM. The second set contained five samples of increasing 2HG concentration from 2-10 mM in a brain metabolite solution and Plasma/Serum buffer. For each set of samples, the calibration curves were constructed by increasing the 2HG concentration while keeping the concentration of other metabolites constant.

The samples were analyzed in 10 mm NMR tubes on a Bruker BioSpin 500 WB system using a MICWB40 micro-imaging probe head. For MRI/MRS data acquisition, reconstruction, and analysis, the in-house software ParaVision 6.0.1 and TopSpin 4.3.0 were used. After manual tuning and matching of the probe, an initial slice-selective MRI sequence, FLASH, was used to place the voxel in the sample and check for any physical inhomogeneities such as air bubbles that could interfere with the signal. The magnetic homogeneity in the sample was determined by a B_0-mapping procedure, and to achieve maximal magnetic homogeneity inside the region of interest, a subsequent localized shimming routine was performed. The water signal was suppressed for each sequence using the VAPOR sequence, a built-in function in ParaVision.

Following this preparation, the MEGA-PRESS experiments (ON/OFF) were run for each sample in every set. The spectra were processed and manually integrated in TopSpin 4.3.0, and the calibration curves were created in Microsoft Excel.

The manual integration in TopSpin yields an SI relative to the initially integrated peak. Therefore, the TSP peak with a constant concentration in the Plasma/Serum buffer at 0 ppm was systematically chosen as the first integral. For the calibration curve calculations, the absolute values from the integrals were used.

3.5.1 Calibration curve for 2-10 mM 2HG

The samples used for the calibration curve for 2-10 mM 2HG were diluted from the sample numbers 7-10 in Table 3.3 according to Table 3.10. For the calculation for the dilution, Equation 3.2 was used.

The samples used for the calibration curve for 2-8 mM 2HG were used in order to utilize as much of the 2HG product as possible. The sample with 10 mM 2HG was sample number 6 from Table 3.3.

Table 3.10: Experimental data for the dilution of the samples of 10-80 mM 2HG to the calibration of 2-8 mM 2HG

c_2 [mol/L]	V_2 [L]	c_1 [mol/L]	V_1 [L]
$2.0 \cdot 10^{-3}$	$2 \cdot 10^{-3}$	$19.97 \cdot 10^{-3}$	$2.0035 \cdot 10^{-4}$
$4.0 \cdot 10^{-3}$	$2 \cdot 10^{-3}$	$39.93 \cdot 10^{-3}$	$2.0035 \cdot 10^{-4}$
$6.0 \cdot 10^{-3}$	$2 \cdot 10^{-3}$	$59.90 \cdot 10^{-3}$	$2.0035 \cdot 10^{-4}$
$8.0 \cdot 10^{-3}$	$2 \cdot 10^{-3}$	$79.86 \cdot 10^{-3}$	$2.0035 \cdot 10^{-4}$

3.5.2 Calibration curve for 2-10 mM 2HG in BRAINO

In the preparation of the 5 samples used in this experiment, the brain metabolite solution concentrations were kept constant, and the concentration of 2HG increased from 2 mM to 10 mM.

The brain metabolite solution was prepared as described in Chapter 3.2.2. The samples with increasing 2HG concentration were prepared according to Table 3.11. For the samples with 2 mM and 4 mM 2HG, volumetric flasks were used, and for the samples with 6 mM, 8 mM, and 10 mM 2HG fine pipetting was used to get the exact volume. To calculate the experimental mass, Equation 3.1 was used.

Table 3.11: Experimental data for the samples to the calibration curve of 2-10 mM 2HG in BRAINO

c_{2HG} [mol/L]	$m_{t(2HG)}$ [g]	$m_{r(2HG)}$ [g]	V_{BRAINO} [L]
$2.0 \cdot 10^{-3}$	0.019208	0.0185	$50.0 \cdot 10^{-3}$
$4.0 \cdot 10^{-3}$	0.019208	0.0194	$25.0 \cdot 10^{-3}$
$6.0 \cdot 10^{-3}$	0.0150	0.0149	$13.0 \cdot 10^{-3}$
$8.0 \cdot 10^{-3}$	0.0150	0.0150	$9.76156 \cdot 10^{-3}$
$10.0 \cdot 10^{-3}$	0.0150	0.0155	$7.80925 \cdot 10^{-3}$

3.6 Spectrum simulation

The 2HG NMR spectra were simulated using a Python script by Nils Åge Frøystein, seen in Appendix A, based on the python nmrsim library developed by Geoffrey M. Sametz [61]. The nmrsim library consists of tools to simulate NMR spectra from user-provided parameters, such as chemical shifts and J-coupling constants.

The nmrsim library was installed, and the packages numpy and matplotlib were imported. NumPy is a Python library that provides a multidimensional array object, and a collection of routines for fast operations on arrays, such as discrete Fourier transforms, basic linear algebra, basic statistical operations, and random simulations [48]. While Matplotlib is a library that creates visualizations in Python [29].

A function was created to convert chemical shifts from ppm to Hz given a spectrometer frequency in MHz, named ppm_to_hz. The input parameter $basic\_freq$, and a list ppm were established. Another function, two_hg, was created to return an array of the chemical shifts, v, from ppm_to_hz and a matrix, J, of the coupling constants.

Next, the *SpinSystem* class from the nmrsim library was imported. The *SpinSystem* class simulates a set of coupled nuclei [61]. The output of the two_hg function was used with the *SpinSystem* class to generate a peak list using the *peaklist* class, which makes a list of peaks [61]. The peak list was set to second order, and the matplotlib function was imported from $nmrsim.plt$. The peak system was then plotted using this function.

To simulate the NMR spectra at different field strengths, the same standard code was used, as shown in Appendix A. To change the field strengths, the $basic\_freq$ parameter can be adjusted to the desired magnetic field in MHz. The J-coupling constants used in this simulation were simulated and refined using the built-in simulation tool, Daisy, in TopSpin 4.3.0. The initial values for tweaking were based on the coupling constants in Table 1.3 taken from Bal et al. [6].

3.7 3D-Printed phantom

In 1984, Charles Hull patented an ”Apparatus for production of three-dimensional objects by stereolithography,” which is considered the world’s first 3D printer [28]. Since then, developers have significantly improved this technology. One of the first doctors to use 3D printing for reconstructing human parts was Dr. Atala, who developed machines to build customized scaffolds of human organs [69]. Today, 3D printing is a widely used method in healthcare. Surgeons and doctors utilize 3D scans to reconstruct patients’ internal structures before surgeries [69], and it is also used to construct objects with varying parameters.

In this thesis, a 3D-printed phantom was developed to achieve high-quality phantom data at the 3 T GE scanner at HUS. The goal was to create a phantom that could provide good shimming while holding smaller concentrations of metabolites. The idea of a 3D-printed phantom was inspired by the study by Bertolino et al. [8], as shown in Figure 1.6. It was further developed through discussions within the research group, and different approaches were tested.

For the smaller compartments, ping pong balls were considered early on due to their favorable geometric structure, which leads to optimal shimming conditions. A 3D-printed cube with a filling tube was also tested, but it was excluded because of its geometrical structure and filling mechanism. Figure 3.3 depicts the drawing of the cube and ping-pong ball.

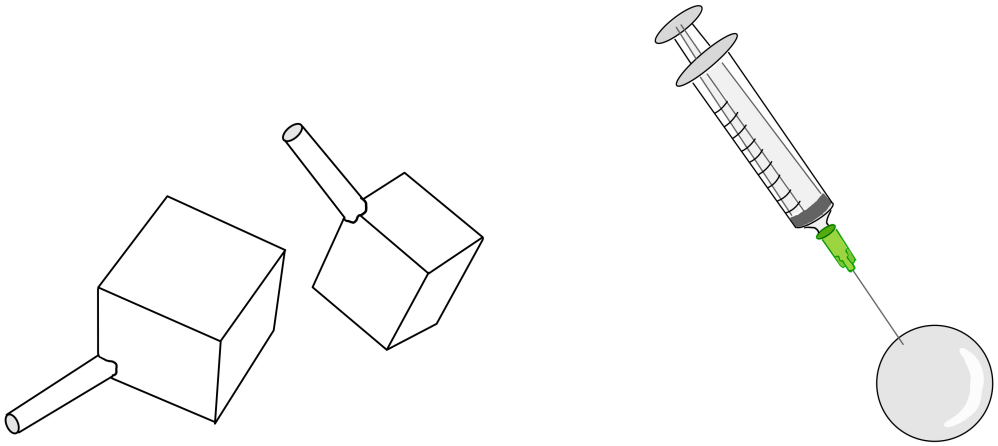

(a) (b)

Figure 3.3: A tested idea for a small compartment: a 3D-printed cube with a filling tube (a). The end result of a small compartment: a ping pong ball filled with a syringe (b).

To fill the ping pong balls, a syringe was used. To close the small holes made by the syringe, various methods were tested, including Parafilm, Loctite, and electrical tape. These methods were tested with a mixture of 10 M sugar inside the ping pong ball and water outside. The solutions were evaluated after a week. Additionally, the purity and residue from the ping pong ball and tape when kept in the buffer solution for a week were also tested.

The idea for the locking mechanism of the smaller compartments started with a boccia set, Figure 3.4, and evolved into a grip mechanism, Figure 3.5. The boccia set idea was tested using ping pong balls in a bucket of water, as shown in Figure 3.4a and 3.4b. This idea was excluded due to the complexity of the opening and screwing mechanisms required in the middle of the phantom and the amount of material needed inside the sphere Figure 3.4c. Ultimately, the mechanism to keep the ping pong balls in the middle of the sphere ended up being a grip

(a) (b) (c)

Figure 3.4: The first idea for the phantom: ping pong balls inside a boccia set (a), the boccia set in a bucket to see the stability of the ping pong (b), a 2D drawing of the first idea (c).

mechanism resembling the holding mechanisms of a diamond in rings, as shown in the drawing in Figure 3.5.

To fill the top of the sphere with solutions, the lid features a mechanism similar to a Peripheral Intravenous Catheter. The lid was screwed onto the phantom with a silicone seal inside the screwing mechanism. To ensure the lid was properly sealed, the silicone seal was smeared with grease.

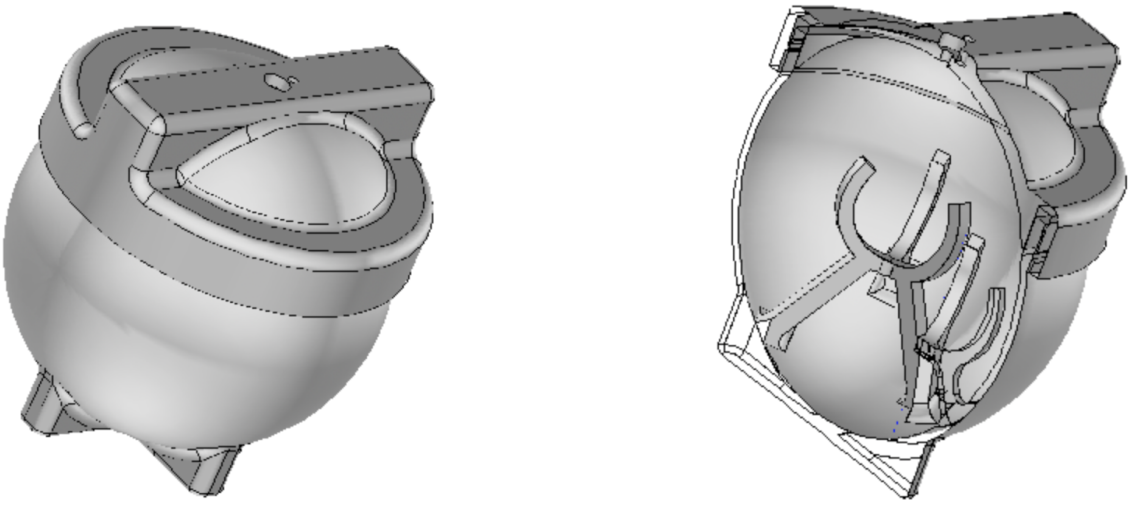

(a) (b)

Figure 3.5: Phantom-drawing by Morten Kristoffersen at the Medical Technology department at HUS: with the lid (a) and a cross-section of the drawing (b).

The complete phantom drawing that was sent to the 3D-printer was drawn in Autodesk Inventor Professional by Morten Kristoffersen at the Medical Technology Department at HUS. The drawing is displayed in Figure 3.5.

The phantom was printed with Clear resin V5 [20] using a Form 3+ 3D printer from Formlabs [21] and then post-processed with the Form Wash and Form Cure, also from Formlabs, as shown in Figure 3.6. This process was carried out by Morten Kristoffersen and Rolf Arne Haakonsen at the Medical Technology department at HUS.

Figure 3.6: Picture of the Form 3+ 3D-printer with the printed phantom, the Form Wash [21] and Form Cure [21].

Three different phantom compositions were created using the 3D-printed phantom and scanned on the 3 T GE scanner at HUS. The samples used were sample numbers 24, 25-27, 30-32, and 34-36 from Table 3.3. Sample number 24, a brain metabolite solution, was used as the surrounding solution in all the phantoms. The smaller compartments contained different concentrations of 2HG, NAA, Glu, and BRAINO. In phantom 3, a contrast agent was added to all the solutions. The details of the solutions in all the phantoms are explained in Table 3.12.

Table 3.12: Overview of the metabolite compositions in the phantoms

Compartment/Phantom	1	2	3
Main	BRAINO	BRAINO	BRAINO, 0.5 mM Clariscan
1	2 mM 2HG	12.5 mM NAA, 12.5 mM Glu	4 mM 2HG, 0.5 mM Clariscan
2	4 mM 2HG	12.5 mM NAA, 12.5 mM Glu, 4 mM 2HG	12.5 mM NAA, 12.5 mM Glu, 4 mM 2HG, 0.5 mM Clariscan
3	8 mM 2HG	4 mM 2HG, BRAINO	4 mM 2HG, BRAINO, 0.5 mM Clariscan

3.8 Observation on the LGG study at HUS

Some of the different detection methods of 2HG have already been implemented in an ongoing quality and control study with cancer patients at HUS. The pulse sequences that are already implemented are among others used to detect lactate and GABA. The four MRS pulse sequences already implemented are given in Table 3.13.

Table 3.13: Already implemented MRS pulse sequences in a quality and control study with cancer patients at HUS.

Pulse sequence:	PRESS	asymmetric PRESS	sLaser	sLaser
TE [ms]:	35	97	110	144

Chapter 4

Results and Discussion

This chapter presents the results from the experiments described in Chapter 3, along with a discussion of these findings.

First, a simple 1D spectrum of 2HG will be shown, accompanied by a 2D COSY spectrum to illustrate the chemical structure of 2HG. Following this, the simulated spectra from the spectrum simulation will be presented, along with the chemical shifts and coupling constants of 2HG.

Next, the experimentally determined optimal TE-times for 2HG at 4.0 ppm and 2.26 ppm in a spin echo sequence will be displayed. These results will be illustrated in a plot of 2HG's SI against the given TE-times at both 60 MHz and 600 MHz, along with a plot showing the behavior of the overlapping metabolite Glu at the same TE-times at 60 MHz.

The calibration curves for 2-10 mM pure 2HG and 2-10 mM 2HG in a brain metabolites solution will be presented, including a plot of the SI of edited 2HG at the given TE times.

Additionally, a picture of the 3D-printed phantom and some of the spectra and quantification from data acquired at the 3 T GE scanner at HUS will be shown. Finally, an *in vivo* spectrum from a tumor will be displayed.

4.1 Spectrum

In this section, a spectrum without any modulation will be presented along with a COSY spectrum to explain the chemical structure of 2-hydroxyglutarate. The Python-simulated spectra in the different field strengths will also be presented.

4.1.1 1D- and COSY-spectrum

The spectrum displayed in Figure 4.1, is a simple 1D-spectrum of 2HG at 600 MHz without any modulation. The pulse sequence for this type of spectrum consists of the excitation, a 90° pulse, followed by the spectrum acquisition.

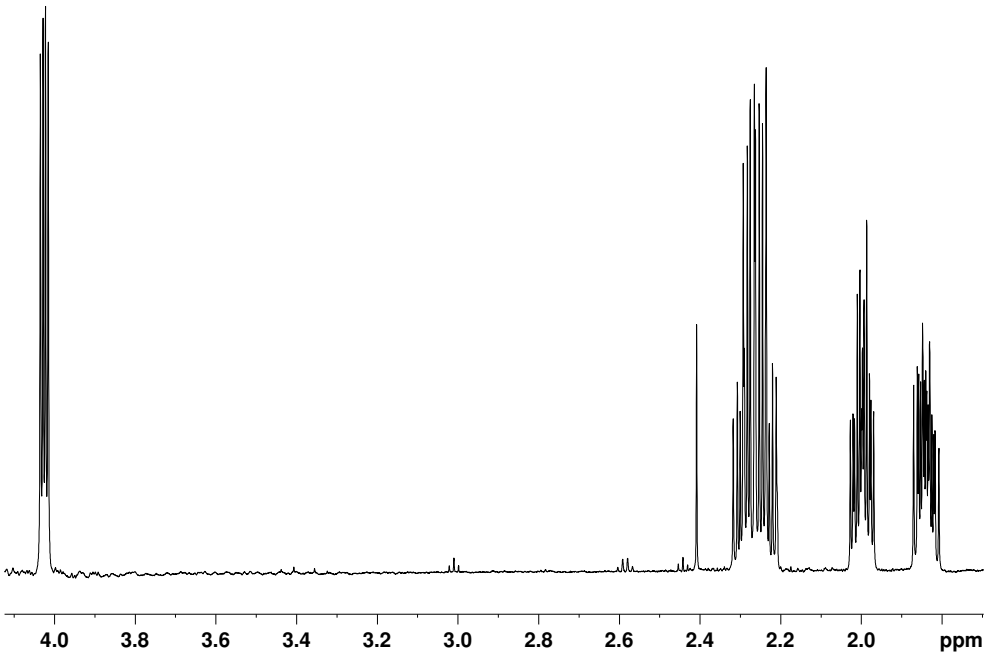

Figure 4.1: 1D-spectrum of 2HG at 600 MHz without any modulation.

The singlet at 2.4 ppm is a pollution in the sample of 2HG from the distributor Sigma-Aldrich. The buffer solution where tested by itself, and it had no visible disturbances.

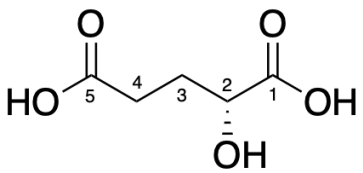

Figure 4.2: The chemical structure of 2HG with assignments [14].

Figure 4.3 is a combination of 2 COSY-spectra. The blue spectrum consists of a BRAINO solution with 5 mM 2HG, and the red spectrum is a COSY spectrum with pure 2HG. Based on Figure 4.1 and 4.3 can the structure and connections of 2HG be determined. Figure 4.2 displays the chemical structure of 2HG with the assigned placements.

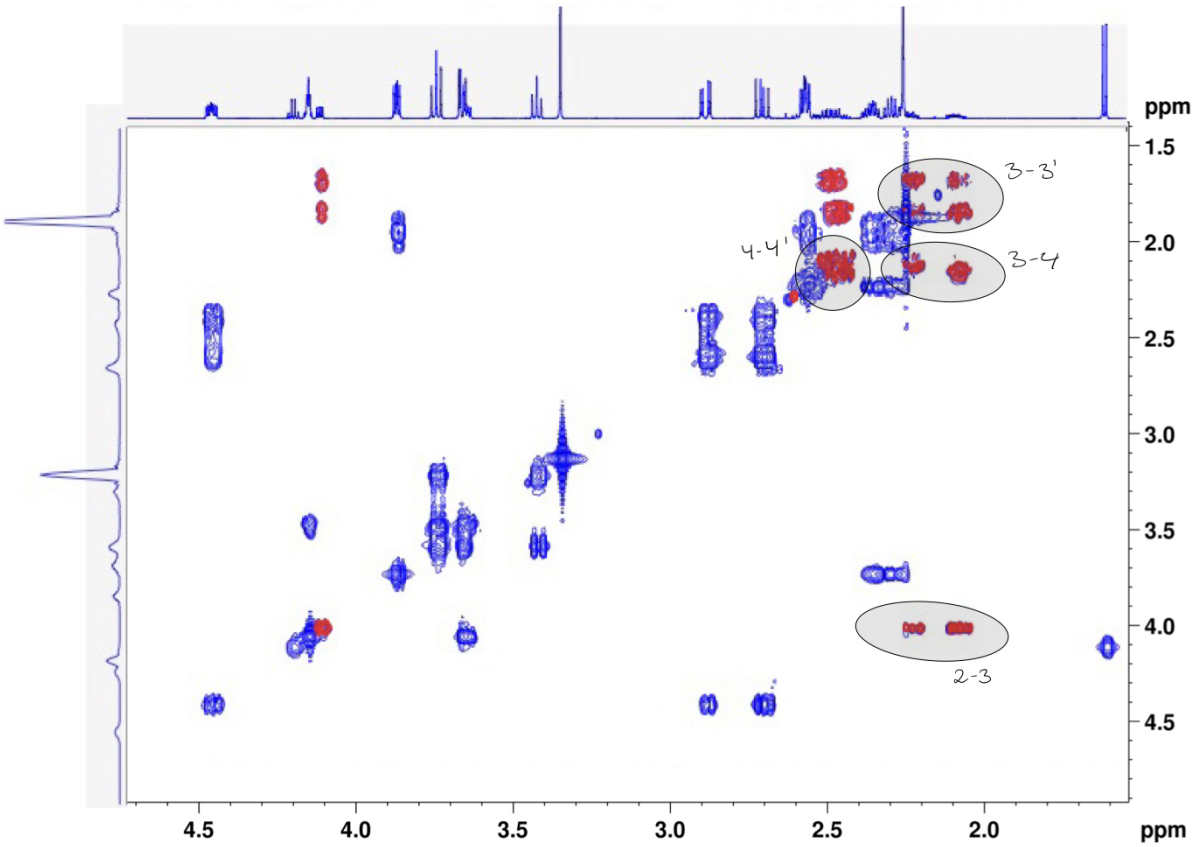

Figure 4.3: A COSY-spectrum of BRAINO with 5 mM 2HG (blue) and a COSY-spectrum of pure 2HG (red).

Based on Figure 4.3, we can observe the following coupling patterns for 2HG: The signal at 1.84 ppm, assigned as 3, couples with signals at 2.00 ppm, 2.24 ppm, 2.29 ppm, and 4.02 ppm, respectively assigned as 3´, 4, 4´, and 2. Another signal at 2.00 ppm, assigned as 3´, couples with the signals at 1.84 ppm, 2.24 ppm, 2.29 ppm, and 4.02 ppm, respectively assigned as 3, 4, 4´, and 2. The signal at 2.24 ppm, assigned as 4, couples with the signals at 2.00 ppm and 1.84 ppm, assigned as 3´ and 3 respectively, and with another signal at 2.29 ppm, assigned as 4´. Similarly, the signal at 2.29 ppm, assigned as 4´, couples with the signals at 2.00 ppm and 1.84 ppm, assigned as 3´ and 3. Lastly, the signal at 4.02 ppm couples with the signals at 2.00 ppm and 1.84 ppm, assigned as 3´ and 3. The peak assignment of 2HG, determined from Figure 4.3, is provided in Table 4.1, showing values similar to those given in Table 1.3 from Bal et al. [6].

Table 4.1: 2HG peak assignment with chemical shift (ppm) given from the spectrum in Figure 4.3 and 4.1.

Assignment	Chemical shift [ppm]
$^{1}COOH$	-
$^{2}CH(OH)$	4.02
$^{3}CH_2$	2.00 (3´), 1.84 (3)
$^{4}CH_2$	2.29 (4´), 2.24 (4)
$^{5}COOH$	-

4.1.2 Simulated spectra

For the Python simulation of the 1D 2HG spectrum at different field strengths, the chemical shift values acquired from the COSY spectra were used as starting values in the Daisy simulation, along with the values from Bal et al. [6], as shown in Table 1.3. The chemical shift values and coupling constants obtained from the Daisy simulation, based on Frøystein's work, were then used in the Python simulation. These values are displayed in Table 4.2.

Table 4.2: Chemical shifts, δ, and coupling constants, J, for 2HG acquired from the Daisy-simulation.

Parameter	position	2HG [pH 7.0]
δ [ppm]	2	3.9275
	3	1.7478
	3´	1.9036
	4	2.1448
	4´	2.1939
J [Hz]	2, 3	7.6505
	2, 3´	4.0492
	2, 4	0.0
	2, 4´	0.0
	3, 3´	-14.01
	3, 4	5.2552
	3, 4´	10.6635
	3´, 4	10.8554
	3´, 4´	5.8262
	4, 4´	-14.95

The Python simulation was conducted to observe how the 1D spectrum for 2HG would vary at different field strengths and to assess the impact of these variations. To acquire the spectra for 2HG, the simulation utilized the density operator method explained in Chapter 2.3.3.

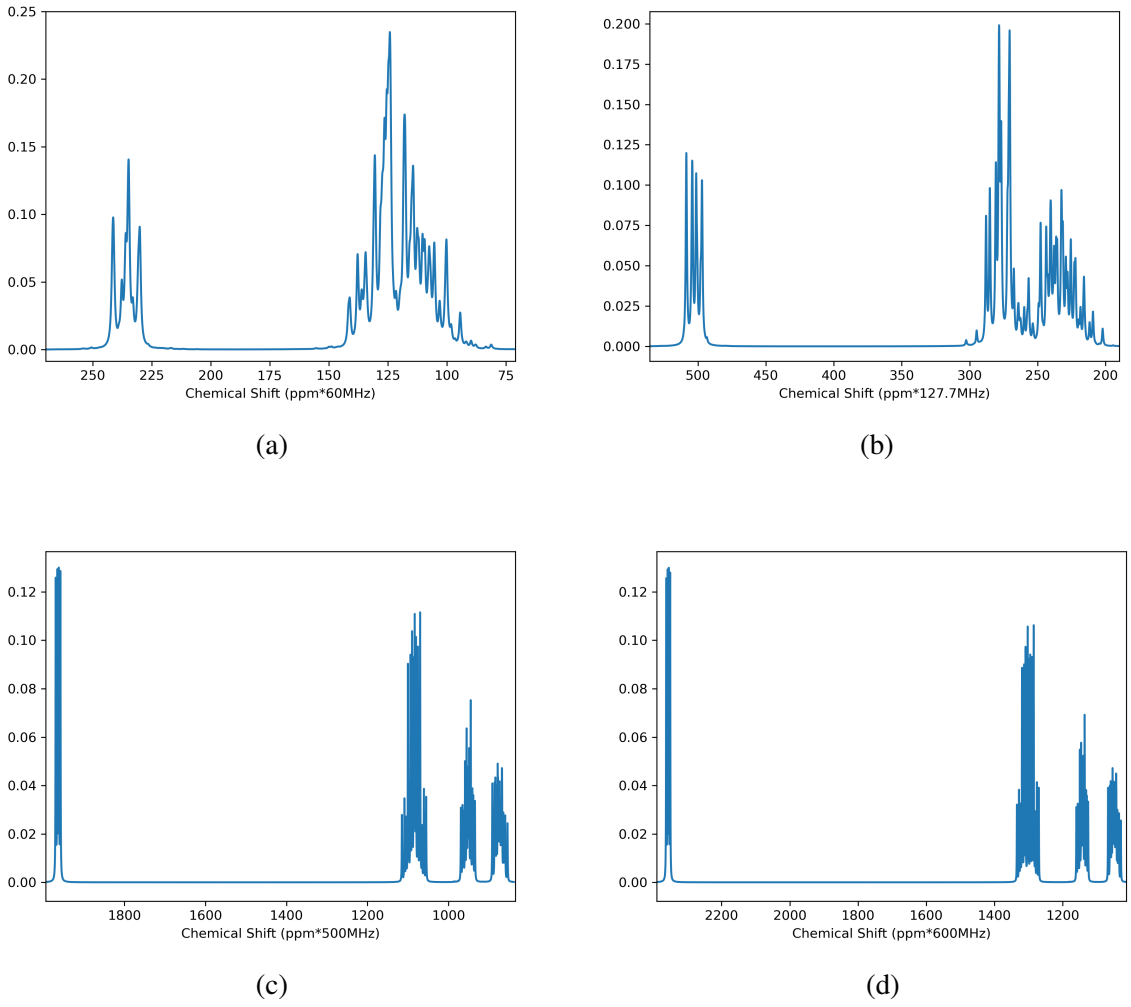

Figure 4.4: Python-simulated 1D 2HG-spectrum at: 60 MHz (a), 3 T (b), 500 MHz (c), 600 MHz (d) (The x-axis in the figures are the chemical shift values in ppm * field strengths).

Figure 4.4 displays the simulated 1D 2HG spectra at 60 MHz (a), 3 T (b), 500 MHz (c), and 600 MHz (d). The spectra, simulated with the Python package ”nmrsim”, are free from noise, resulting in a better signal-to-noise ratio compared to the experimental data.

To simulate the spectrum for the field strength 3 T, the strength was calculated from T to MHz with Equation 2.8 presented in Chapter 2.1.2. Here B_0 = 3 T and $\frac{\gamma}{2\pi}$ for ^1H is $42,577\ \frac{MHz}{T}$ [55].

$$\frac{\gamma}{2\pi}\vec{B}_0 = 42.577\frac{MHz}{T}\cdot 3T = 127.731MHz \tag{4.1}$$

The difference between the 500 MHz and 600 MHz spectra in Figure 4.4 is not as apparent as it is in the experimental data. However, when focusing on the peaks at the respective δ values in the simulated spectra, the peak splitting becomes more evident, making the differences between the 500 MHz and 600 MHz 1D spectra more visible, as shown in Figure 4.5. Since the Python package ”nmrsim” does not incorporate noise, the signal-to-noise ratio in the simulated spectra is unrealistically high compared to the experimental data. This affects the visibility of the spectrum differences between the 500 MHz and 600 MHz field strengths, making them less noticeable in the simulated spectra than in the NMR spectra.

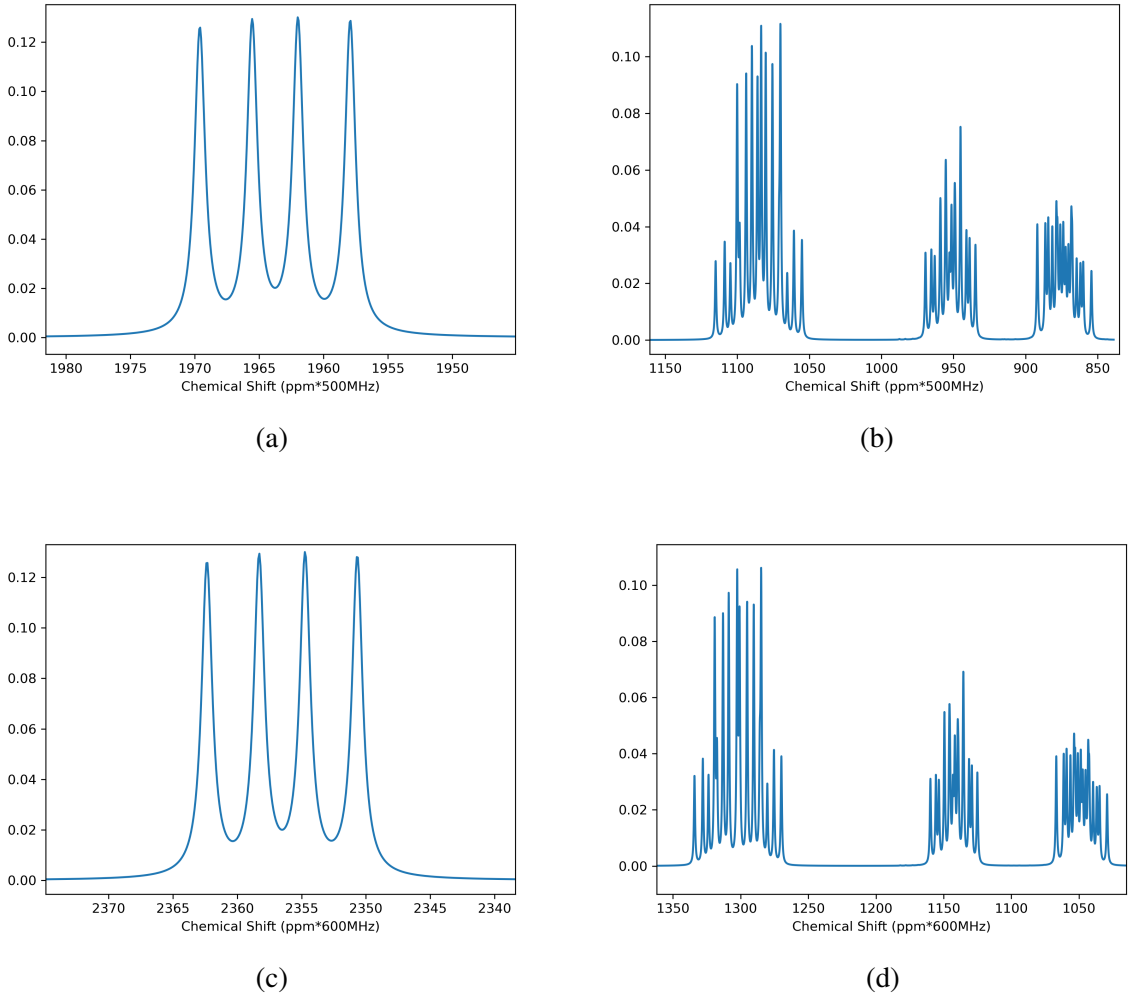

Figure 4.5: Python-simulated 1D 2HG-spectrum at 500 MHz around 4 ppm (a), and around 2 ppm (b), and the Python-simulated 1D 2HG-spectrum at 600 MHz around 4 ppm (c), and around 2 ppm (d) (The x-axis values in the figures are the chemical shift values in ppm * field strengths).

To see how accurately represented the simulated spectra were, the simulated spectrum at 600 MHz was visually compared with the experimental 600 MHz spectrum, Figure 4.6. Based on Figure 4.6, the simulated spectrum of 2HG at 600 MHz can be compared with the experimental spectrum of 2HG at 600 MHz. Figure 4.6a and Figure 4.6c display the spectra around 4 ppm, while Figure 4.6b and Figure 4.6d show the spectra around 2 ppm. As observed in Figure 4.6, the peak splitting and the J-coupling in the simulated spectra around these two chemical shifts, 4 ppm, and 2 ppm, are quite accurately represented compared to the experimental spectra.

The simulated spectra helped visualize how different field strengths would affect the 2HG signals before obtaining the experimental data. Based on the 1D spectrum at 600 MHz and the simulated spectra for 2HG at 500 MHz and 600 MHz, the J-coupling at 4.02 ppm was examined further. To the naked eye, the peaks around 4 ppm could appear as a doublet of doublets in the first order, while the other peaks were determined to be of higher order based on their peak splitting and SI. As explained in Chapter 2.3.2, investigating the coupling mechanism of higher-order coupled spins requires the use of the density operator, as shown in Equation 2.35.

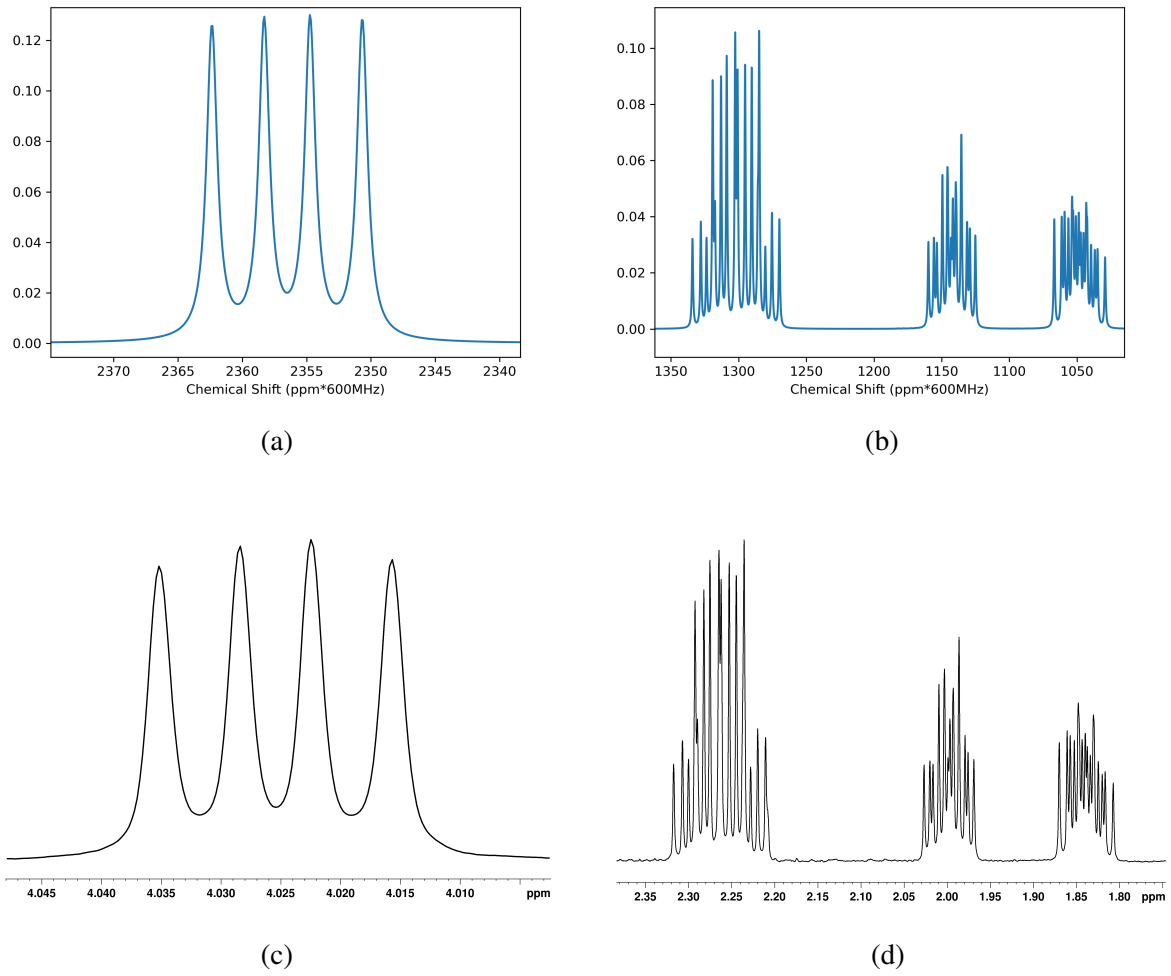

Figure 4.6: 1D 2HG spectra at 600 MHz: simulated around 4 ppm (a), simulated around 2 ppm (b), experimental around 4 ppm (c) and experimental around 2 ppm (d).

The coupling mechanism of the peaks at 4.02 ppm was investigated using Equation 2.34 from the vector model. The desired phase angle for the peaks at 4.02 ppm is 2π, as these peaks are observed with editing using the MEGA-PRESS sequence. Equation 2.34 was used to determine the theoretical optimal TE for a MEGA-PRESS sequence observing the 4.02 ppm peaks for 2HG, assuming the peaks are of first order. In this context, θ represents the angle between the two vectors, so for the signal at 4.02 ppm, the desired phase change is 360°, 2π, and t represents the TE for this MEGA-PRESS sequence. For the coupling constant J at 7.65 Hz, the theoretical TE, assuming a first-order coupling, should be:

$$\theta = 2\pi J \cdot t = 2\pi J \cdot TE \tag{4.2}$$

$$TE = \frac{\theta}{2\pi J} = \frac{2\pi}{2\pi J} = \frac{1}{J} = \frac{1}{7.65 s^{-1}} = 132 ms \tag{4.3}$$

For the coupling constant J at 4.05 Hz, the theoretical TE, assuming a first-order coupling, should be,

$$TE = \frac{\theta}{2\pi J} = \frac{2\pi}{2\pi J} = \frac{1}{J} = \frac{1}{4.05 s^{-1}} = 247 ms \tag{4.4}$$

If peak 2, at 4.02 ppm, is of first-order, the theoretical optimal TE for a peak 180° out of phase should be 132 ms and 247 ms. In the next sub-chapter, ”Optimal TE”, the experimental optimal TE values are presented and compared with these theoretical values.

The basis sets used for the modulation and quantification in Osprey was also simulated using the density operator, as described in Equation 2.35. Figure 4.7 displays the basis sets for 2HG at TE values of 30 ms, 80 ms, 110 ms, and 130 ms. These basis sets were obtained from MRICloud [42] and computed for a sLaser pulse sequence at a 3 T GE scanner.

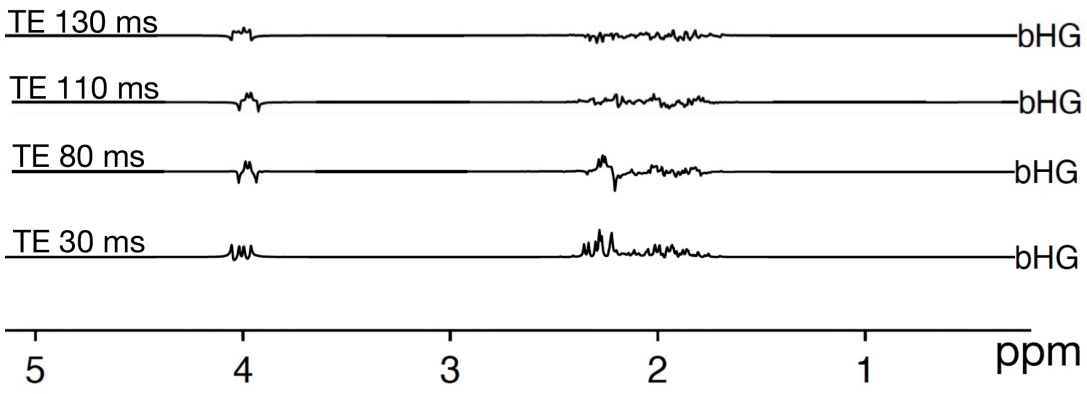

Figure 4.7: The basis sets of 2HG from MRICloud [42] for a sLaser sequence with TE = 30 ms, 80 ms, 110 ms, and 130 ms.

From Figure 4.7, it can be observed that the splitting pattern at the lower chemical shift is of higher order. Compared to the Python-simulated spectrum at 3 T, 127.7 MHz, the peak-splitting around 2 ppm in the basis set appears more pronounced than in the Python-simulated spectrum, Figure 4.4b. When focusing on the peak around 4 ppm, the basis set shows that the peaks seem nearly refocused and not 180° out of phase around TE = 130 ms. This suggests that the peaks around 4 ppm may be of higher order at a lower magnetic field.

4.2 Optimal TE-time

In this section, the experimental optimal TE-time in a spin echo sequence for 2HG at 4.02 ppm and 2.26 ppm will be presented. This includes a plot of 2HG´s SI with the given TE-time at 60 MHz and 600 MHz, as well as a plot of the overlapping metabolite Glu's behavior at the same TE times at 60 MHz. Additionally, the spectra with the optimal TE-time for the different peaks will be displayed. The data used for the plots in this section can be found in Appendix C.1 and C.2.

The spin echo sequence performed on the NMR machines, 60 MHz Nanalysis and 600 MHz Bruker BioSpin, can be compared to the data from a sLaser sequence on the 3 T GE scanner. In the 60 MHz Nanalysis and 600 MHz Bruker BioSpin, the entire sample is analyzed, and due to the small sample size, it is assumed that the entire sample experiences the same effects. In a sLaser sequence, adiabatic pulses are used, as explained in Chapter 2.3.7. When adiabatic pulses are applied, all the spins in a sample experience the same effects [23, 1, 2].

4.2.1 4.02 ppm

The signal from 2HG at 4.02 ppm, assigned to position 2 displayed in Figure 4.2, is used in regard to editing pulse sequences, here MEGA-PRESS.

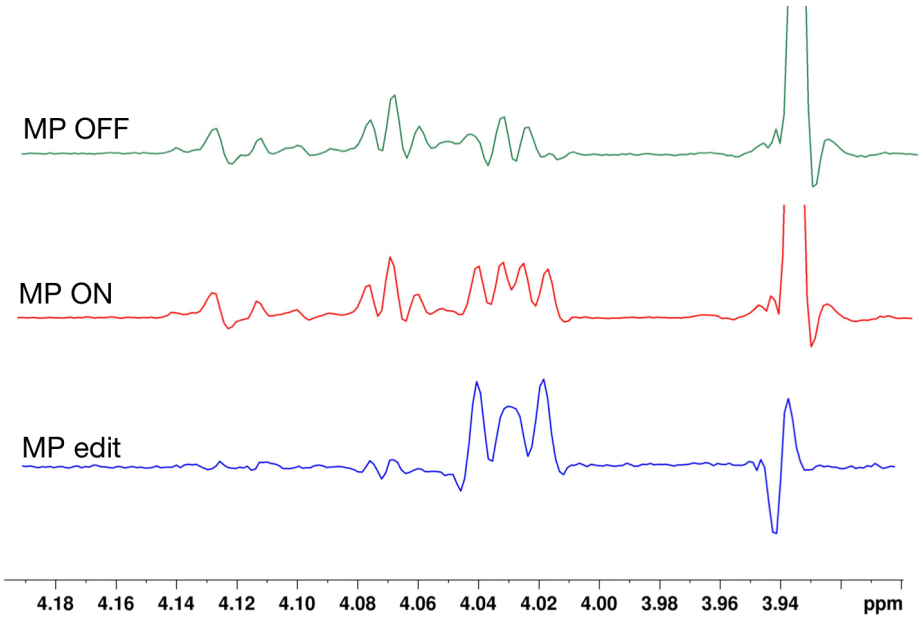

Figure 4.8: The OFF, ON, and edited spectrum from the MEGA-PRESS sequence with TE = 80 ms at 500 MHz of a brain metabolite solution with 10 mM 2HG focused around 4 ppm.

When an editing sequence is used on 2HG, an editing pulse is applied around peak 3 at 1.9 ppm during the ON part of the sequence, resulting in a refocusing of the signal at 4.02 ppm. This occurs due to the coupling between the peak assignments 2 and 3, as explained in the previous chapter. The signal in the OFF sequence is subtracted from the signals in the ON sequence, producing the edited spectrum. To achieve the highest SI in the edited spectra, the signals in the OFF spectra should be as negative as possible.

The goal of edited spectra is to reduce the signals from other metabolites present in the voxel, making it easier to measure 2HG. In the MEGA-PRESS figure in Appendix D.1, it is shown how the signals from other metabolites in a brain metabolite solution are reduced when the OFF spectrum is subtracted from the ON spectrum, resulting in an easier visualization of the 2HG signals around 4 ppm, as displayed in Figure 4.8 where the signals around 4 ppm are in focus.

To determine the optimal TE for editing sequences on 2HG, 20 spectra were accumulated using a spin echo sequence with a TE range from 10 ms to 200 ms at 60 MHz and 600 MHz. The respective SI at 4.02 ppm was measured and plotted against the respective TE in Figure 4.9.

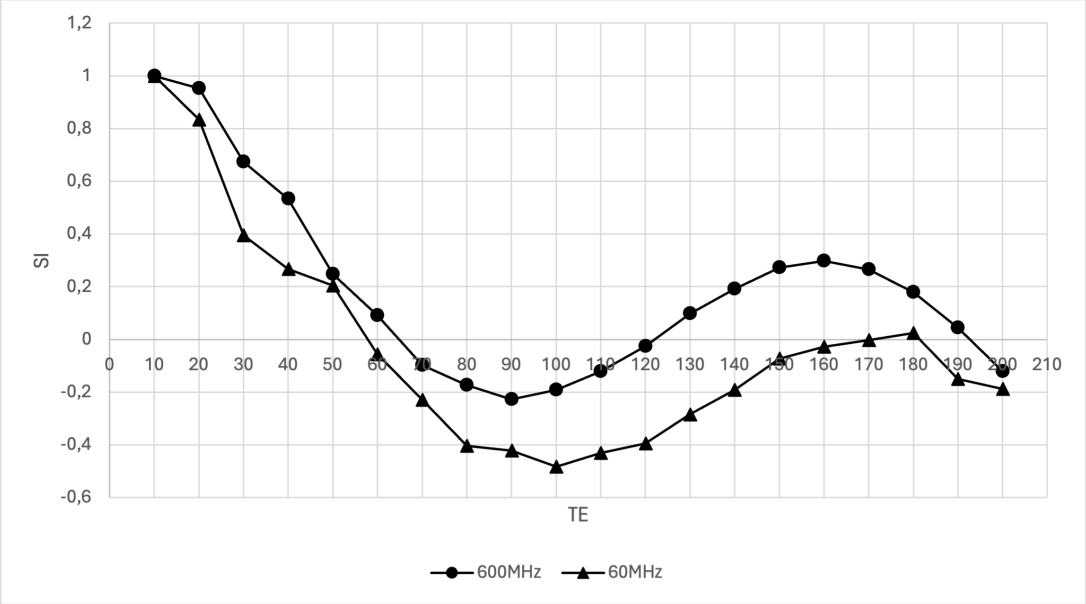

Figure 4.9: The SI of 2HG at 4.02 ppm plotted against the TE-time at 60 MHz (△) and 600 MHz (○).

As depicted in Figure 4.9, the minimum SI for peak 2 at 4.02 ppm occurs at TE = 90 ms for 600 MHz and TE = 100 ms for 60 MHz. Figure 4.10a shows the spectra accumulated at the TE values with the minimum SI at 600 MHz: 80 ms (blue), 85 ms (red), 90 ms (brown), 95 ms (green), and 100 ms (turquoise). Figure 4.10b displays the spectra accumulated at the TE values with the minimum SI at 60 MHz: 90 ms (blue), 100 ms (red), and 110 ms (green).

As seen in Figure 4.10a and 4.10b, the SI is difficult to distinguish visually. The peaks were integrated as explained in Chapter 3, and the integration values are plotted in Figure 4.9. Upon close inspection, the brown spectrum, TE = 90 ms, in Figure 4.10a appears to be the most negative within the depicted interval. Similarly, in Figure 4.10b, the red spectrum, TE = 100 ms, is the most negative within the given spectrum interval.

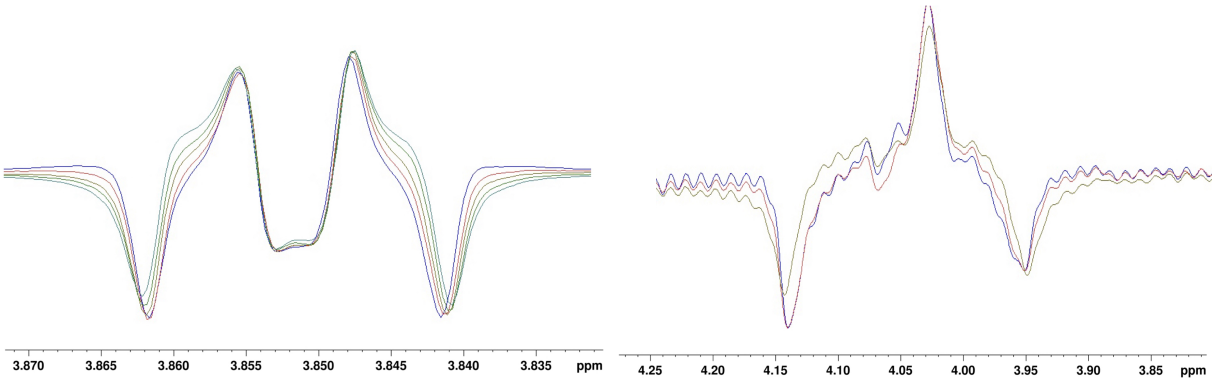

(a) (b)

Figure 4.10: The 2HG spectra at chemical shift 4.02 ppm around the optimal TE-times: at 600 MHz with TE = 80 ms (blue), 85 ms (red), 90 ms (brown), 95 ms (green) and 100 ms (turquoise) (a). And at 60 MHz with TE = 90 ms (blue), 100 ms (red), and 110 ms (green) (b).

From the calculations done in the previous chapter, the theoretical optimal TE time for the 4.02 ppm signal, if it were of first order, should have been 132 ms and 247 ms. However, the plot in Figure 4.9 shows that the signal at 4.02 ppm is most negative at TE = 90 ms or 100 ms, depending on the magnetic field strength. This, along with observations from the basis set of 2HG and the peak splitting, helped determine that, although the peaks appear as a doublet of doublets, other effects are present, indicating higher-order coupling. In the 1D spectrum of 2HG without any modulation, a roofing tendency is observed in the peaks at 4.02 ppm, which can also suggest higher-order coupling.

4.2.2 2.26ppm

The signal from 2HG at 2.26 ppm is used in unedited spectrum analysis. The peaks and signals at this chemical shift have a higher-order coupling pattern, as explained in the COSY spectrum. This signal originates from assignment 4. As the field strength decreases, the peak separation also decreases, making it harder to distinguish the peaks at 2.26 ppm and 1.8 ppm at lower magnetic field strengths.

In this section, the peak areas at 2.26 ppm will be presented. Since the signals in this area are analyzed using unedited pulse sequences, the desired SI is as high as possible. To determine the optimal TE, 20 spectra were accumulated over a TE range from 10 ms to 200 ms at 60 MHz and 600 MHz. The respective SIs at 2.26 ppm were measured and plotted against the TE times in Figure 4.11.

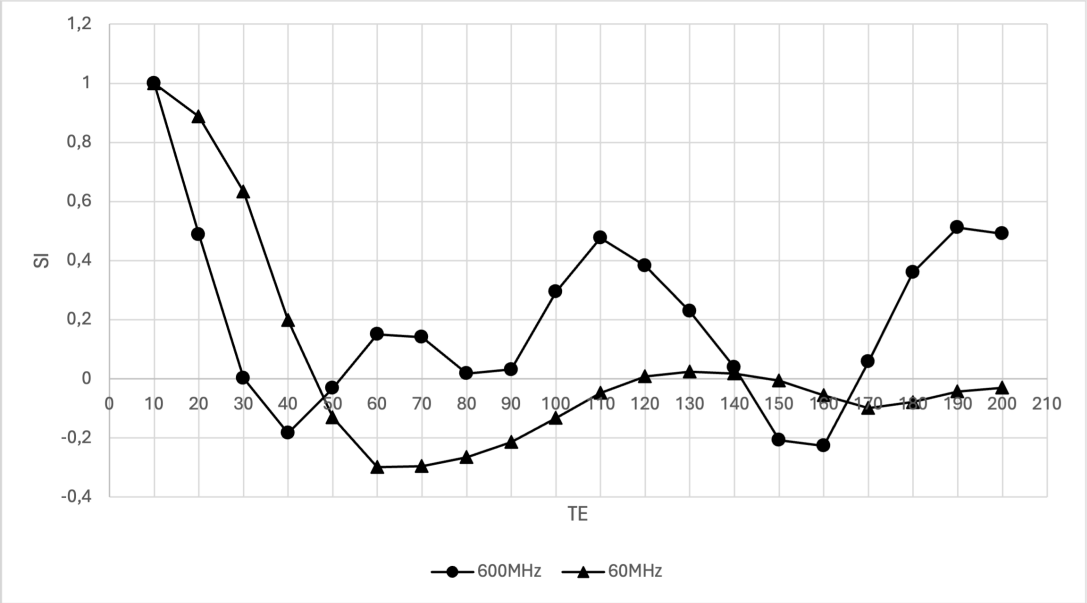

Figure 4.11: The SI of 2HG at 2.26 ppm plotted against the TE-time, at the field strengths 60 MHz (△) and 600 MHz (○).

As seen in Figure 4.11, the maximum signal for the peaks at 2.26 ppm occurs at TE = 130 ms for 60 MHz, while for 600 MHz, the highest SI is at TE = 110 ms and TE = 190 ms. The signals around 110 ms were chosen due to the potential loss of signal with longer TE and because TE = 110 ms was already implemented in ”The LGG” study at HUS.

The trends in the curves for the magnetic fields 60 MHz (△) and 600 MHz (○) in Figure 4.11 are similar, but the SI differences in the 60 MHz (△) curve are smaller than in the 600 MHz (○) curve. This could be due to the lower peak splitting at 60 MHz. As a result, the phase differences of the peaks are less pronounced, leading to smaller SI differences at various TE times.

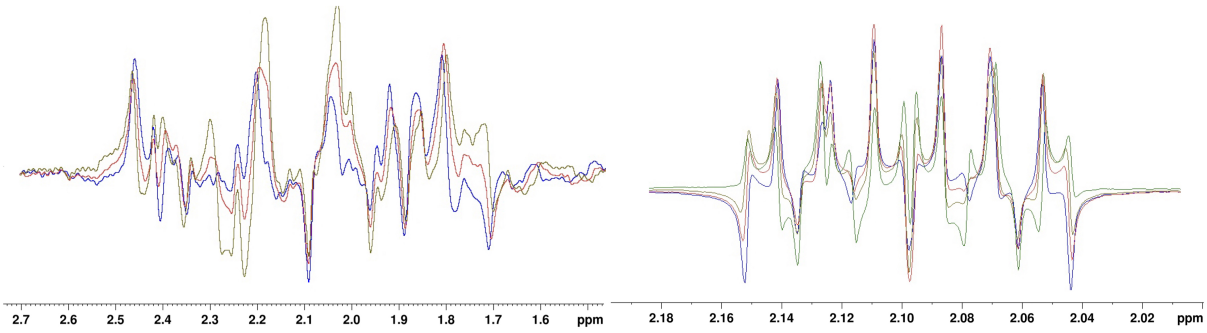

(a) (b)

Figure 4.12: The 2HG spectra at chemical shift 2.26 ppm around the optimal TE-times: at 60 MHz with TE = 120 ms (blue), 130 ms (red), and 140 ms (brown) (a). And at 600 MHz with TE = 100 ms (blue), 105 ms (red), 110 ms (brown), and 120 ms (green) (b).

In Figure 4.12a, the spectra from the 60 MHz system with TE = 120 ms (blue), 130 ms (red), and 140 ms (brown) are displayed. As seen, the signal peaks at 2.26 ppm and 1.8 ppm are difficult to separate visually at a low magnetic field. Therefore, the signals were systematically integrated as explained earlier. Focusing on the interval, the red spectrum, TE = 130 ms, appears the most positive. Figure 4.12b displays the spectra from the 600 MHz system with TE = 100 ms (blue), 105 ms (red), 110 ms (brown), and 120 ms (green). The brown spectrum, TE = 110 ms, appears the most positive. Due to the difficulty in visually separating the spectra, the peaks were integrated, and the optimal TE times based on the SI were determined from this integration, plotted in Figure 4.11.

Based on these results, the optimal TE to detect the 2.26 ppm signal of 2HG with a spin echo sequence is 110 ms at 600 MHz and 130 ms at 60 MHz. The detection of 2HG at 110 ms using sLaser has, as mentioned, also been studied by Shams et al. [62] in 2021. They investigated the detection of 2HG with sLaser at a TE of 110 ms at 7 T both *in vitro* and *in vivo*. Their study compared a sLaser sequence with TE = 110 ms and a MEGA-sLaser sequence with TE = 74 ms, concluding that the sLaser sequence with TE = 110 ms was preferable due to its similar fit reliability, simpler implementation, and preservation of signals from other metabolites [62]. A sLaser sequence with TE = 110 ms is also already implemented in ”The LGG Study” at HUS. Based on this, the recommended TE in a sLaser sequence for detecting the 2HG signal at 2.26 ppm is 110 ms.

4.2.3 1.8 ppm

In this section, the signal from the peak areas at 1.8 ppm will be presented. Since the signals in this area are used in unedited spectra, the desired SI is as high as possible, similar to the signal at 2.26 ppm explained in the previous section. Figure 4.13 displays the SI of the 2HG signal around 1.8 ppm at different TE times in a spin echo sequence.

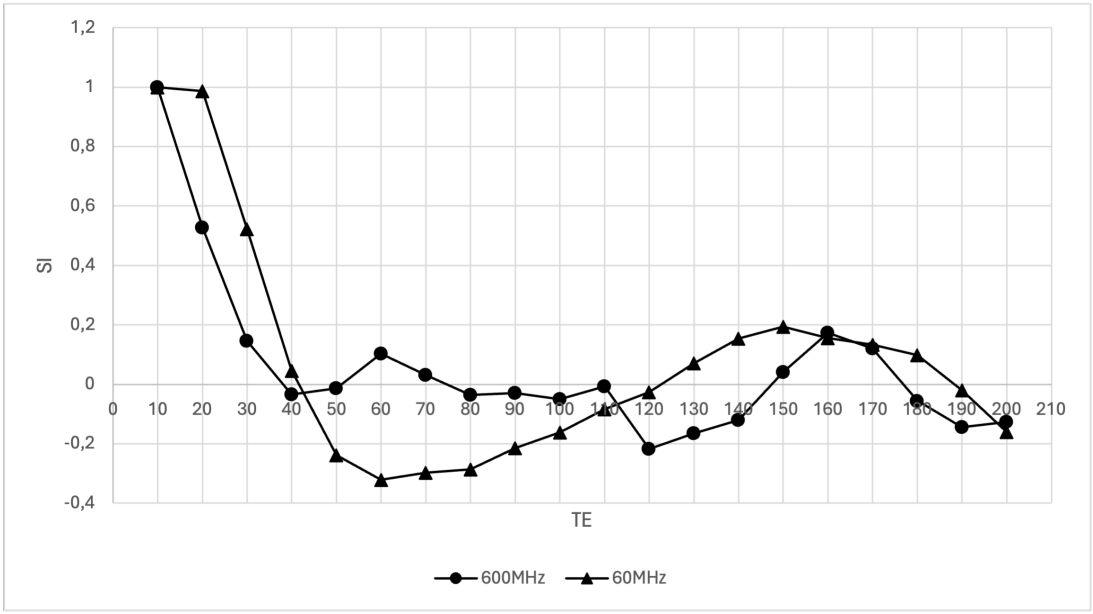

Figure 4.13: The SI of 2HG at 1.8 ppm plotted against the TE-times from a spin echo sequence at the field strengths: 60 MHz (△) and 600 MHz (○).

The peaks and signal at 1.8 ppm also have a higher-order coupling pattern, as explained in the COSY spectrum. These signals originate from peak assignment 3. To determine the optimal TE, 20 spectra were accumulated over a TE range from 10 ms to 200 ms at 60 MHz and 600 MHz, and the respective SIs at 1.8 ppm were measured and plotted against the TE times in Figure 4.13.

For the signal around 1.8 ppm, the two chemical shifts are well separated at a high magnetic field, 600 MHz, while at the lower field, 60 MHz, the shifts are not visually distinguishable from the signal peaks at 2.26 ppm. The signals at 1.8 ppm at 60 MHz were systematically integrated as explained in the methods section. At 600 MHz, the signal peaks at 1.8 ppm are well separated. Due to the poor separation at 60 MHz, the two signals at 1.8 ppm at 600 MHz were integrated together to compare them with the signals at 60 MHz. From Figure 4.13, the maximum SI for the two peaks around 1.8 ppm is at TE = 160 ms for 600 MHz and TE = 150 ms for 60 MHz.

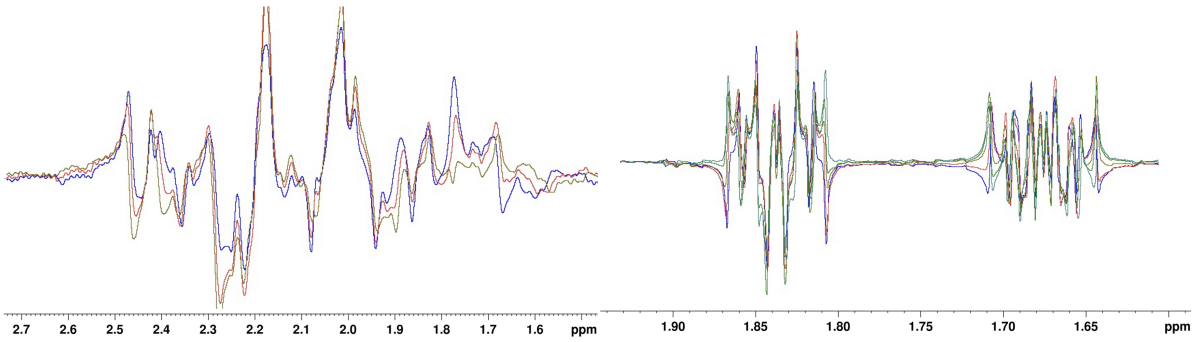

(a) (b)

Figure 4.14: The 2HG spectra at chemical shift 1.8 ppm around the optimal TE-times: at 60 MHz TE = 140 ms (blue), 150 ms (red) and 160 ms (brown) (a). And at 600 MHz TE = 150 ms (blue), 155 ms (red), 160 ms (brown), 165 ms (green) and 170 ms (turquoise) (b).

In Figure 4.14a, the spectra from the 60 MHz system with TE = 140 ms (blue), 150 ms (red), and 160 ms (brown) are displayed. As seen, the signal peaks at 1.8 ppm are difficult to visually separate from the signal peaks at 2.26 ppm, so the signals were systematically integrated as explained. Focusing on the interval, the red spectrum, TE = 150 ms, appears the most positive. In Figure 4.14b, the spectra from the 600 MHz system with TE = 150 ms (blue), 155 ms (red), 160 ms (brown), 165 ms (green), and 170 ms (turquoise) are displayed. The brown spectrum, TE = 160 ms, appears the most positive. The separation of the spectra and identifying which has the highest SI is difficult to see visually, so the peaks SI were integrated and plotted in Figure 4.13.

The signal at 1.8 ppm is often seen in connection with the signals at 2.26 ppm and is rarely studied by itself. For the spectra obtained *in vivo*, both the signals at 2.26 ppm and 1.8 ppm overlap with Glu, NAA, and GABA. Therefore, Glu and NAA were studied together with 2HG at 3 T, and the behavior of the Glu signal at different TE times was studied at 60 MHz.

4.2.4 Overlapping metabolites

In addition to the difficulty in separating its own signal, other brain metabolites also have signals in the same area as 2HG. As shown in Table 1.2, Glu and NAA particularly overlap with the signals from 2HG around 2.26 ppm and 1.8 ppm. To detect the signal from 2HG in a brain metabolite solution and potentially *in vivo* in this area, a solution with pure Glu was analyzed at 60 MHz to determine the signal behavior in the given region.

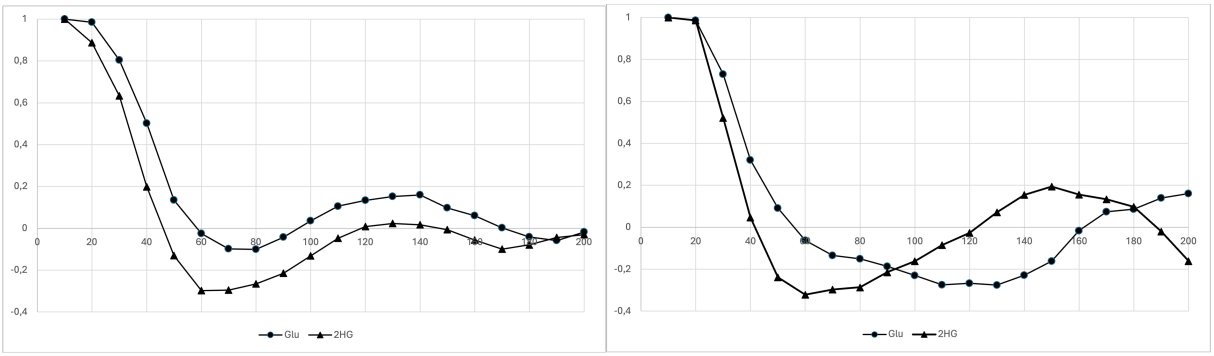

(a) (b)

Figure 4.15: The SI of Glu (○) and 2HG (△) at 60 MHz plotted against the different TE-times in a spin echo sequence around the chemical shifts: 2.3 ppm (a) and 2 ppm (b).

The SI of Glu and 2HG around 2.3 ppm and 2.0 ppm were integrated and plotted against the respective TE values, as shown in Figure 4.15. In Figure 4.15a, the trends on the plotted curves for 2HG and Glu are similar. The signal peaks were, therefore, further investigated at TE = 130 ms, the optimal TE at 60 MHz for the signal at 2.26 ppm for 2HG, to determine if the peak recognizer in the modulation programs could identify distinctive features to separate the peaks. Due to the low magnetic field and the higher-order coupling, the peaks are hard to visually separate. Figure 4.16 displays the signals from Glu (red spectrum) and 2HG (blue spectrum) from a spin echo sequence with TE = 130 ms in the interval from 1.5 ppm to 2.7 ppm.

Glu has a distinctive peak at 2.35 ppm that can be used to separate it from other metabolites. The peaks from 2.00 ppm and lower can be used for the detection of 2HG, as there is no signal from Glu in this region. However, NAA and GABA both have signals around the same chemical shift. In the modulation performed with Osprey and LCModel in Chapter 4.4 on the data accumulated at the 3 T GE scanner at HUS, the importance of these distinctive peaks will be evident.

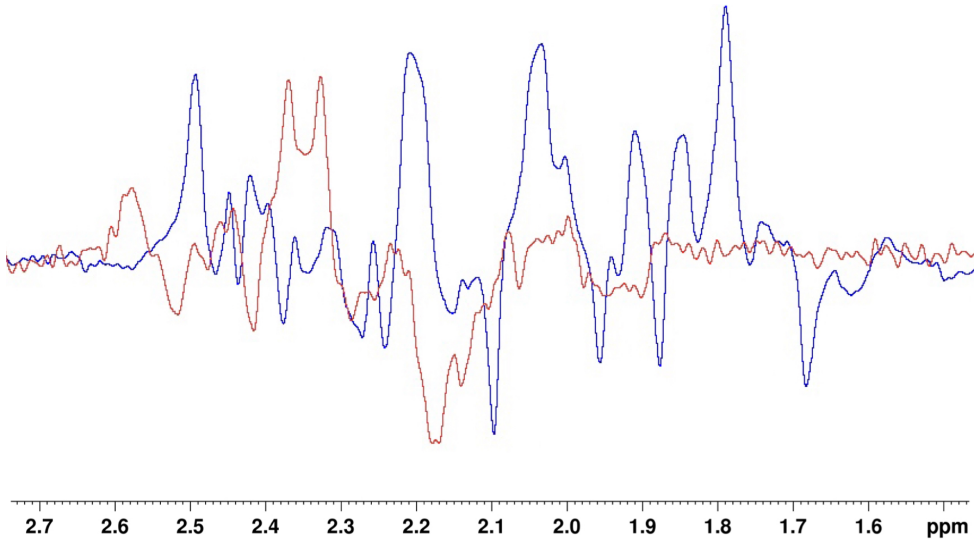

Figure 4.16: The signal-peaks for Glu (red) and 2HG (blue) from a spin echo sequence with TE = 130 ms focused on 1.5 ppm to 2.7 ppm at 60 MHz.

4.2.5 Optimal TE at 4.02 ppm, 2.26 ppm, and 1.8 ppm

Based on the results from the experiments already presented, the optimal TE at 4.02 ppm is 100 ms for 60 MHz and 90 ms for 600 MHz. For the signals around 2 ppm, the optimal TE is 130 ms for 60 MHz and 110 ms for 600 MHz. If the signal from 2HG at 1.8 ppm were to be investigated by itself, the optimal TE would be 150 ms at 60 MHz and 160 ms at 600 MHz. The optimal TE times for each peak assignment of 2HG are presented in Table 4.3.

Table 4.3: The optimal TE for the 2HG signals at 4.02 ppm, 2.26 ppm, and 1.8 ppm.

Peak assignment	Chemical shift [ppm]	TE = 60 MHz [ms]	TE = 600 MHz [ms]
2	4.02	100	90
3, 3´	1.84, 2.00	150	160
4, 4´	2.24, 2.29	130	110

The spectrum for the optimal TE for peak assignment 2 at 4.02 ppm, as determined from the analyses, is presented in Figure 4.17. The best spectrum at 60 MHz with TE = 100 ms is shown in Figure 4.17a, and the best spectrum at 600 MHz with TE = 90 ms is shown in Figure 4.17b.

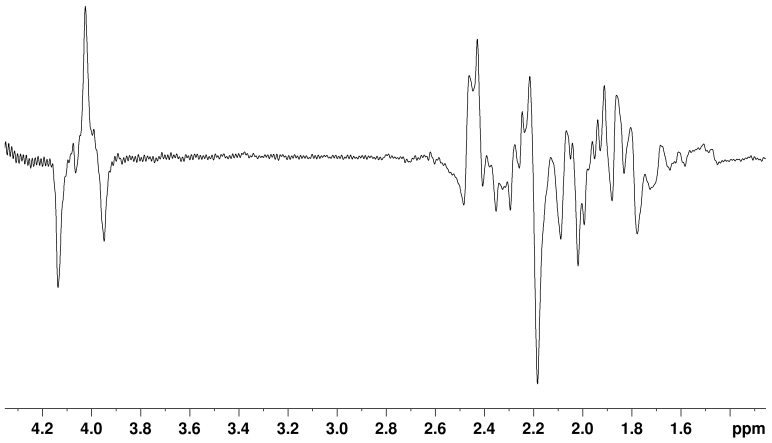

(a)

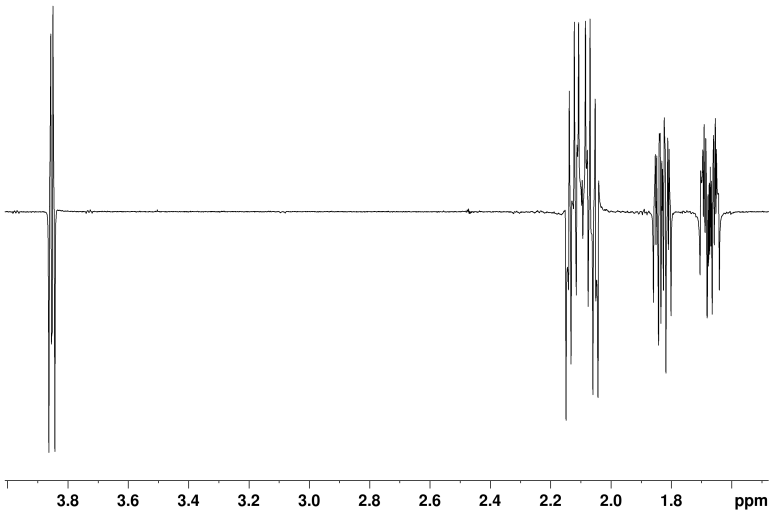

(b)

Figure 4.17: The experimental best 2HG spectra for the chemical shift 4.02 ppm at 60 MHz with TE = 100 ms (a) and 600 MHz with TE = 90 ms (b).

The spectrum for the optimal TE for peak 4 at the chemical shift of 2.26 ppm, as determined from the analyses, is presented in Figure 4.18. The best spectrum at 60 MHz with TE = 130 ms is shown in Figure 4.18a, and the best spectrum at 600 MHz with TE = 110 ms is shown in Figure 4.18b.

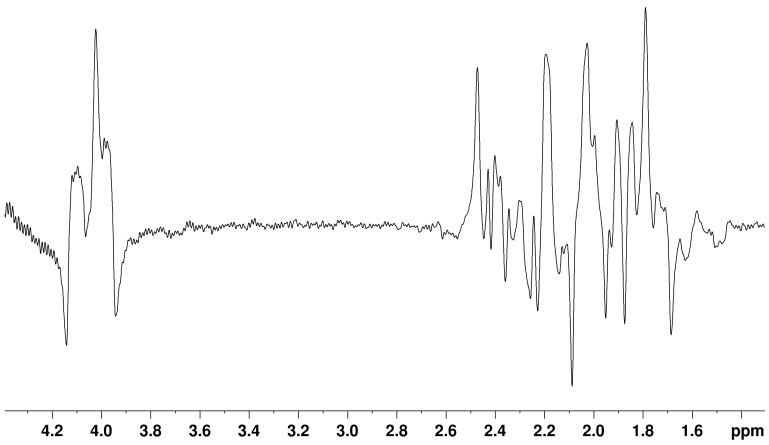

(a)

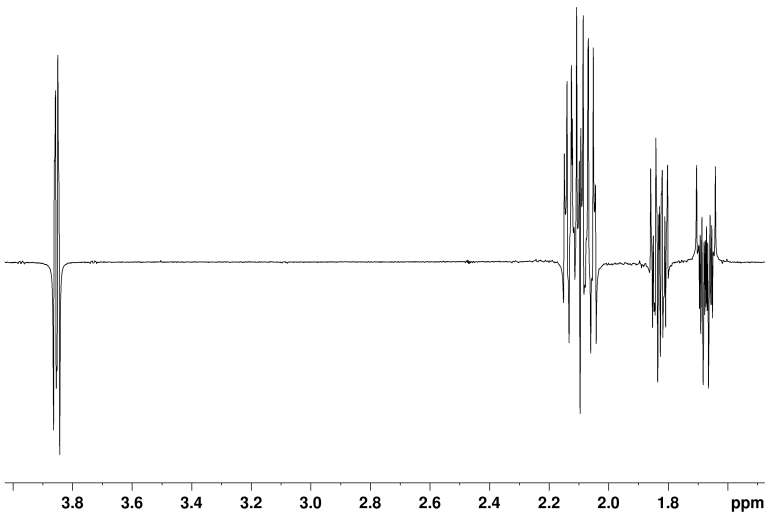

(b)

Figure 4.18: The experimental best 2HG spectra for the chemical shift 2.26 ppm at TE = 130 ms at 60 MHz (a), and 110 ms at 600 MHz (b).

The spectrum for the optimal TE for peak 3 at the chemical shift of 1.8 ppm, as determined from the analyses, is presented in Figure 4.19. The best spectrum at 60 MHz with TE = 150 ms is shown in Figure 4.19a, and the best spectrum at 600 MHz with TE = 160 ms is shown in Figure 4.19b.

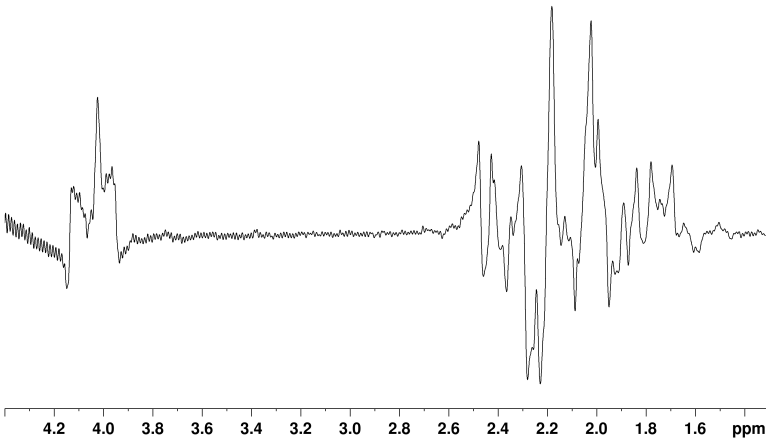

(a)

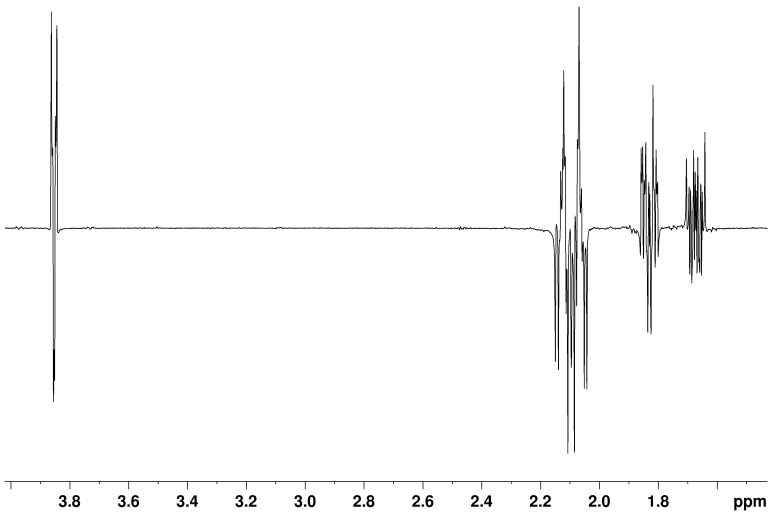

(b)

Figure 4.19: The experimental best 2HG spectra for the chemical shift 1.8 ppm at TE: 150 ms at 60 MHz (a) and 160 ms at 600 MHz (b).

The optimal TE for an editing sequence is 90 ms at a high magnetic field, 600 MHz, and 100 ms at a lower magnetic field, 60 MHz. Consequently, the expected optimal TE for the editing spectra with the MEGA-PRESS sequence at 500 MHz is between 90 ms and 100 ms. For the detection of 2HG with a sLaser sequence, the optimal TE at a high magnetic field, 600 MHz, is 110 ms, as tested on a 3 T system in earlier research. At a lower magnetic field, 60 MHz, the optimal TE for the detection of 2HG with a sLaser sequence is 130 ms. Therefore, the detection of 2HG at 3 T is assumed to be closer to 130 ms.

4.3 Calibration curves at 500 MHz

The calibration curves for 2HG were created from the edited spectra using the MEGA-PRESS sequence, as explained in Chapter 3. Given that the concentration of 2HG in a tumor *in vivo* is around 4 mM, the calibration curves were made with concentrations ranging from 0 mM to 10 mM of 2HG. When using edited spectra, the lowest SI on the editing peak in the OFF spectrum is desired. The SI of the OFF spectrum in a MEGA-PRESS sequence is equivalent to a PRESS spectrum with the same parameters. The SI of the OFF spectra versus the respective TE is plotted in Figure 4.20a, and the SI of the PRESS sequences with the same parameters is plotted against the respective TE in Figure 4.20b. The TE values used in the calibration curves are 68 ms, 74 ms, 80 ms, and 97 ms, as depicted in Figure 4.20a. Based on Figure 4.20, it was expected that the best TE for the calibration curves would be 97 ms, because of the lowest SI from the plot. The data used to make the calibration curves can be found in Appendix C.3 and C.2, and the plots of the SI vs TE for all the concentrations of pure 2HG and 2HG in BRAINO can be found in Appendix D.2.

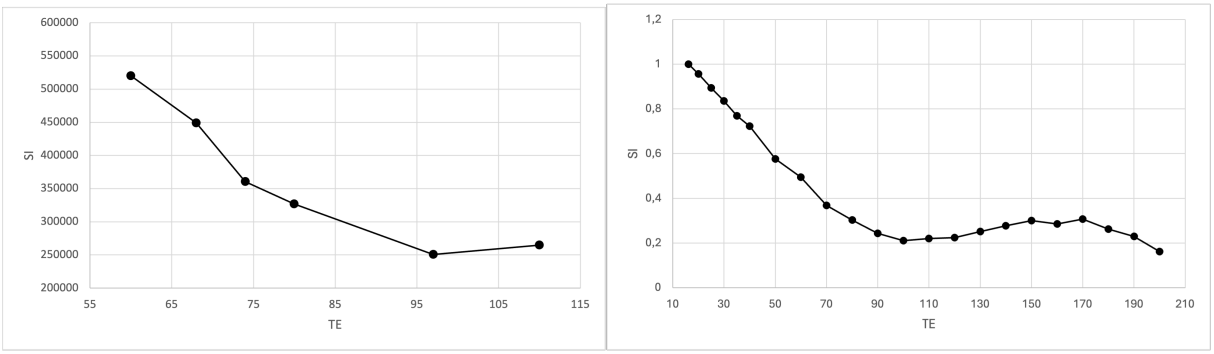

(a) (b)

Figure 4.20: SI vs TE at 500 MHz for: MEGA-PRESS OFF (a) and PRESS (b).

Based on the literature reviewed before the experiments, as mentioned in the introduction, the TE times focused on for the MEGA-PRESS sequence were 68 ms, 74 ms, 80 ms, and 97 ms. The TE of 68 ms was likely taken from MEGA-PRESS GABA experiments and was not expected to be as effective as the higher TE values. This expectation was based on the optimal TE determined in Chapter 4.3, which was 90 ms for a magnetic field of 600 MHz and 100 ms for a magnetic field of 60 MHz. Earlier studies had examined the edited spectra of a MEGA-PRESS sequence with TE = 60 ms. However, this was excluded from this study after the initial spectra were accumulated, as the time was too short for the signal to be fully refocused. Since the calibration curves were made from spectra at a magnetic field of 500 MHz, the optimal TE was expected to be around 90 ms. The TE of 110 ms was also excluded based on the observation in Figure 4.20a, which showed an increase in SI for TE = 110 ms compared to TE = 97 ms.

The SI from the edited MEGA-PRESS spectra were plotted against the TE and are depicted in Figure 4.21. The trends on the curves are similar for all concentrations, both for pure 2HG and for 2HG in BRAINO, with the plots displayed in the Appendix. The concentration of 2HG displayed in Figure 4.21 is 4 mM of pure 2HG and 4 mM of 2HG in BRAINO. This concentration is chosen because it is similar to the concentration of 2HG *in vivo*, providing an appropriate signal-to-noise ratio. Based on Figure 4.21, it is expected that the slope of the calibration curve

will increase with the TE up to around 97 ms. When comparing Figure 4.20a with Figure 4.21, it can be seen that the SI reaches a max negative value around 97 ms, and thus would also reach a maximum refocus around the same TE.

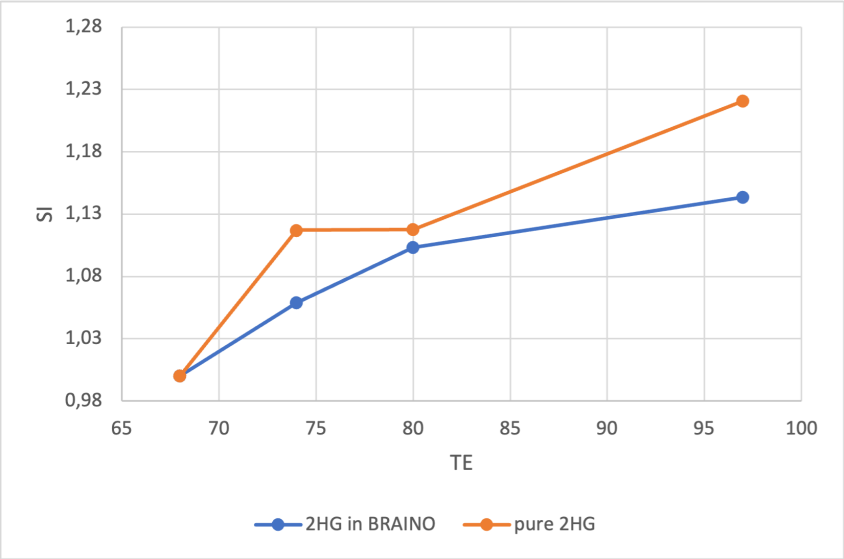

Figure 4.21: SI vs TE at 500 MHz for edited 2HG at 4.02 ppm of 4 mM pure 2HG (red) and 4 mM 2HG in a brain metabolite solution (blue).

4.3.1 2-10 mM 2HG

Figure 4.22 displays the calibration curves for pure 2HG at the chemical shift of 4.02 ppm from the MEGA-PRESS sequence at TE = 68 ms (a), 74 ms (b), 80 ms (c), and 97 ms (d). The calibration curves exhibit good linearity, as indicated by the R-value. Each curve has an $R^2 > 0.9$, demonstrating good linearity, and all calibration methods can be used to monitor changes in the metabolite concentration.

Due to incomplete refocusing in the edited spectra used for the calibration curve, the SI in the calibration curves is relatively lower than the theoretical SI for 2HG. In the y-axis of the plots in Figure 4.22, the SI is represented. As expected, the SI increases with TE, which is also reflected in the slope of the calibration curves. The slope and linearity of each calibration curve are displayed in Table 4.4.

Table 4.4: The slope and linearity (R^2) of the calibration curves for pure 2HG

Calibration curve	Linearity [R^2]	Slope
Figure 4.22a	> 0.9984	72547
Figure 4.22b	> 0.9978	75638
Figure 4.22c	> 0.9978	82708
Figure 4.22d	> 0.9977	82434

The slope is steepest in Figure 4.22c. When the SI of the OFF spectra from the MEGA-PRESS sequence is subtracted from the ON spectra where the signals are fully refocused, the

SI of the edited spectra increases, as shown in Figure 4.21. Figure 4.20a displays the SI of the OFF spectra from the MEGA-PRESS sequence used in the modulation of the calibration curves. In Figure 4.21, the SI from the edited MEGA-PRESS spectra are shown. The SI for the MEGA-PRESS sequences with TE = 80 ms and 97 ms are similar. The slope of the calibration curves is determined by the difference between the highest SI and the lowest SI in the curve. The calibration curve for TE = 80 ms has the highest difference between the highest and lowest SI, resulting in the steepest slope.

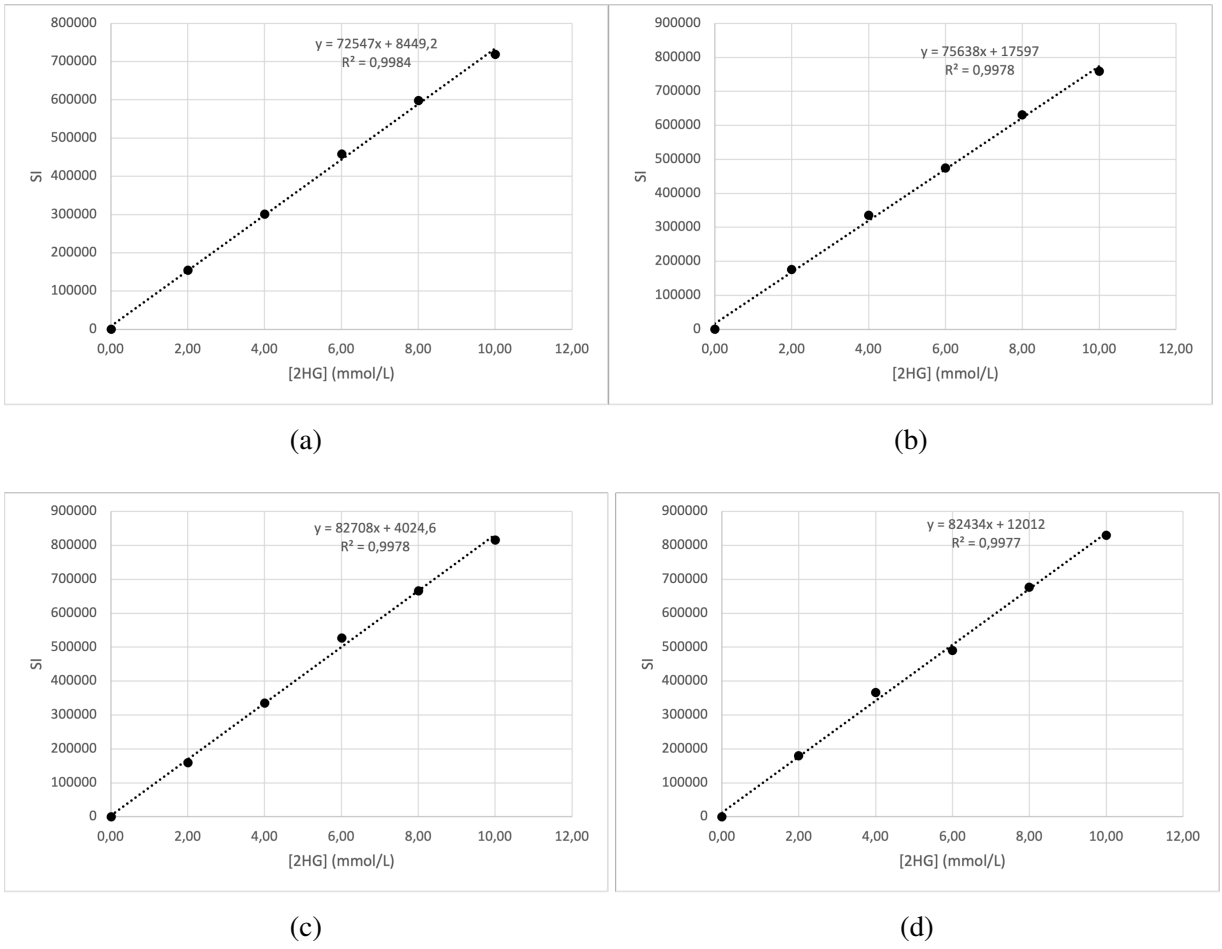

Figure 4.22: Calibration curves for pure 2HG at 4.0 ppm, with MEGA-PRESS at TE = 68 ms (a), 74 ms (b), 80 ms (c) and 97 ms (d).

4.3.2 2-10 mM 2HG in the brain metabolite solution

Figure 4.23 displays the calibration curves for 2HG in the brain metabolite solution at the chemical shift of 4.02 ppm from the MEGA-PRESS sequence at TE = 68 ms (a), 74 ms (b), 80 ms (c), and 97 ms (d). These calibration curves also show good linearity, with all $R^2 > 0.9$, indicating that the methods can be used to monitor concentration changes in 2HG in BRAINO.

As with the calibration curves for pure 2HG, the OFF spectra are not turned 180°, resulting in an incompletely refocused edited spectrum for each sequence. Consequently, the SI in the calibration curves is relatively lower than the theoretical SI for 2HG when measured against the SI for NAA in the brain metabolites solution. As mentioned for the calibration curves for pure

2HG, Figure 4.20 shows that the signal at 4.02 ppm has high negativity around 80 ms and 97 ms. Therefore, the SI for the edited spectra is expected to increase with TE up to around 100 ms. This will be reflected in the slope of the calibration curves, as shown in Table 4.5.

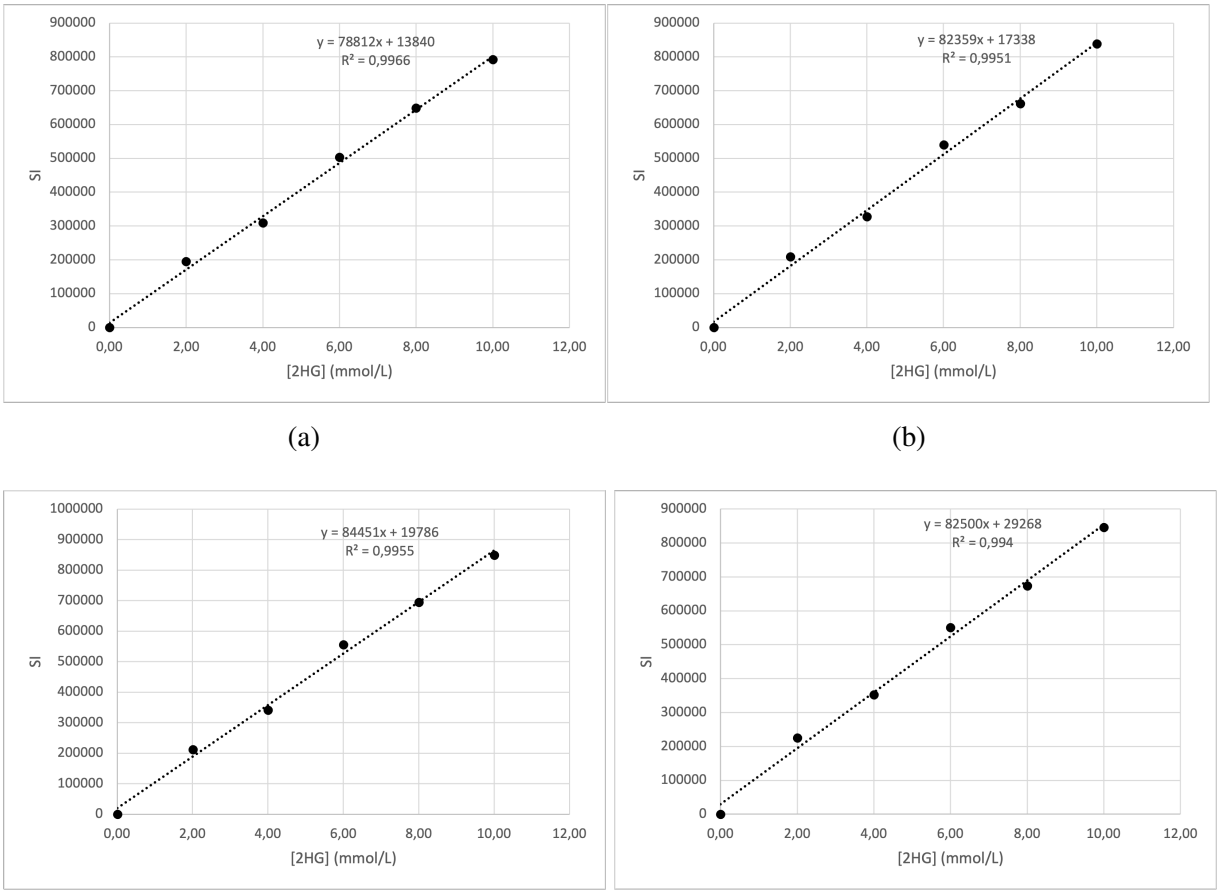

Figure 4.23: Calibration curves for 2HG in the brain metabolite solution at 4.0 ppm, with MEGA-PRESS at TE = 68 ms (a), 74 ms (b), 80 ms (c) and 97ms (d).

The slope for the calibration curves is highest in calibration curve 4.23c, as expected from the SI on the OFF spectrum and edited spectrum from the MEGA-PRESS sequence with TE = 80 ms, as shown in Figure 4.20a. The SI differences between concentrations at TE = 80 ms are greater than those at TE = 97 ms. Therefore, the slope is higher at TE = 80 ms, even though the SI at the OFF spectrum for TE = 97 ms is more negative than that for TE = 80 ms.

Table 4.5: The slope and linearity (R^2) of the calibration curves for 2HG in BRAINO

Calibration curve	Linearity [R^2]	Slope
Figure 4.23a	> 0.9966	78812
Figure 4.23b	> 0.9951	82359
Figure 4.23c	> 0.9955	84451
Figure 4.23d	> 0.9940	82500

4.4 3D-printed phantom data

In this section, the results from the 3D-printed phantom will be presented. Pictures of the 3D-printed phantom, both outside and inside the 3 T GE scanner, and an MRI of the phantom with voxel selections will be displayed. Additionally, results from disturbances detected inside the ping pong balls will be discussed. The data accumulated with the phantom at the 3 T GE scanner will be presented, along with some modulation and quantification results performed with Osprey.

4.4.1 3D-printed phantom

The 3D-printed phantom was created using the Form 3+ 3D printer, as explained in Chapter 3 and shown in Figure 3.6. The design was based on drawings by Morten Kristoffersen from the Medical Technology department, depicted in Figure 3.5.

Figure 4.24 displays several pictures of the finished 3D-printed phantom without any liquid. Figure 4.24a shows the phantom without a lid and the smaller compartments (ping pong balls) attached to the claws. Figure 4.24b shows the phantom without a lid but with the smaller compartments attached (ping pong balls). Figure 4.24c shows the phantom and the lid. To separate the different smaller compartments, Omega-3 pills were attached to the outside of the phantom, and aligned with each smaller compartment.

(a) (b) (c)

Figure 4.24: Pictures of the 3D-printed phantom: with claws (a), with ping pong balls (b) and with the lid (c).

The phantom was placed inside the 3 T GE scanner in the head coil, as shown in Figure 4.25a. Figure 4.25b shows the 3D-printed phantom filled and sealed with the lid, in front of the computer displaying the MRI and MRS of the respective phantom. Figure 4.25c shows the MRI of the phantom with the smaller compartments and the markings with Omega-3 pills on the sides. These marks were used, as explained, to differentiate the compartments.

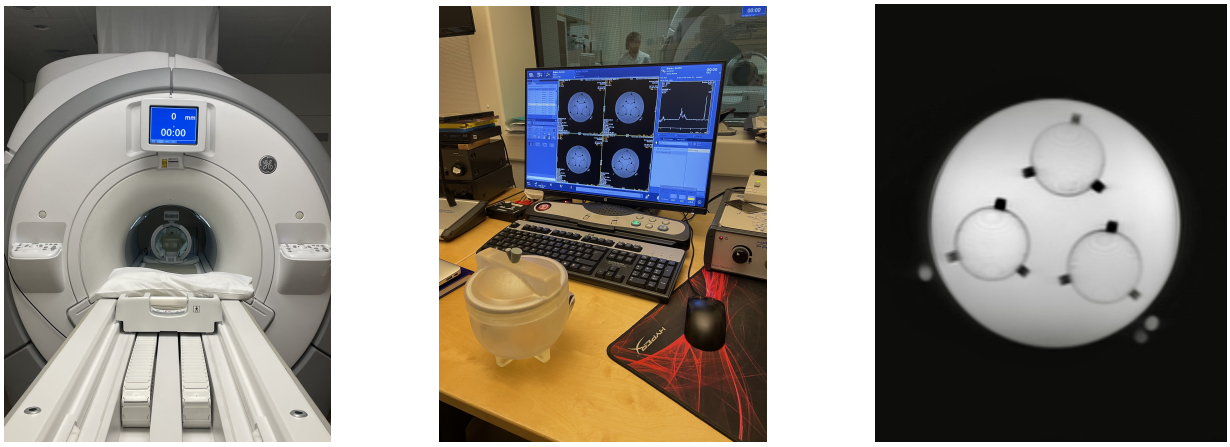

(a) (b) (c)

Figure 4.25: The 3D-printed phantom placed inside the head coil inside the 3 T GE scanner at HUS (a), a filled and sealed 3D-printed phantom in front of the computer with the respective MRI and MRS (b), and the MRI of the 3D-printed phantom with the smaller compartments marked with Omega-3 pills (c).

The MRI was acquired in three directions to accurately place the voxel inside the smaller compartments. Initially, a volume MRI was obtained for the first phantom data. However, after further examination, it was determined that a three-directional MRI was sufficient to place the voxel inside the smaller compartments.

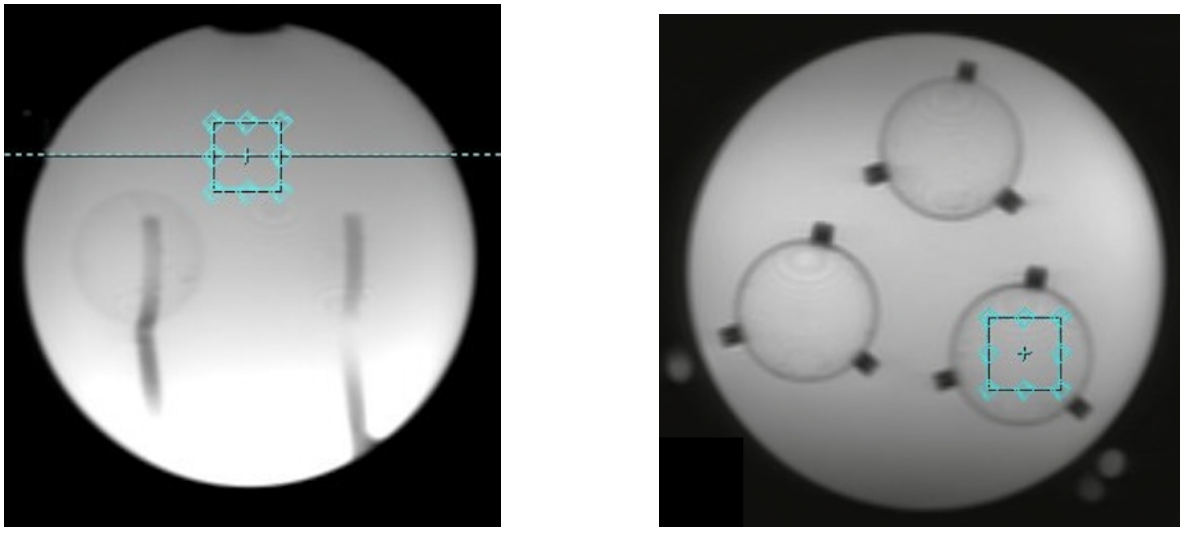

(a) (b)

Figure 4.26: The $30 \times 30 \times 30\ mm^2$ voxel placement in the phantom at the 3 T GE scanner at HUS. The placement outside (a), and inside (b) of the smaller compartments.

Figure 4.26 displays two examples of voxel placement. For the acquisition of the brain metabolite solution without 2HG, the voxel was placed outside the smaller compartments, as shown in Figure 4.26a. An example of voxel placement inside the ping pong balls is displayed in Figure 4.26b. A 3D MRI of the voxel placement is included in Appendix D.3. The voxels were

placed in the middle of the ping pong balls in such a way that they did not touch the walls. Due to the geometric structure of the ping pong balls, the shimming was expected to be quite good. The linewidth of the spectra from the voxels placed inside the ping pong balls was 2, with a water suppression of 99%, which is quite good for phantom data on a 3 T GE scanner. The linewidth of the voxel placed outside the smaller compartments was not always as good as those inside, varying from 2 to 3, with a water suppression of 99%. This could be due to the non-circular geometry around the voxel placed outside the small compartments. The ping pong balls were attached to the phantom with a claw-like structure, which could interfere with the signals in the outside voxel.

As explained in Chapter 3, the closing mechanism for the ping pong balls was tested with a mixture of 10 M sugar inside the ping pong balls and pure water outside, and the different solutions were tested after a week. The results showed that both the Loctite and the electrical tape sealed the syringe hole in the ping pong ball effectively. Parafilm was excluded because the sharp edges of the claw construction tore holes in the parafilm when the ping pong balls were attached to the phantom. Electrical tape was chosen as the closing mechanism because it could easily be removed and reattached if the solutions inside the ping pong balls needed to be removed or refilled.

Three different phantoms were made, corresponding to sample numbers 24, 25-27, 30-32, and 34-36 from Table 3.3. The first phantom, with sample numbers 24-27, was used over a few weeks. The data acquired after one week showed a different signal distribution in the spectrum compared to those acquired after one day. To determine the peak change, the solutions were tested at 600 MHz.

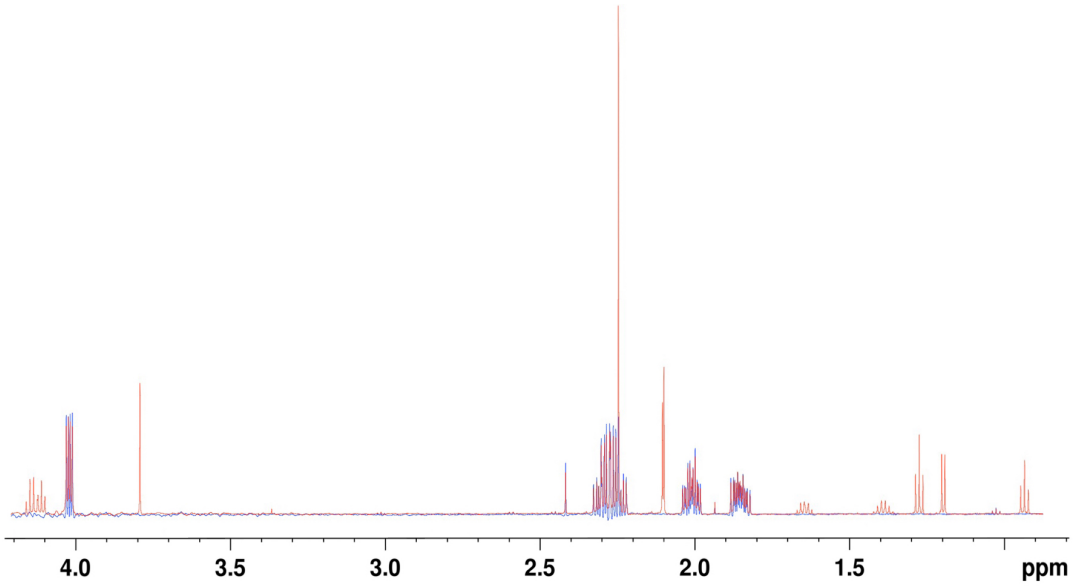

Figure 4.27: The spectrum from the solution in phantom 1, the ping pong ball with 4 mM 2HG: before it was filled in the ping pong ball (blue spectrum) and after it had stayed in the ping pong ball for 1 week (red spectrum).

Figure 4.27 displays two spectra: the blue spectrum shows the signals before the solutions were filled into the ping pong balls, and the red spectrum shows the signals after the solutions had been inside the ping pong balls for one week.

The stability of the 2HG molecule in the brain metabolite solution in the plasma/serum buffer stored at 25°*C* was tested over six months. The 2HG SI did not change from September 22., 2023, to March 19., 2024, as shown in Figure 4.28.

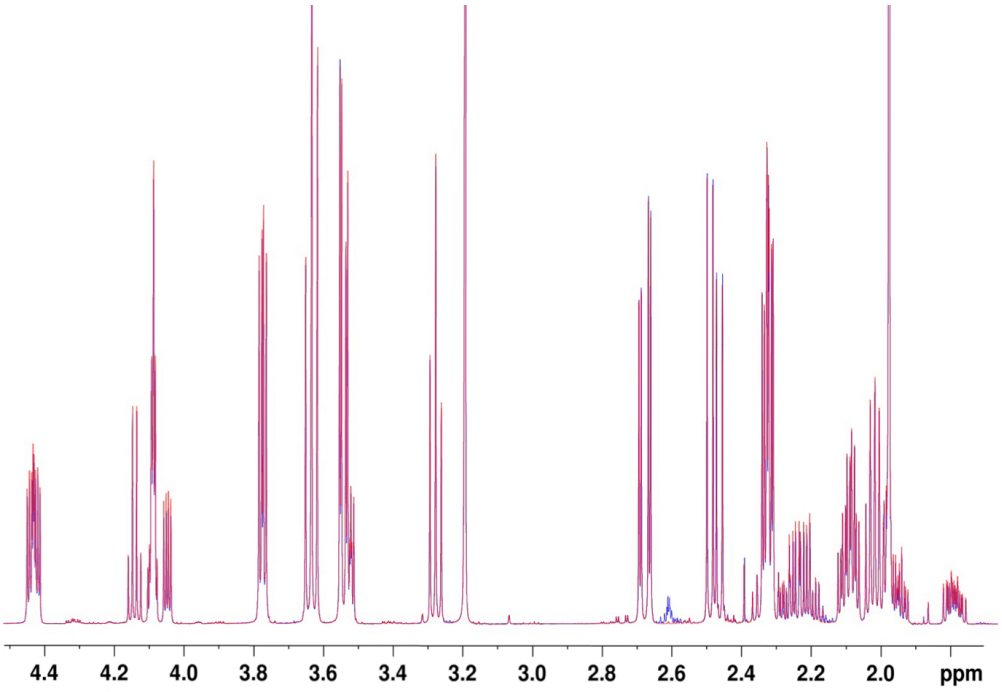

Figure 4.28: The SI of 2HG and the brain metabolites in a 6-month time period: March 19. 2024 (red spectrum) and September 22. 2023 (blue spectrum).

The signal at 2.6 ppm from the spectrum of 2HG in BRAINO, acquired before any time had passed, was observed to disappear over the six months. No research was conducted to identify this signal, as it is not in the overlapping chemical shift range for 2HG.

Based on the results of the 2HG stability test, it was assumed that the peak change in the spectrum after one week was due to the ping pong balls or the electrical tape. To investigate this, the ping pong balls and the electrical tape were cut and placed in the buffer solution for one week and then tested at 600 MHz, as displayed in Figure 4.29. The blue spectrum in Figure 4.29 shows the solution from the cut ping pong ball left in the plasma/serum buffer for one week, and the green spectrum shows the solution from the cut electrical tape left in the plasma/serum buffer for one week.

When the spectra are compared with the spectrum of the solution kept in the ping pong ball for one week, the peaks align quite well with the signals from the ping pong ball and the electrical tape, as shown in Figure 4.29. The peaks from the signals of the cut ping pong ball left in the buffer solution for one week align well with the disturbance signals in the spectrum of the 2HG solution left inside the ping pong ball for one week.

The spectra are focused around 1 ppm to 2.5 ppm, as this is where the disturbance signals were visible in the spectra from the 3 T GE scanner after one week. The 2HG signals around 2.26 ppm are the ones examined on the 3 T GE scanner. The signals from the ping pong ball around 1 ppm do not interfere with any of the desired signals in this study. The metabolite peaks in this area in a brain metabolite solution come from lac.

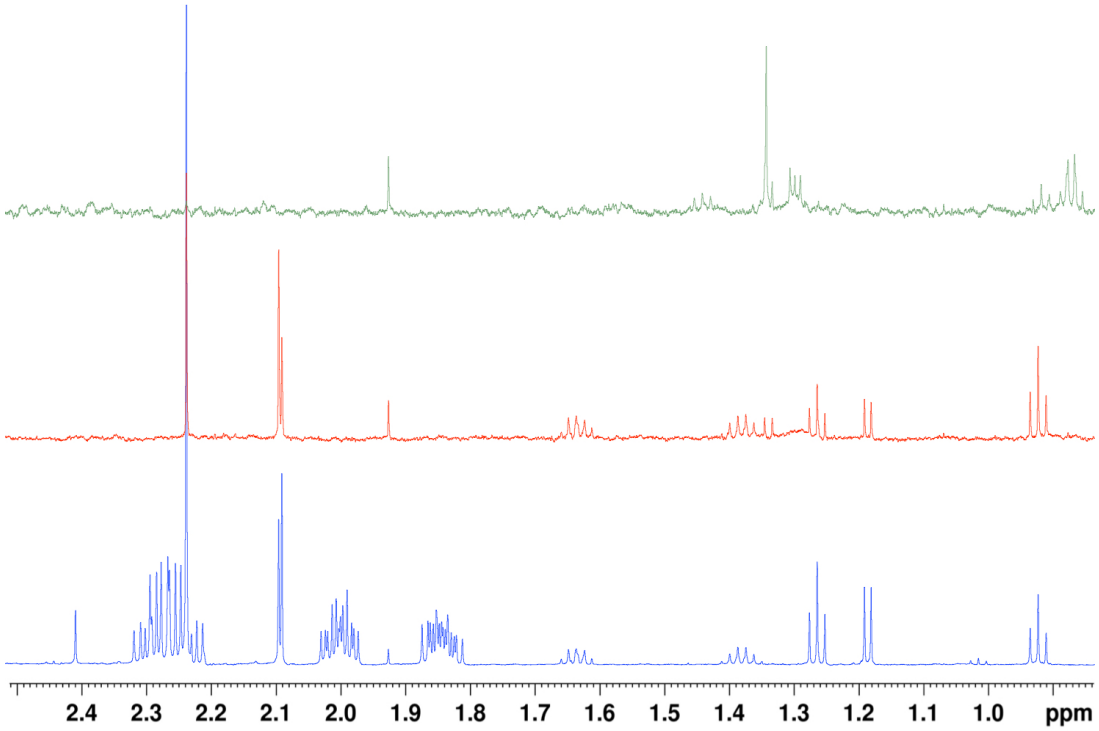

Figure 4.29: Comparison of the spectrum from 4 mM 2HG solution kept inside ping pong ball 2 in phantom 1 (blue spectrum), the ping pong ball solution (red spectrum), and the electrical tape solution (green spectrum).

The peak that most likely changed the peak structure in the spectra for 2 mM 2HG at the 3 T GE scanner after one week is the singlet at 2.24 ppm from the pollution. For spectra with higher 2HG concentrations, the peaks are not visibly changed. This could be because the SI for 2HG is higher, and the SI for the disturbance peaks remains the same across all compartments. Consequently, in compartments with a higher concentration of 2HG, the signals are less affected in a lower magnetic field where the coupling pattern is of a higher order.

The signals originating from the ping pong balls did not appear in the spectra after one day. The ping pong balls were filled 1-2 hours before the phantom data were acquired at the 3 T GE scanner, serving as a short-term solution for this thesis. The disturbance from the ping pong balls needs to be resolved in further studies.

4.4.2 Phantom data

Three different phantom compositions were created using the 3D-printed phantom, as explained. The samples used in these phantoms were sample numbers 24, 25-27, 30-32, and 34-36 from Table 3.3. Sample number 24, a brain metabolite solution, was used as the surroundings in all the phantoms. The smaller compartments contained different concentrations of 2HG, NAA, Glu, and BRAINO. In phantom 3, a contrast agent was added to all the solutions. The solutions in all the phantoms are detailed in Table 3.12. The overlapping metabolites NAA and Glu were examined further due to their overlapping nature, and 2HG was added to the solution in another ping pong ball to see how the three metabolites behave in conjunction. The concentration of 2HG was kept at 4 mM, reflecting its concentration *in vivo* in tumors. All the spectra were modulated and quantified with Osprey, and some of the spectra will be displayed in this section.

As explained earlier, the pulse sequences focused on were sLaser, PRESS, and MEGA-PRESS. At the 3 T GE scanner, the sLaser sequence and the signal at 2 ppm were the focus. A short PRESS sequence was run, along with some MEGA-PRESS sequences with TE = 68 ms, 74 ms, 80 ms, and 97 ms, consistent with the experiments done at NNP. The MEGA-PRESS sequences were analyzed with Gannet, but the results were not adequate. The sLaser sequences with TE = 30 ms and 100 ms to 140 ms were run. The TE times were chosen based on the results from the optimal TE analysis done at NNP, with the expected best TE between 110 ms and 130 ms for the signals at 2.26 ppm, peak 4 and 4' for 2HG.

Phantom 1

The compartments in phantom 1 contained different concentrations of 2HG, as explained. The concentration of 4 mM was chosen for the subsequent phantoms due to its similarity to the concentration of 2HG *in vivo* in tumors.

When the solutions used in the experiments at the 3 T GE scanner were prepared, the spectral analysis programs LCModel and Osprey were not yet available on MacOS, and the reference peaks used in the programs had therefore not been identified. The basis set acquired from MRSCloud [42] was made with Cr and NAA as standards, which could not be removed. As a result, the basis set applied in Osprey indicated that all the solutions contained Cr and NAA. In Osprey, Cr is also used as a reference peak, and since the solutions in phantom 1 neither included Cr nor NAA, the modulation and quantification done by Osprey were not usable. However, the processing and spectra read by Osprey can be used and are displayed in Figure 4.30, 4.31, 4.33, and 4.34.

Figure 4.30 displays the modeled spectrum with Osprey from the short TE (35 ms) PRESS sequence. The PRESS spectra with TE = 35 ms acquired on the phantoms with pure 2HG on the 3 T GE scanner at HUS were unusable in Osprey. The best spectrum processed by Osprey is the one modeled in Figure 4.30. As depicted, the spectrum, even after alignment and averaging, still had an off baseline, and the signal-to-noise ratio did not improve as much from averaging as expected for any of the PRESS spectra analyzed by Osprey. Therefore, the spectra accumulated by the short TE PRESS sequence were chosen not to be examined further.

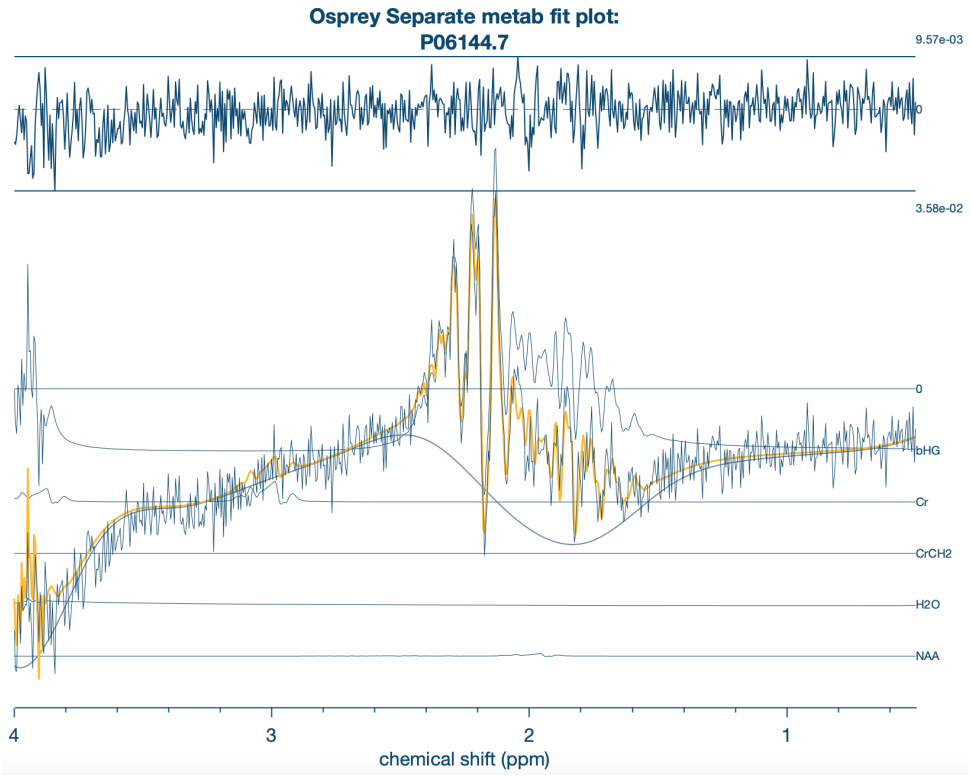

Figure 4.30: The modeling done by Osprey on the spectrum of an 8 mM 2HG from a PRESS sequence at TE = 35 ms on the 3 T GE scanner at HUS.

Figure 4.31 displays the Osprey-processed spectra from the sLaser TE = 30 ms sequence at the 3 T GE scanner at HUS. Each figure contains the spectrum from one of the small compartments in phantom 1. Figure 4.31a shows the spectrum from the solution in sample number 25, 2 mM 2HG; Figure 4.31b shows sample number 26, 4 mM 2HG; and Figure 4.31c shows sample number 27, 8 mM 2HG.

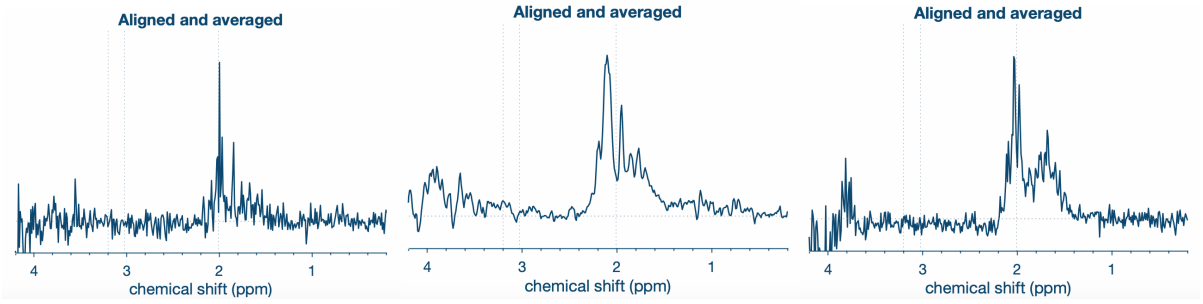

(a) (b) (c)

Figure 4.31: The processed Osprey spectrum from the sLaser sequence with TE = 30 ms of 2HG concentration: 2 mM (a), 4 mM (b), 8 mM (c).

As explained, phantom 1 was analyzed over several weeks, and the disturbance from the ping pong balls affected the signals, especially in the spectra with 2 mM 2HG. The spectra displayed in Figure 4.31 are from the experiments conducted during the first two days after the phantom was filled.

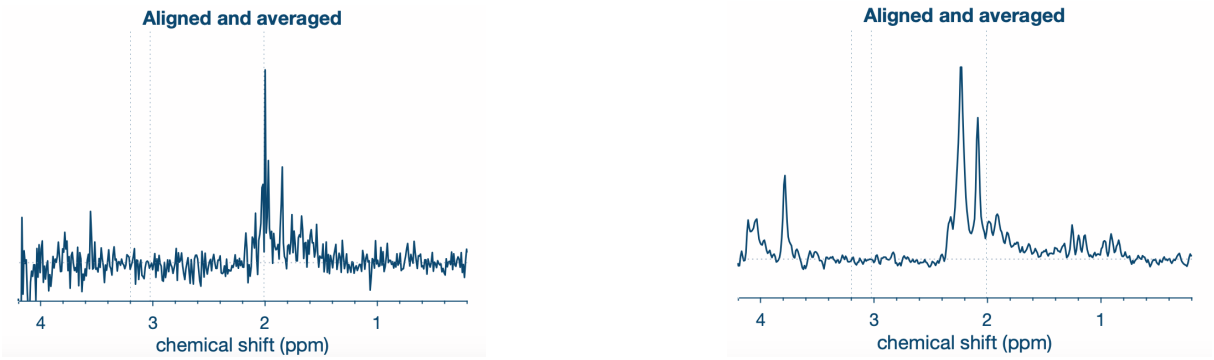

(a) (b)

Figure 4.32: The spectra of 2 mM 2HG from a sLaser sequence with TE = 30 ms at the 3 T GE scanner at HUS aligned and averaged by Osprey. Spectrum (a) were obtained 1 day after the filling, and spectrum (b) were obtained 1 week after the filling.

In Figure 4.32, the spectra of 2 mM 2HG from a sLaser sequence with TE = 30 ms obtained after 1 day, Figure 4.32a, and after 1 week, Figure 4.32b, are displayed. In Figure 4.32a, the S/N ratio is lower than in Figure 4.32b, but the peak differences in the two spectra are still visible. The spectrum of the pollution from the ping pong ball displayed a singlet at 2.24 ppm. This singlet is most likely the peak that interferes the most with the signal and disrupts the peak-splitting pattern. To avoid the effect of the pollution from the ping pong balls, the spectra in the later phantoms were obtained within one day after filling.

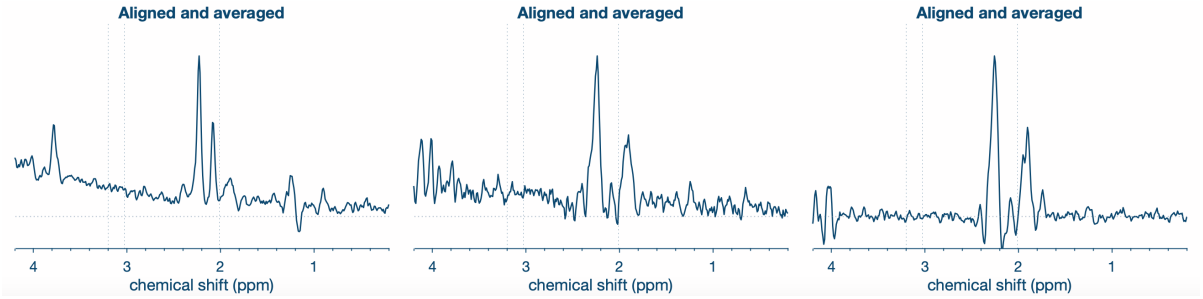

(a) (b) (c)

Figure 4.33: The processed Osprey spectra from the sLaser sequence with TE = 110 ms at the 3 T GE scanner at HUS of 2HG concentration: 2 mM (a), 4 mM (b), 8 mM (c).

Figure 4.33 displays the Osprey-processed spectra from the sLaser TE = 110 ms sequence at the 3 T GE scanner at HUS. Each figure contains the spectrum from one of the small compartments in phantom 1. Figure 4.33a shows the spectrum from the solution in sample number 25 (2 mM 2HG), Figure 4.33b shows sample number 26 (4 mM 2HG), and Figure 4.33c shows sample number 27 (8 mM 2HG). The spectra in Figure 4.33a were acquired one week after

filling, and the signal is therefore affected by the pollution. The peak behavior in Figure 4.33b and 4.33c is as expected, mostly positive. The peak splitting is lower than expected based on the peak splitting in the spectra at 60 MHz, Figure 4.18a, and 600 MHz Figure 4.18b. This could result from the alignment, averaging, and processing done in Osprey, which improves the S/N ratio, phase, and baseline of the spectra.

Figure 4.34 displays the Osprey-processed spectra from the sLaser TE = 130 ms sequence at the 3 T GE scanner at HUS. Each figure contains the spectrum from one of the small compartments in phantom 1. Figure 4.34a shows the spectrum from the solution in sample number 25 (2 mM 2HG), Figure 4.34b shows sample number 26 (4 mM 2HG), and Figure 4.34c shows sample number 27 (8 mM 2HG). The spectra in Figure 4.34a were acquired one week after filling, and the signal is therefore affected by the disturbance. The spectra processed by Osprey in Figure 4.34 do not have as good an S/N ratio or baseline as those acquired with TE = 110 ms at the 3 T GE scanner. Whether this is because a sLaser sequence with TE = 110 ms is better than one with TE = 130 ms or just a coincidence cannot be determined without several spectra acquired at the same TE. However, based on the displayed spectra, it seems that at 3 T, a TE of 110 ms is preferred over TE = 130 ms.

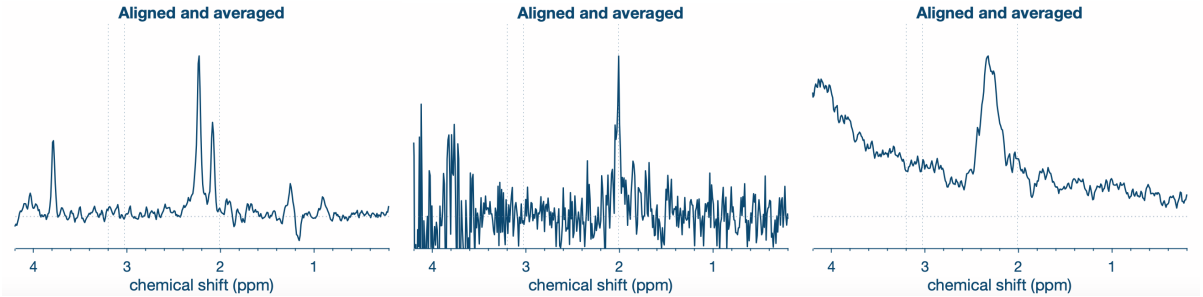

(a) (b) (c)

Figure 4.34: The processed Osprey spectra from the sLaser sequence with TE = 130 ms of 2HG concentration: 2 mM (a), 4 mM (b), 8 mM (c).

The quantification done by Osprey on the data from phantom 1 is not displayed or further examined due to the lack of reference peaks, Cr, or NAA. As explained, the basis sets from MRICloud [42] use Cr and NAA as references. Consequently, the quantification done by Osprey on the solution containing only 2HG and TSP resulted in an incorrect assumption of mostly NAA.

Brain metabolite solution

Figure 4.35 displays the Osprey-processed spectra of a brain metabolite solution, sample number 24, at TE = 30 ms Figure 4.35a, TE = 110 ms Figure 4.35b, and TE = 130 ms Figure 4.35c. These spectra were acquired to observe how the brain metabolites in a brain metabolite solution without 2HG behave at the desired TE for the detection of 2HG. The spectra of the BRAINO solution were acquired from phantom 2. The solution, sample 24, was initially in the large compartment of phantom 1 and was later refilled in the large compartment of phantom 2. This could have resulted in some contamination in the signals, but it was not visible in any of the spectra for the brain metabolite solution, Figure 4.35 and 4.36. Additionally, due to the lack of accuracy in the quantification, no contamination could be detected in the quantification either.

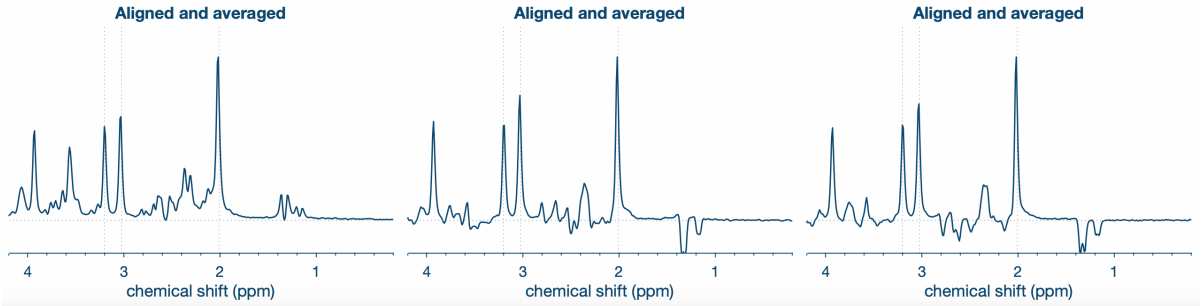

(a) (b) (c)

Figure 4.35: The processed Osprey spectra from the sLaser sequence at the 3 T GE scanner at HUS on a brain metabolite solution at TE = 30 ms (a), 110 ms (b), 130 ms (c).

Figure 4.36 shows the modulation of a brain metabolite solution, where the yellow spectral line represents the modulated spectrum based on the basis spectra from MRSCloud. Each spectral line below the experimental spectrum represents the peaks Osprey attributes to each metabolite, based on the basis set obtained from MRICloud [42]. The basis sets are implemented in Osprey as explained in Chapter 3. Osprey aligns each metabolite spectrum from the basis sets to the experimental spectrum. For instance, when NAA is fitted to the experimental spectrum, the peaks Osprey identifies as belonging to NAA are subtracted from the experimental spectrum, and this process continues for each metabolite until Osprey has aligned each peak with an associated metabolite.

Figure 4.36, the modulation of the brain metabolite data with sLaser TE = 30 ms is quite good, but not as good as expected. With a short TE, the phases are not significantly affected, and the basis sets should closely match the experimental data. The most surprising mismatch was with the NAA peaks. The NAA peaks from the basis set are slightly misaligned with the experimental spectrum. This recurring problem during the analysis with Osprey resulted in the NAA peaks from the basis set ”taking” some of the signals from GABA, causing the quantified GABA signal to be systematically low. In the quantification done by Osprey, the water signal is used as a reference. The quantification for the brain metabolite solution at the different TEs is described in Table 4.6.

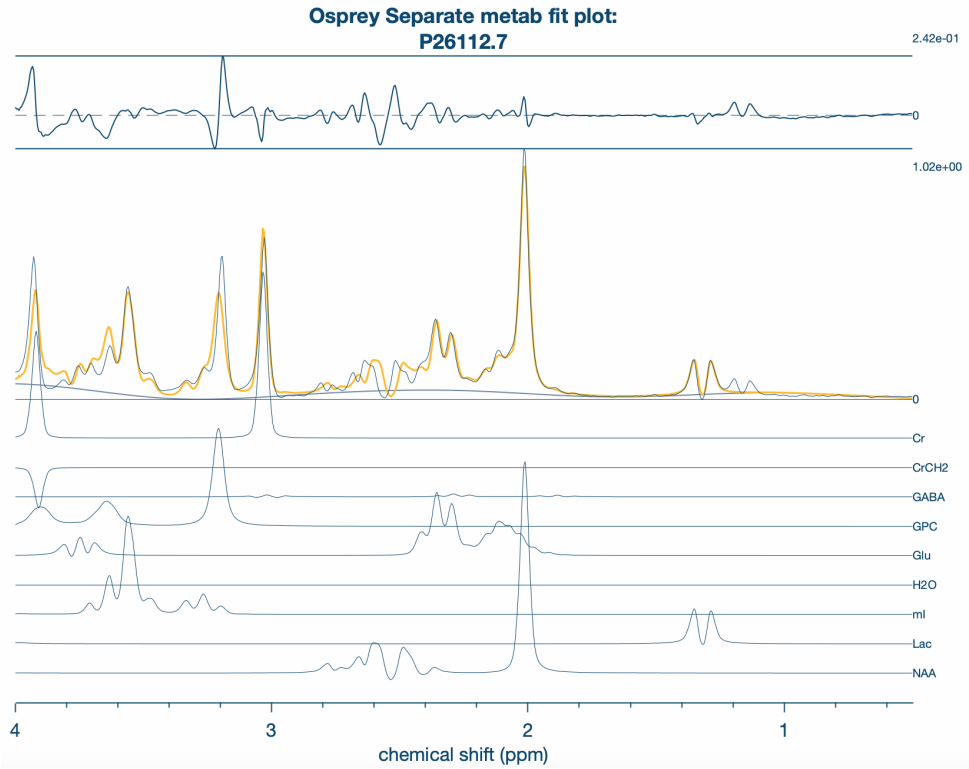

Figure 4.36: The Osprey modulation of a brain metabolite solution with sLaser at TE = 30 ms. The calculated basis set for each metabolite based on the basis set from MRICloud [42] are displayed under the experimental spectrum.

As displayed in Table 4.6, the quantification of the metabolites using a water reference is not chemically accurate. The quantified concentrations are quite different from the actual concentrations (*Exact*) of the metabolites. Osprey and LCModel are primarily designed for the analysis of spectra *in vivo*, not for phantom data. Based on the results from Osprey's quantification of the experimental data in this study, it cannot be considered an approved quantification approach from a chemical perspective. To use Osprey effectively, the method of quantification and modulation would need to be improved.

One of the main reasons for the poor accuracy with Osprey may originate from the basis sets from MRSCloud. The basis sets for the metabolites are not similar to the experimental data acquired under controlled settings. In Figure 4.36, it is especially evident that the NAA peaks in the basis set do not align with the experimental NAA peaks. Initially, it was thought that the pH of the solutions might be off, causing the peaks to misalign. However, the pH of the buffer solutions used was checked and confirmed to be 7.4.

In Table 4.6, the GABA quantification from the sLaser sequence at TE = 30 ms is relatively lower than the actual concentration compared with the other metabolites. This discrepancy may result from the mismatch between the basis set for NAA and the experimental signal from NAA, leading to the misalignment of the GABA signal with the NAA metabolite.

Table 4.6: The quantification of the metabolites (in mM) in the brain metabolite solution done by Osprey for the sLaser sequences with different TE-times acquired at the 3 T GE scanner at HUS (Each column with a TE-time is the quantification done by Osprey in mM).

Met.	Exact	TE = 30 ms	TE = 110 ms	TE = 130 ms
NAA	12.5	13.416901	8.829531	7.148865
Glu	12.5	13.306779	5.755971	5.530576
Cho	3.0	2.821227	2.307404	2.09572
m-Ins	7.5	8.008397	0.0	0.0
Lac	5.1	4.503101	3.083379	2.838074
GABA	2.0	0.533347	0.0	2.155971
Cr	10.0	8.754445	7.555362	5.243518

The quantified data were also scaled to the NAA signal to determine if the water reference affected the quantification. For the spectrum at TE = 30 ms, scaling to NAA did not improve the results. However, for the spectra at 110 ms and 130 ms, the metabolites Glu, Cho, Lac, and Cr had a similar scaling to NAA. This consistency, however, was not systematic enough to attribute the low quantification solely to the water reference.

Phantom 2

The compartments in phantom 2 contained a variation of 2HG, NAA, Glu, and a full brain metabolite solution, as explained earlier. Compartment 1 contained 12.5 mM NAA and 12.5 mM Glu, sample number 30 from Table 3.3. The spectra from this solution were acquired to observe how the overlapping metabolites behave at the desired TE for the quantification of 2HG. In compartment 2, 4 mM 2HG was added to the existing NAA and Glu solution, sample number 31 from Table 3.3. The last compartment contained 4 mM 2HG and a full brain metabolite solution. Figure 4.37, 4.38, and 4.39 display the Osprey-processed spectra from phantom 2.

Figure 4.37 shows the Osprey-processed spectra from the sLaser TE = 30 ms sequence at the 3 T GE scanner at HUS. Each figure contains the spectrum from one of the small compartments in phantom 2. Figure 4.37a displays the spectrum from sample number 30, with 12.5 mM NAA and 12.5 mM Glu. Figure 4.37b shows the spectrum from sample number 31, where 4 mM 2HG is added to the same solution as sample 30. Figure 4.37c shows the solution consisting of a full brain metabolite solution with 4 mM 2HG. From Figure 4.37a to Figure 4.37b, 4 mM 2HG is added. Since the metabolites overlap, it is difficult to separate which peaks belong to which metabolite. When studying the spectra, the SI is, as expected, higher in Figure 4.37b, with a small bump around 1.9 ppm visible. From Figure 4.37b to Figure 4.37c, a full brain metabolite solution is added. The quantification done in Osprey from the spectra from compartments 1-3 in phantom 2 with sLaser TE = 30 ms is presented in Table 4.7.

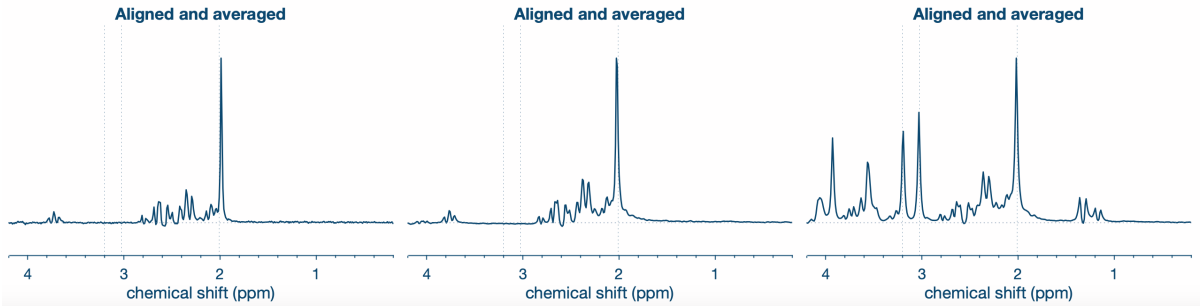

(a) (b) (c)

Figure 4.37: The processed Osprey spectra from the sLaser sequence with TE = 30 ms of: 12.5 mM NAA and 12.5 mM Glu (a), 4 mM 2HG, 12.5 mM NAA and 12.5 mM Glu (b), and 4 mM 2HG and BRAINO (c).

Figure 4.38 displays the Osprey-processed spectra from the sLaser TE = 110 ms sequence at the 3 T GE scanner at HUS. Each figure contains the spectrum from one of the small compartments in phantom 2. Figure 4.38a, 4.38b and 4.38c contain the same solutions as mentioned in the previous paragraph. The phase and baseline in Figure 4.38b are off, affecting the spectrum, and the modulation and quantification.

Based on the experiments on phantom 1 and at NNP, a TE of 110 ms was expected to give the best spectrum for the detection of 2HG. As explained previously, the quantification done in this thesis is not applicable due to the basis sets. However, the quantification of the metabolites in these spectra is mentioned in Table 4.7.

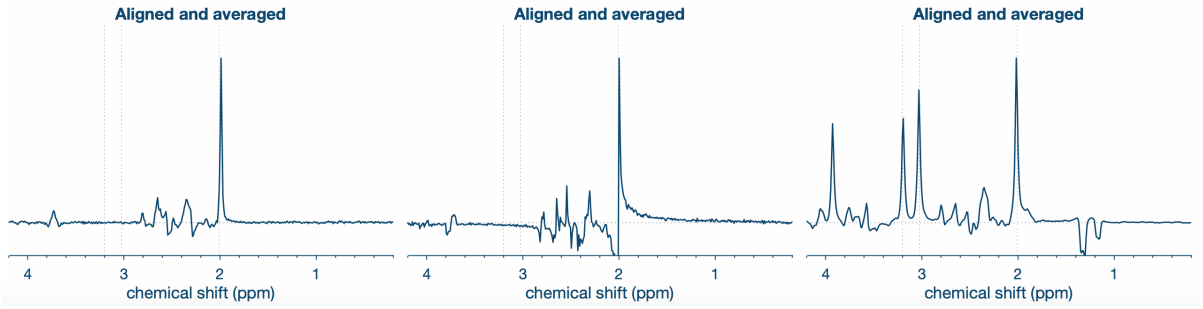

(a) (b) (c)

Figure 4.38: The processed Osprey spectra from the sLaser sequence with TE = 110 ms of: 12.5 mM NAA and 12.5 mM Glu (a), 4 mM 2HG, 12.5 mM NAA and 12.5 mM Glu (b), and 4 mM 2HG and BRAINO (c).

Figure 4.39 displays the Osprey-processed spectra from the sLaser TE = 130 ms sequence at the 3 T GE scanner at HUS. Each figure contains the spectrum from one of the small compartments in phantom 2. Figure 4.38a, 4.38b and 4.38c contain the same solutions as mentioned for the spectra at TE = 30 ms. Determining whether the 2HG signals are easier to detect at 110 ms or 130 ms at 3 T is challenging without any form of accurate SI quantification. As explained, the quantification done with Osprey is not applicable due to the inaccuracy, most likely from the inaccurate basis sets. Nonetheless, the quantification done in Osprey from the

spectra from compartments 1-3 in phantom 2 with sLaser TE = 130 ms is presented in Table 4.7.

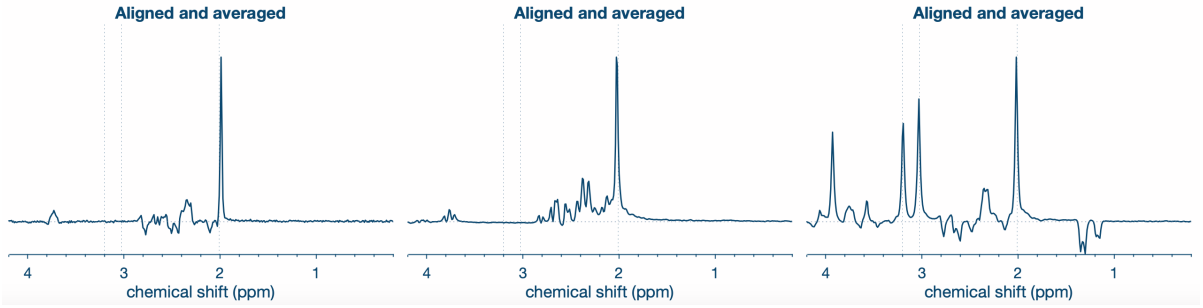

(a) (b) (c)

Figure 4.39: The processed Osprey spectra from the sLaser sequence with TE = 130 ms of: 12.5 mM NAA and 12.5 mM Glu (a), 4 mM 2HG, 12.5 mM NAA and 12.5 mM Glu (b), and 4 mM 2HG and BRAINO (c).

Table 4.7 displays the quantification of the metabolites (in mM) in phantom 2 done by Osprey for the sLaser sequences acquired with different TE times at the 3 T GE scanner at HUS. As previously explained, the quantification done by Osprey in this thesis is not applicable due to the lack of accuracy, most likely caused by the basis sets. From Table 4.7, it is evident that the over- and under-quantification are not systematic. Sometimes the quantification of 2HG is zero, and sometimes it is more than four times the actual concentration. The concentrations quantified by Osprey for the other metabolites are systematically more accurate at TE = 30 ms, and progressively less accurate at TE = 110 ms and TE = 130 ms.

Table 4.7: The quantification of the metabolites (in mM) in phantom 2 done by Osprey for the sLaser sequences acquired with different TE-times acquired at the 3 T GE scanner at HUS (Each column with a TE-time is the quantification done by Osprey in mM).

PP	Met.	Exact	TE = 30 ms	TE = 110 ms	TE = 130 ms
1	NAA	12.5	14.857426	9.478583	6.203207
	Glu	12.5	13.878698	5.186268	4.381254
2	2HG	4.0	0.629459	2.401897	18.429913
	NAA	12.5	15.438963	9.735179	6.788183
	Glu	12.5	17.369093	6.416491	5.864747
3	2HG	4.0	1.898833	0.0	4.353226
	NAA	12.5	11.521539	7.823622	6.121421
	Glu	12.5	12.65334	4.839845	4.06102
	Cho	3.0	2.618414	2.119274	2.030965
	m-Ins	7.5	7.066036	0.0	0.0
	Lac	5.1	4.284987	2.707934	2.439742
	GABA	2.0	1.531025	1.288141	2.581444
	Cr	10.0	8.283188	6.599462	5.130005

Phantom 3

The compartments in phantom 3 contained the same solutions as PP 2 in phantom 1 and PP 2 and 3 in phantom 2, with the addition of 0.5 mM of the contrast agent Clariscan. The contrast agent was added to obtain spectra more similar to those *in vivo* and to observe if the signals from the different metabolite compositions would change. The spectra of phantom 3 from a sLaser sequence with different TE times acquired at the 3 T GE scanner at HUS are displayed in Figure 4.40.

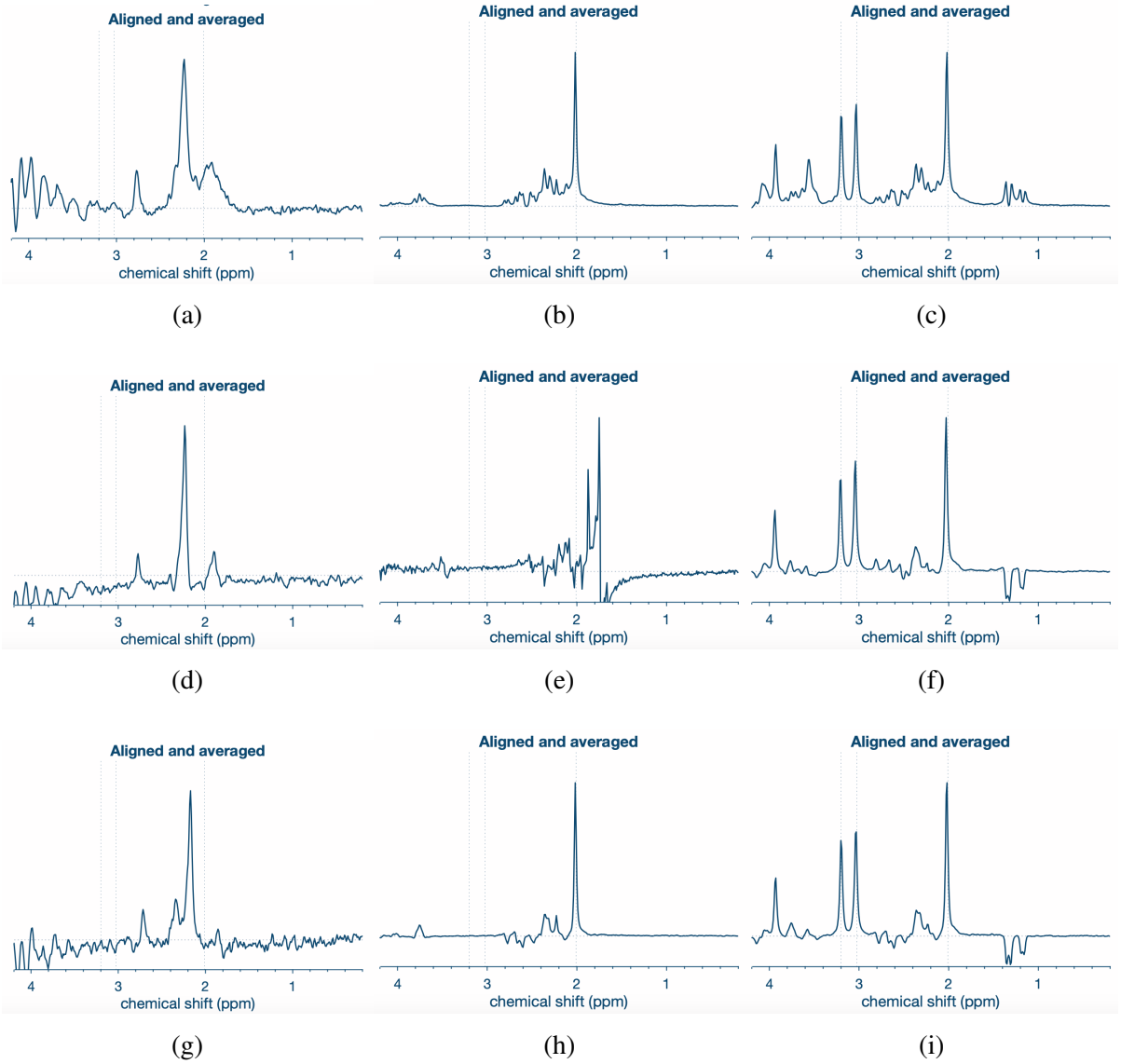

Figure 4.40: The processed Osprey spectra from the sLaser sequence of phantom 3, which include 0.5 mM of the contrast agent Clariscan, with different TE times. Figures a-c are spectra with TE = 30 ms. Figures d-f are spectra with TE = 110 ms. Figures g-i are spectra with TE = 130 ms. Figures a, d, and e have a solution with 4 mM 2HG. Figures b, e, and h have a solution with 4 mM 2HG, 12.5 mM NAA, and 12.5 mM Glu. Figures c, f, and i have a solution with 4 mM 2HG and BRAINO.

Figure 4.40a - 4.40c display the Osprey-processed spectra of phantom 3 at TE = 30 ms. Figure 4.40d - 4.40f display the Osprey-processed spectra of phantom 3 at TE = 110 ms. While Figure 4.40g - 4.40i display the Osprey-processed spectra of phantom 3 at TE = 130 ms. The first compartment in phantom 3 contain 4 mM 2HG, with the spectra displayed in Figure 4.40a, 4.40d and 4.40g. The second compartment contains 4 mM 2HG, 12.5 mM NAA and 12.5 mM Glu, and the spectra are displayed in Figure 4.40b, 4.40e and 4.40h. The third compartment consists of 4 mM 2HG in a brain metabolite solution, with the spectra displayed in Figure 4.40c, 4.40f and 4.40i.

The quantification done by Osprey on the spectra of phantom 3 is displayed in Table 4.8. The quantification of the solution with pure 2HG is not usable, as the basis set includes Cr and NAA, which are not present in the solution. Consequently, the quantification done by Osprey is mostly assigned to NAA and not 2HG. However, for the quantification done on the compartments that included more metabolites, 2HG was more frequently detected.

Table 4.8: The quantification of the metabolites (in mM) in phantom 3 done by Osprey for the sLaser sequences acquired with different TE-times acquired at the 3 T GE scanner at HUS (Each column with a TE-time is the quantification done by Osprey in mM).

PP	Met.	Exact	TE = 30 ms	TE = 110 ms	TE = 130 ms
1	2HG	4.0	0.0	0.0	1.280591
2	2HG	4.0	3.499673	5.635771	3.048681
	NAA	12.5	8.584388	6.712589	5.208105
	Glu	12.5	9.121987	2.8266	2.192446
3	2HG	4.0	2.148611	0.0	1.804441
	NAA	12.5	8.02989	6.163868	5.109336
	Glu	12.5	7.661785	2.529829	2.453778
	Cho	3.0	2.008726	1.778299	1.722831
	m-Ins	7.5	3.657869	0.0	0.0
	Lac	5.1	2.239269	1.97294	1.922612
	GABA	2.0	1.46209	0.950958	1.127321
	Cr	10.0	6.074636	5.131907	4.45432

When the spectra from phantom 2 and phantom 3 are compared, the highest SI for the peaks is lower in the spectra with a contrast agent, indicating that the signal peaks are not as sharp, as expected. Adding a contrast agent increases T_2 relaxation, resulting in a lower SI at a higher TE. The quantification done by Osprey on phantoms 2 and 3 is not similar. Based on the expectation that the spectra with a contrast agent would be more similar to those *in vivo*, the quantification on phantom 3 was expected to be more accurate than that on phantom 2, which it was not.

Both the spectra of 2HG, NAA, and Glu at 110 ms in phantoms 2 and 3 have a lower S/N ratio, poorer baseline, and phase than the other spectra. Based on the results from phantoms 2 and 3, it seems that the spectra from sLaser with TE = 130 ms are better read and quantified by Osprey. Whether this is a result of a better method with TE = 130 ms than TE = 110 ms would need to be determined after several studies on different samples with the same concentrations and TE times as done in this study.

The most accurate quantification of the metabolites was systematically achieved using the sLaser sequence with TE = 30 ms across all different compartments. This consistency underscores the reliability of TE = 30 ms for metabolite quantification in this study. Despite efforts to simulate more realistic *in vivo* conditions by adding a contrast agent in phantom 3, the expected improvement in quantification accuracy was not observed. Additionally, while the sLaser sequences at TE = 110 ms and 130 ms were anticipated to enhance the quantification of 2HG in solutions with other metabolites, as 2HG showed increased SI with these TE times, they exhibited poorer quantification with the basis sets used in Osprey. Therefore, the results suggest that shorter echo times, specifically TE = 30 ms, are preferable without a change of analysis tools and basis sets.

MEGA-PRESS on 3 T GE scanner

The signal at 4 ppm, as shown in the spectra figures from the 3 T GE scanner, Figure 4.30 - 4.40, is difficult to detect. This was unexpected based on the studies conducted on the 60 MHz and 600 MHz systems at NNP. The 4 ppm signal from 2HG is used for editing sequences, including the MEGA-PRESS sequence in this study. The MEGA-PRESS sequence was utilized for calibration curves on the 500 MHz system and was also tested on the 3 T GE scanner, with analysis attempted using Gannet. As anticipated from the spectra from the short TE PRESS and sLaser sequences performed on the 3 T GE scanner, the analysis with Gannet yielded no usable results. The 4 ppm signal from 2HG is close to the water signal at 4.7 ppm, but the proximity should not affect the signal as much as it does. Some of the analysis issues may also stem from Gannet, as it is designed for the analysis of edited GABA spectra, not edited 2HG. If the MEGA-PRESS sequence is to be used on phantom data of 2HG at the 3 T GE scanner in the future, the analysis tool should be improved accordingly.

4.5 *In vivo* spectrum

From the spectra of 2HG with different overlapping metabolites accumulated at a magnetic field from 600 MHz down to 60 MHz the difficulties of detecting 2HG is visualized. A quantification program like Osprey or LCModel with optimal basis sets will help the quantification of 2HG *in vivo* as well as *in vitro* on clinical MR scanners.

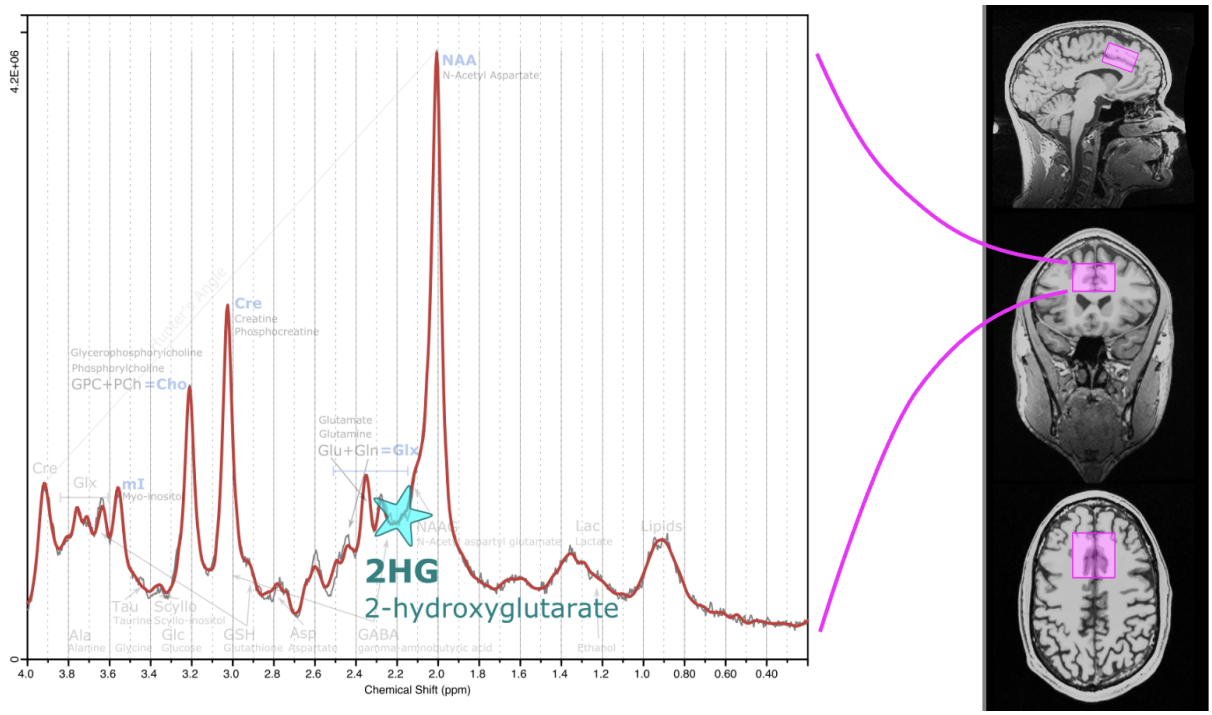

Figure 4.41: Anonymized MRS and MRI from the LGG study at HUS in courtesy of Dr. Judit Haasz.

Figure 4.41 displays an MRS spectrum acquired at the same 3T GE scanner as the phantom data. The MRS and MRI are anonymized examples from the ”LGG study” at HUS courtesy of Dr. Judit Haasz. It was from this spectrum detected an elevated concentration of 2HG, which indicates an IDH-mutation as explained in the background of 2HG. An IDH-mutation indicated that the tumor could be an Oligodendroglioma or an Astrocytoma based on the glioma overview in Figure 1.5. The diagnosis was confirmed by a pathological report of IDH mutation, an Astrocytoma, grade IV.

Chapter 5

Concluding remarks

5.1 Conclusions

The conclusions of this study encapsulate the comprehensive findings from the experiments and simulations conducted on 2HG. These findings contribute significantly to the understanding of 2HG's behavior in various environments and under different conditions, providing a foundation for further research and practical applications in medical and biochemical fields. Below are the key points derived from the study:

- The chemical shifts and its assigned protons in 2HG were presented in Table 4.1. The chemical shifts, δ, and the coupling constants, J, were adjusted for the spectra with Phosphate buffer solution with the Daisy simulation and were presented in Table 4.2.

- The Python-simulated spectra were displayed in Figure 4.4 and 4.5. The resolution and the peak splitting pattern in the simulated spectra were both good and accurate. Based on the comparison of the simulated 1D spectrum at 600 MHz and the experimental 1D spectrum at 600 MHz done in Figure 4.6 the simulations done by "nmrsim" were accurate. The simulation helped visualize how the magnetic field strength would affect the signal from 2HG.

- The optimized TE-time for 2HG at 4 ppm was with a spin echo sequence determined to be 90 ms at a magnetic field strength, B_0, of 600 MHz. While on a magnetic field strength of 60 MHz, the optimal TE-time for 2HG´s signal at 4 ppm was determined to be 100 ms. The results of these experiments, together with the observation of the basis sets and the 1D spectrum the coupling at 4.02 ppm were determined to be of higher order, as well as the signals at 2.26 ppm and 1.8 ppm.

- The optimized TE-time for 2HG at 2.26 ppm with a spin echo sequence was determined to be 130 ms at a field strength of 60 MHz and 110 ms at a field strength of 600 MHz. While the optimized TE-time for 2HG at 1.8 ppm with a spin echo sequence was determined to be 150 ms for a magnetic field of 60 MHz and 160 ms for a magnetic field of 600 MHz. The signals at 1.8 ppm are often seen in connection with the signals at 2.26 ppm and are rarely studied by themselves.

- The stability of 2HG in a brain metabolites solution was measured over 6 months. 2HG was based on the stability test determined to be stable in a brain metabolite solution with a

Plasma/Serum buffer with a pH of 7.4.

- All the calibration curves for both pure 2HG and 2HG in a brain metabolite solution showed good linearity, with $R^2 > 0.9$, indicating reliable methods for monitoring metabolite concentration changes.

- The circular geometry of the 3D printed phantom, particularly its smaller compartments, resulted in data from the 3 T GE scanner with excellent shimming. The filling mechanism using a syringe and the locking mechanism with electrical tape, along with the claw grip for attaching the ping pong balls, functioned effectively. The screwing mechanism with a silicone seal kept the phantom sealed for weeks. Additionally, the mechanism similar to a Peripheral Intravenous Catheter on top of the lid efficiently filled the last drops of solution into the phantom while allowing air to escape. After a week, pollution signals were found to originate from the ping pong balls, which will require a solution in further studies.

- The spectra accumulated by the short TE PRESS sequence at the 3 T GE scanner had poor signal-to-noise ratio and baselines after the alignment and averaging done in Osprey. The best spectrum of the 8 mM 2HG solution analyzed with a PRESS sequence with TE 35 ms where displayed in Figure 4.30, but because of the poor S/N ratio and baselines, the short TE PRESS spectra were not examined further.

- The spectra acquired with a sLaser sequence at the 3 T GE scanner exhibited good linewidth, 2, and excellent water suppression, 99%, resulting in generally high-quality spectra. However, due to the inapplicability of quantification with Osprey, the optimal quantification method for 2HG at a clinical 3 T GE scanner could not be determined, highlighting the need for a better analysis tool.

This study has successfully demonstrated the chemical shifts and coupling constants of 2HG, verified the accuracy of Python-simulated spectra, and optimized TE times for detecting 2HG signals at various ppm levels, pulse sequences, and magnetic field strengths at NNP given the parameters presented. The stability of 2HG in brain metabolite solutions and the reliability of calibration curves were confirmed, providing robust methods for future research. The 3D printed phantom´s design was validated for use on a 3 T GE scanner, although improvements are needed on the ping pong balls. Lastly, while data from the 3 T GE scanner presented challenges in quantification, the spectra from the sLaser sequence showed promise, highlighting the need for better analysis tools for further studies. These findings pave the way for enhanced detection and quantification of 2HG in biochemical research and clinical diagnostics.

5.2 Further work

- In this thesis, the optimal TE for spin echo, PRESS, and MEGA-PRESS sequences was determined for both high magnetic fields and 60 MHz. It would be interesting to explore how a MEGA-sLaser sequence would affect the signals from 2HG compared to the editing from a MEGA-PRESS sequence. Therefore, a MEGA-sLaser sequence should be developed and tested both at NNP for the 600 MHz and at HUS for the 3 T GE scanner.

- Regarding the disturbance signals from the ping pong balls in the phantom, further studies should explore solutions. Different ping pong balls from various suppliers should be tested. Additionally, rinsing the residue inside the ping pong balls with distilled water and buffer solution using a syringe should be attempted and then tested for disturbances. If neither of these methods proves effective, the ping pong balls would need to be replaced with an alternative container, possibly glass, to achieve a cleaner surface. If the ping pong balls are replaced, the grip mechanism would also need to be adapted to accommodate the new container.

- For the spectra acquired at the 3 T GE scanner, a new or improved analysis method needs to be implemented, primarily involving new basis sets for the different metabolites. The basis sets used in this thesis were obtained from the MRICloud website. In future studies, new basis sets should be created, either by simulating them with fid-a or another simulation tool, or by using experimental data. A basis set for the 3 T GE scanner could be developed from a range of samples with varying concentrations and sequences for each metabolite.

Bibliography

[1] Adiabatic excitation. https://mriquestions.com/adiabatic-excitation.html. Accecced: 25.05.2024.

[2] Adiabatic rf-pulses. https://mriquestions.com/adiabatic-pulses.html. Accecced: 25.05.2024.

[3] J. R. Alger, J. A. Frank, A. Bizzi, M. J. Fulham, B. X. DeSouza, M. O. Duhaney, S. W. Inscoe, J. L. Black, P. C. van Zijl, and C. T. Moonen. Metabolism of human gliomas: assessment with h-1 mr spectroscopy and f-18 fluorodeoxyglucose pet. *Radiology*, 177(3):633–41, 1990.

[4] P. Atkins and J. de Paula. *ELEMENTS of Physical Chemistry, 7th edition*. Oxford University Press, 2017.

[5] A. W. Autry, M. Lafontaine, L. Jalbert, E. Phillips, J. J. Phillips, J. Villanueva-Meyer, M. S. Berger, S. M. Chang, and Y. Li. Spectroscopic imaging of d-2-hydroxyglutarate and other metabolites in pre-surgical patients with idh-mutant lower-grade glioma. *Journal of Neuro-Oncology*, 159:43–52, 2022.

[6] D. Bal and A. Gryff-Keller. ^{1}h and ^{13}c nmr study of 2-hydroxyglutaric acid and its lactone. *Magnetic Resonance in Chemistry*, 40:533–536, 2002.

[7] A. Berrington, N. L. Voets, S. J. Larkin, N. de Pennington, J. Mccullagh, R. Stacey, C. J. Schofield, P. Jezzard, T. Clare, S. Cadoux-Hudson, P. Plaha, O. Ansorge, and U. E. Emir. A comparison of 2-hydroxyglutarate detection at 3 and 7 t with long-te semi-laser. *NMR in Biomedicine*, 311:e3886, 2018.

[8] N. Bertolino, C. Marchionni, F. Ghielmetti, B. Burns, G. Finocchiaro, E. Anghileri, M. G. Bruzzone, and L. Minati. Accuracy of 2-hydroxyglutarate quantification by short-echo proton-mrs at 3t: A phantom study. *European Journal of Medical Physics*, 2014.

[9] A. Bhandaril, C. Sharma, M. Ibrahim, M. Riggs, R. Jones, and A. Lasocki. The role of 2-hydroxyglutarate magnetic resonance spectroscopy for the determination of isocitrate dehydrogenase status in lower grade gliomas versus glioblastoma: a systematic review and meta-analysis of diagnostic test accuracy. *Neuroradiology*, 63:1823–1830, 2021.

[10] A. Bjørnerud. *The Physics of Magnetic Resonance Imaging*. Department of Physics, University of Oslo, 2008.

[11] F. Bloch, W. W. Hansen, and M. Packard. Nuclear induction. *Phys. Rev.*, 69:127–127, Feb 1946.

[12] M. A. Brown and R. C. Semelka. *MRI: Basic Principles and Applications, Third edition*. John Wiley and Sons, Inc., 2003.

[13] R. Chang and K. A. Goldsby. *GENERAL CHEMISTRY: THE ESSENTIAL CONCEPTS, SEVENTH EDITION*. McGraw-Hill Education, 2014.

[14] Chemdraw. http://www.perkinelmer.co.uk/category/chemdraw. Chemical Communication Software. Accecced: 06.02.2024.

[15] C. Choi, S. K. Ganji, R. J. DeBerardinis, K. J. Hatanpaa, D. Rakheja, Z. Kovacs, X.-L. Yang, T. Mashimo, J. M. Raisanen, I. Marin-Valencia, J. M. Pascual, C. J. Madden, B. E. Mickey, C. R. Malloy, R. M. Bachoo, and E. A. Maher. 2-hydroxyglutarate detection by magnetic resonance spectroscopy in subjects with idh-mutated gliomas. *nature medicine*, 2012.

[16] Craven, a. - github. https://github.com/alexcraven. Accecced: 25.04.2024.

[17] E. Derbyshire and R. Obeid. Choline, neurological development and brain function: A systematic review focusing on the first 1000 days. *Nutrients*, 12(6):1731, 2020.

[18] Merck life science as. dl-α-hydroxyglutaric acid disodium salt. https://www.sigmaaldrich.com/NO/en/product/sigma/94577, 2022.

[19] I. L. Fjermestad. Spectral editing of brain metabolites using weighted nuclear magnetic resonance. Master thesis, University of Bergen, 2019.

[20] Formlabs - clear resin v5. https://formlabs.com/eu/store/materials/clear-resin/. Accessed: 16.02.2024.

[21] Formlabs - form 3+. https://formlabs.com/eu/3d-printers/form-3/. Accessed: 16.02.2024.

[22] J. Frahm, H. Bruhn, M. L. Gyngell, K. D. Merboldt, W. Hänicke, and R. Sauter. Localized proton nmr spectroscopy in different regions of the human brain in vivo. relaxation times and concentrations of cerebral metabolites. *Magnetic resonance in medicine*, 11(1):47–63, 1989.

[23] M. Garwood and L. DelaBarre. The return of the frequency sweep: Designing adiabatic pulses for contemporary nmr. *Journal of Magnetic Resonance*, 153(2):155–177, 2001.

[24] GE Medical Systems, Milwaukee, WI, USA.

[25] V. Govindaraju, K. Young, and A. A. Maudsley. Proton nmr chemical shifts and coupling constants for brain metabolites. *NMR in Biomedicine*, 2000.

[26] M. Haris, K. Cai, A. Singh, H. Hariharan, and R. Reddy. In vivo mapping of brain myo-inositol. *NeuroImage*, 54(3):2079–2085, 2011.

[27] A. D. Harris, M. G. Saleh, and R. A. E. Edden. Edited ^1h magnetic resonance spectroscopy in vivo: Methods and metabolites. *Magnetic Resonance in Medicine*, 2017.

[28] C. Hull. Apparatus for production of three-dimensional object by stereolithography. *US Patent*, 4,575,330, 1986.

[29] J. D. Hunter. Matplotlib: A 2d graphics environment. *Computing in Science & Engineering*, 9(3):90–95, 2007.

[30] K. Hyeonjin, K. Sungjin, H. L. Hyeong, and H. Hwon. In-vivo proton magnetic resonance spectroscopy of 2-hydroxyglutarate in isocitrate dehydrogenase-mutated gliomas: A technical review for neuroradiologists. *Korean J Radiol*, 17(5):620–632, 2016.

[31] D. Juskanic, J. P. Mistinova, S. Holly, M. Sekeresova, K. Kolejak, and L. Patrivuc. Diagnositc performance of edited 2hg mr spectroscopy of central glioma in the clinical environment. *Magnetic Resonance Materials in Physics, Biology and Medisince*, 35:45–52, 2022.

[32] J. Kalinina, A. Carroll, L. Wang, Q. Yu, D. E. Mancheno, S. Wu, F. Liu, J. Ahn, M. He, H. Mao, and E. G. Van Meir. Detection of "oncometabolite" 2-hydroxyglutarate by magnetic resonance analysis as a biomarker of idh1/2 mutations in glioma. *J Mol Med*, 90:1161–1171, 2012.

[33] J. Keeler. *Understanding NMR Spectroscopy*. John Wiley and Sons, Ltd, 2012.

[34] P. Lauterbur. Image formation by induced local interactions: Examples employing nuclear magnetic resonance. *Nature*, 242:190–191, 1973.

[35] Lcmodel. http://lcmodel.ca/lcmodel.shtml. Accecced: 11.04.2024.

[36] Lcmodel download - github. https://github.com/schorschinho/LCModel. Accecced: 11.04.2024.

[37] Logo - haukeland university hospital. https://www.helse-bergen.no/48f7bb/contentassets/61d2801beef644ae9284c03cdda5551a/haukelanduniversitetssjukehus_rgb_pos.png, 2023. Accecced: 06.02.2024.

[38] Logo - university in bergen. https://manual.uib.no/files/2023/01/logo2023_eng.png, 2023. Accecced: 06.02.2024.

[39] A. Louis, David N. aand Perry, P. Wesseling, D. J. Brat, I. A Cree, D. Figarella-Branger, C. Hawkins, H. K. Ng, S. M. Pfister, G. Reifenberger, R. Soffietti, A. von Deimling, and D. W. Ellison. The 2021 who classification of tumors of the central nervous system: a summary. *Neuro-Oncology, Volume 23, Issue 8, Pages 1231–1251*, 2021.

[40] A. W. Malgorzata. *Characterizing mass transport in hydrogels using Nuclear Magnetic Resonance*. PhD thesis, Univeristy of Bergen, 2019.

[41] Matlabr2024a. https://matlab.mathworks.com. Accecced: 11.04.2024.

[42] Mricloud. https://braingps.mricloud.org/home. Accecced: 11.04.2024.

[43] Periodic table of elements. https://pubchem.ncbi.nlm.nih.gov/ptable/, 2024. Accecced: 03.02.2024.

[44] U. Neuberger, P. Kickingereder, X. Helluy, M. Fischer, M. Bendszus, and S. Heiland. Accuracy of 1h magnetic resonance spectroscopy for quantification of 2-hydroxyglutarate using linear combination and j-difference editing at 9.4 t. *Z. Med. Phys.*, 27:300–309, 2017.

[45] T. B. Nguyen, G. Melkus, M. Taccone, I. D. Moldovan, D. Ghinda, R. Gotfrit, C. H. Torres, N. Zakhari, S. Chakraborty, J. Woulfe, G. Jansen, M. D. F. McInnes, R. E. Thornhill, I. Cameron, and F. AlKherayf. Preoperative determination of isocitrate dehydrogenase mutation in gliomas using spectral editing mrs: A prospective study. *J. MAGN. RESON. IMAGING*, 53:416–426, 2021.

[46] Nmr spektrometers at uib. https://www.uib.no/en/kj/94587/nmr-spektrometers-uib#500-mhz. Accecced: 25.05.2024.

[47] Nnp - norwegian nmr platform. imagemapster. https://nmr.h.uib.no/index.php/blog/facebook-page/2-uncategorised/9-test-av-imagemapster, 2017. Accecced: 06.02.2024.

[48] Numpy documentation. https://numpy.org/doc/stable/. Accecced: 03.05.2024.

[49] G. Oeltzschner, H. J. Zöllner, S. C. N. Hui, M. Mikkelsen, M. G. Saleh, S. Tapper, and R. A. E. Edden. Osprey: Open-source processing, reconstruction and estimation of magnetic resonance spectroscopy data. *Journal of Neuroscience Methods*, 343:108827, 2020.

[50] G. H. J. Park, S.-H. Yang, and H.-M. Baek. 900mhz 1h-/13c-nmr analysis of 2-hydroxyglutarate and other brain metabolitesin human brain tumor tissue extracts. *PLoS ONE*, 13(9): e0203379, 2018.

[51] Pascal´s triangle. https://chem.libretexts.org/Bookshelves/Physical_and_Theoretical_Chemistry_Textbook_Maps/Supplemental_Modules_(Physical_and_Theoretical_Chemistry)/Spectroscopy/Magnetic_Resonance_Spectroscopies/Nuclear_Magnetic_Resonance/NMR%3A_Experimental/NMR_-_Interpretation/Pascals_Triangle, 2021. Accecced: 06.03.2024.

[52] Phosphate buffer (ph 5.8 to 7.4) preparation and recipe. https://www.aatbio.com/resources/buffer-preparations-and-recipes/phosphate-buffer-ph-5-8-to-7-4, 2024. Accecced: 19.10.2023.

[53] W. B. Pope, R. M. Prins, M. A. Thomas, R. Nagarajan, K. E. Yen, M. A. Bittinger, N. Salamon, A. P. Chou, W. H. Yong, H. Soto, N. Wilson, E. Driggers, H. G. Jang, S. M. Su, D. P. Schenkein, A. Lai, T. F. Cloughesy, H. I. Kornblum, H. Wu, V. R. Fantin, and L. M. Liau. Non-invasive detection of 2-hydroxyglutarate and other metabolites in idh1 mutant glioma patients using magnetic resonance spectroscopy. *J Neurooncol*, 107:197–205, 2012.

[54] W. G. Proctor and F. C. Yu. The dependence of a nuclear magnetic resonance frequency upon chemical compound. *Phys. Rev.*, 77:717–717, Mar 1950.

[55] Proton gyromagnetic ratio. https://physics.nist.gov/cgi-bin/cuu/Value?gammap. Accecced: 22.05.24.

[56] Pubchem compound summary for cid 43, 2-hydroxyglutaric acid. https://pubchem.ncbi.nlm.nih.gov/compound/2-Hydroxyglutaric-acid, 2024. Accecced: 26.04.2024.

[57] E. M. Purcell, H. C. Torrey, and R. V. Pound. Resonance absorption by nuclear magnetic moments in a solid. *Phys. Rev.*, 69:37–38, Jan 1946.

[58] I. I. Rabi, J. R. Zacharias, S. Millman, and P. Kusch. A new method of measuring nuclear magnetic moment. *Phys. Rev.*, 53:318–318, Feb 1938.

[59] S. Ramin, W. Tognola, and A. Spotti. Proton magnetic resonance spectroscopy: Clinical applications in patients with brain lesions. *São Paulo medical journal = Revista paulista de medicina*, 121:254–9, 12 2003.

[60] G. S. Rule and T. K. Hitchens. *Fundamentals of Protein NMR Spectroscopy*. Springer, 2006.

[61] G. M. Sametz. Nmrsim's documentation - github. https://nmrsim.readthedocs.io/en/latest/index.html, 2023.

[62] Z. Shams, W. J. M. van der Kemp, U. Emir, J. W. Dannkbaar, T. J. Snijders, F. Y. F. de Vos, D. W. Klomp, J. P. Wijnen, and E. C. Wiegers. Comparison of 2-hydroxyglutarate detection with slaser and mega-slaser at 7t. *Front. Neurol.*, 12:718423, 2021.

[63] M. Svensen. Quantitative diffusion-weighted j-difference spectroscopy of common brain metabolites. Master thesis, University of Bergen, 2021.

[64] H. N. Sørgård. *Wetting in Porous Media: A Nuclear Magnetic Resonance Study*. PhD thesis, Univeristy of Bergen, 2020.

[65] The nobel prize in physics 1952. https://www.nobelprize.org/prizes/physics/1952/summary/. Accecced: 22.04.2024.

[66] The nobel prize in physiology or medicine 2003. https://www.nobelprize.org/prizes/medicine/2003/summary/. Accecced: 31.05.2024.

[67] I. Tkác, Z. Starcuk, I. Y. Choi, and R. Gruetter. In vivo ^{1}h nmr spectroscopy of rat brain at 1ms echo time. *Magnetic Resonance in Medicine 41:649–656*, 1999.

[68] Topspin 4.3.0. https://www.bruker.com/en/products-and-solutions/mr/nmr-software/topspin.html. Accecced: 05.03.2023.

[69] M. Whitaker. The history of 3d printing in healthcare. *The Bulletin of the Royal College of Surgeons of England*, 96(7):228–229, 2014.

Appendix A

Python 1D NMR simulation script

```
pip install nmrsim

import numpy as np
import matplotlib as mpl

from nmrsim import SpinSystem

import matplotlib.pyplot as plt
from nmrsim.plt import mplplot

#Figure size
mpl.rcParams['figure.dpi']= 150
%matplotlib notebook

#Function: ppm_to_hz
#Given a chemical shift in ppm and spectrometer frequency in MHz
def ppm_to_hz(ppm, spec_freq):
#return the corresponding chemical shift in Hz.
    return [d * spec_freq for d in ppm]

#Set the frequency in MHz:
basic_freq = 600

#The chemical shifts for 2HG in ppm:
ppm = [3.9275, 1.7478, 1.9036, 2.1448, 2.1939]

#The ppm_to_hz function returning the corresponding chemical shifts
#from ppm to Hz based on the set frequency
v_two_hg = ppm_to_hz(ppm, basic_freq)
```

```
#Function: two_hg
def two_hg():
    #chemical shifts for 2HG times the frequency
    #in the magnetic field.
    v = np.array(v_two_hg)
    #coupling constants, J-values, taken from
    #the daisy-simulation based on Bal et al.
    J = np.zeros((5, 5))
    J[0, 1] = 7.6505
    J[0, 2] = 4.0492
    J[1, 2] = -14.01
    J[1, 3] = 5.2552
    J[1, 4] = 10.6635
    J[2, 3] = 10.8554
    J[2, 4] = 5.8620
    J[3, 4] = -14.95
    J = J + J.T
    return v, J
#The two_hg function returning the chemical shifts and the J-values
v, J = two_hg()

#Print the frequencies in Hz
print('v: ', v)
#Print a Matrix of the coupling constants
print('J: \n', J)


#Defining the SpinSystem of 2HG
two_hg_system = SpinSystem(v, J)

#printing the peaklist for 2HG
two_hg_system.peaklist()


#defining that the spin system for 2HG is of second order
two_hg_system.second_order = True

#defining the min and max values in the x-axis.
left = max(ppm)*basic_freq+35
right = min(ppm)*basic_freq-35

#Defining the desired title, x label and y label in the figure
plt.title('1D 2HG spectrum at 600MHz')
plt.xlabel('Chemical Shift (ppm*600MHz)')
plt.ylabel('Intensity')
```

```
#Plotting the peaksystem for 2HG
fig = mplplot(two_hg_system.peaklist(), y_max=0.25, w=1.0,
points=16384, limits=(left,right));

#Save the figure to the computer
plt.savefig('2HG_spectrum_600MHz.png', dpi=300)
```

Appendix B

The spin echo sequence script used at the 600 MHz Bruker BioSpin

```
;enkelt spinn ekko
;avance-version (00/02/07)


#include <Avance.incl>


"p2=p1*2"

"d11=30m"


1 ze
2 30m
  d1
  p1 ph1
  d20
  p2 ph2
  d20
  go=2 ph31
  d11 mc #0 to 2 F0(zd)
exit


ph1=0 0 2 2 1 1 3 3
ph2=1 3 1 3 0 2 0 2
ph31=0 0 2 2 1 1 3 3


;pl1 : f1 channel - power level for pulse (default)
;p1 : f1 channel -  90 degree high power pulse
```

```
;p2 : f1 channel - 180 degree high power pulse
;d1 : relaxation delay; 1-5 * T1
;d11: delay for disk I/O                              [30 msec]
;d20: fixed echo time to allow elimination of diffusion
;     and J-mod. effects
;NS: 8 * n
;DS: 16


;d20: d20 should be << 1/J ,but > (50 * P2)
```

Appendix C

Complex tables

C.1 Optimal TE tables for 2HG

Table for the optimal TE times for 2HG at 4.02 ppm.

	4.02 ppm			
		Normalized		Normalized
Echo time:	600 MHz	600 MHz	60 MHz	60 MHz
10	7,61689E+11	1	488337,6	1
20	7,25531E+11	0,952529129	407324,21	0,83410372
30	5,13057E+11	0,673578706	192832,26	0,3948749
40	4,05766E+11	0,532718733	130423,7	0,26707692
50	1,88889E+11	0,247986956	100053,07	0,20488504
60	69780512768	0,091612873	-27762,73	-0,0568515
70	-75051040768	-0,098532401	-112289,15	-0,2299416
80	-1,32724E+11	-0,174249648	-197330,82	-0,4040869
90	-1,72592E+11	-0,22659105	-205931,9	-0,4216999
100	-1,45961E+11	-0,191628405	-235705,55	-0,4826693
110	-92881870848	-0,121941996	-210498,93	-0,4310521
120	-20384980992	-0,026762868	-192653,84	-0,3945095
130	75028619264	0,098502964	-138681,37	-0,2839867
140	1,46161E+11	0,191890925	-93765,13	-0,1920088
150	2,07556E+11	0,272494491	-35889,31	-0,0734928
160	2,27102E+11	0,298155398	-13245,26	-0,0271232
170	2,02278E+11	0,265564994	-1171,69	-0,0023993
180	1,37077E+11	0,17996517	11942,95	0,02445634
190	33793122304	0,04436604	-73198,44	-0,1498931
200	-92722806784	-0,121733165	-91511,4	-0,1873937

Table for the optimal TE times for 2HG at 2.26 ppm.

	2.26 ppm			
		Normalized		Normalized
Echo time:	600 MHz	600 MHz	60 MHz	60 MHz
10	2,32763E+12	1	2168754,86	1
20	1,13688E+12	0,488428685	1922738,64	0,88656338
30	2896109568	0,001244232	1373560,58	0,63334063
40	-4,26234E+11	-0,18311964	430191,88	0,19835892
50	-73704194048	-0,031664945	-283822,58	-0,1308689
60	3,48915E+11	0,149901411	-646637,76	-0,2981608
70	3,27371E+11	0,140645651	-641088,99	-0,2956023
80	41019375616	0,017622827	-577268,1	-0,2661749
90	72545222656	0,031167026	-465116,08	-0,2144623
100	6,84354E+11	0,294013495	-286356,1	-0,1320371
110	1,1088E+12	0,476366089	-103235,49	-0,0476013
120	8,90913E+11	0,382755954	17092,72	0,00788135
130	5,3101E+11	0,228133753	50746,46	0,02339889
140	87806238720	0,037723494	37577,64	0,01732683
150	-4,8365E+11	-0,207786853	-13957,97	-0,0064359
160	-5,27436E+11	-0,226598165	-122643,99	-0,0565504
170	1,3298E+11	0,057131038	-215633,16	-0,0994272
180	8,38717E+11	0,360331505	-171671,99	-0,0791569
190	1,19172E+12	0,511988062	-95187,42	-0,0438904
200	1,14406E+12	0,491513959	-66755,03	-0,0307803

Table for the optimal TE times for 2HG at 1.8 ppm.

	2.0 ppm + 1.8 ppm			
		Normalized		Normalized
Echo time:	600 MHz	600 MHz	60MHz	60 MHz
10	2,02194E+12	1	1417727,61	1
20	1,06505E+12	0,526746208	1398886,01	0,98671
30	2,95602E+11	0,146197405	739678,55	0,52173531
40	-68467662848	-0,033862406	65638,52	0,0462984
50	-27090681856	-0,013398379	-337857,72	-0,2383093
60	2,07706E+11	0,102726376	-455437,23	-0,3212445
70	63315755008	0,031314401	-420786,09	-0,2968032
80	-73896919040	-0,036547582	-405505,72	-0,2860251
90	-60732637184	-0,030036855	-303624,76	-0,214163
100	-1,02562E+11	-0,050724812	-228402,05	-0,1611043
110	-15743614976	-0,007786401	-119309,09	-0,0841552
120	-4,41139E+11	-0,218176161	-37773,6	-0,0266438
130	-3,32285E+11	-0,164339889	100977,35	0,07122479
140	-2,44729E+11	-0,121037016	218544,73	0,15415142
150	82365857792	0,040736109	275167,32	0,1940904
160	3,4932E+11	0,172764792	220468,17	0,15550813
170	2,44821E+11	0,121082268	189334,79	0,13354807
180	-1,12701E+11	-0,055739079	138812,77	0,09791216
190	-2,9143E+11	-0,144133816	-28824,11	-0,0203312
200	-2,55602E+11	-0,126414497	-227949,51	-0,1607851

C.2 Optimal TE tables for 2HG and Glu at 60 MHz

Table for the optimal TE times for 2HG and Glu around 4 ppm.

			around 4 ppm			
			absolute values		normalized values	
Spectrum number	Pulse sequence	TE	Glu	2HG	Glu	2HG
1	spin echo	10	111086,85	488337,6	1	1
2	spin echo	20	52376,81	407324,21	0,471494241	0,834103723
3	spin echo	30	39367,24	192832,26	0,354382539	0,394874898
4	spin echo	40	42679,41	130423,7	0,38419858	0,267076916
5	spin echo	50	32109,97	100053,07	0,289052845	0,204885043
6	spin echo	60	7569,48	-27762,73	0,068140198	-0,05685151
7	spin echo	70	11944,2	-112289,15	0,107521277	-0,229941643
8	spin echo	80	-2276,18	-197330,82	-0,020490094	-0,404086886
9	spin echo	90	16846,34	-205931,9	0,151650173	-0,421699865
10	spin echo	100	17674	-235705,55	0,15910074	-0,482669264
11	spin echo	110	14247,63	-210498,93	0,128256675	-0,431052063
12	spin echo	120	12499,59	-192653,84	0,112520879	-0,394509536
13	spin echo	130	25716,06	-138681,37	0,231495087	-0,283986672
14	spin echo	140	34381,16	-93765,13	0,309498019	-0,192008827
15	spin echo	150	32852,24	-35889,31	0,295734734	-0,073492825
16	spin echo	160	54235,07	-13245,26	0,488222233	-0,027123162
17	spin echo	170	51323,94	-1171,69	0,462016341	-0,002399344
18	spin echo	180	49986,26	11942,95	0,449974592	0,024456339
19	spin echo	190	42849,84	-73198,44	0,385732785	-0,149893107
20	spin echo	200	31072,56	-91511,4	0,279714116	-0,187393721

Table for the optimal TE times for 2HG and Glu around 2.3 ppm.

			around 2.3 ppm			
			absolute values		normalized values	
Spectrum number	Pulse sequence	TE	Glu	2HG	Glu	2HG
1	spin echo	10	350747,06	2168754,86	1	1
2	spin echo	20	345594,73	1922738,64	0,985310411	0,88656338
3	spin echo	30	281918,16	1373560,58	0,803764856	0,633340635
4	spin echo	40	175789,47	430191,88	0,501185869	0,198358924
5	spin echo	50	47368,96	-283822,58	0,135051624	-0,130868908
6	spin echo	60	-8883,65	-646637,76	-0,025327796	-0,298160835
7	spin echo	70	-34487,39	-641088,99	-0,098325528	-0,29560233
8	spin echo	80	-35407,91	-577268,1	-0,100949984	-0,266174896
9	spin echo	90	-14977,57	-465116,08	-0,042701912	-0,214462265
10	spin echo	100	12599,65	-286356,1	0,035922325	-0,132037099
11	spin echo	110	36995,01	-103235,49	0,105474897	-0,047601272
12	spin echo	120	46648,58	17092,72	0,132997779	0,007881352
13	spin echo	130	53245,87	50746,46	0,151807032	0,023398892
14	spin echo	140	55960,96	37577,64	0,159547909	0,017326827
15	spin echo	150	34281,8	-13957,97	0,097739379	-0,006435937
16	spin echo	160	21136,71	-122643,99	0,060261973	-0,056550416
17	spin echo	170	823,46	-215633,16	0,002347732	-0,099427171
18	spin echo	180	-14512,36	-171671,99	-0,041375571	-0,079156936
19	spin echo	190	-20689,75	-95187,42	-0,058987665	-0,043890355
20	spin echo	200	-6327,25	-66755,03	-0,018039353	-0,030780348

Table for the optimal TE times for 2HG and Glu around 2 ppm.

			around 2 ppm			
			absolute values		normalized values	
Spectrum number	Pulse sequence	TE	Glu	2HG	Glu	2HG
1	spin echo	10	224511,13	1417727,61	1	1
2	spin echo	20	221460,43	1398886,01	0,98641181	0,98671
3	spin echo	30	163925,45	739678,55	0,73014398	0,521735307
4	spin echo	40	72057,32	65638,52	0,320952106	0,0462984
5	spin echo	50	20402,49	-337857,72	0,090875183	-0,238309332
6	spin echo	60	-13905,19	-455437,23	-0,061935415	-0,321244523
7	spin echo	70	-30055,42	-420786,09	-0,133870512	-0,296803199
8	spin echo	80	-33639,21	-405505,72	-0,149833151	-0,286025127
9	spin echo	90	-41924,18	-303624,76	-0,186735419	-0,214162973
10	spin echo	100	-51534,18	-228402,05	-0,229539533	-0,161104325
11	spin echo	110	-61466,24	-119309,09	-0,273778142	-0,084155157
12	spin echo	120	-59962,64	-37773,6	-0,267080924	-0,026643764
13	spin echo	130	-61966,64	100977,35	-0,276006985	0,071224789
14	spin echo	140	-51374,97	218544,73	-0,228830393	0,154151424
15	spin echo	150	-36249,49	275167,32	-0,161459657	0,194090401
16	spin echo	160	-3544,96	220468,17	-0,015789685	0,15550813
17	spin echo	170	16578,64	189334,79	0,073843288	0,133548073
18	spin echo	180	19331,1	138812,77	0,086103081	0,097912158
19	spin echo	190	31394,85	-28824,11	0,139836497	-0,020331205
20	spin echo	200	36201,41	-227949,51	0,161245503	-0,160785124

C.3 Calibration curve table for pure 2HG

Concentration/Echo time	68 ms	74 ms	80 ms	97 ms
10 mM	717978,29	758419,98	816058,21	830631,02
8 mM	597366,25	630451,12	666310,44	677694,5
6 mM	457789,34	474505,59	527064,69	490383,72
4 mM	300216,55	335349,69	335546,5	366447,62
2 mM	153756,44	175988,62	160399,69	179932,88
0 mM	0	0	0	0

C.4 Calibration curve table for 2HG in BRAINO

Concentration/Echo time	68 ms	74 ms	80 ms	97 ms
10 mM	792172,41	838482,93	849440,21	846233,14
8 mM	648769,16	661823,94	694853,78	674274,33
6 mM	502752,43	539049,08	555394,85	551131,75
4 mM	309051,86	327235,83	341018,3	353407,92
2 mM	194665,62	208196,11	211528,88	225566,17
0 mM	0	0	0	0

Appendix D

Complex figures

D.1 MEGA-PRESS spectrum for ON, OFF, and edited sequence

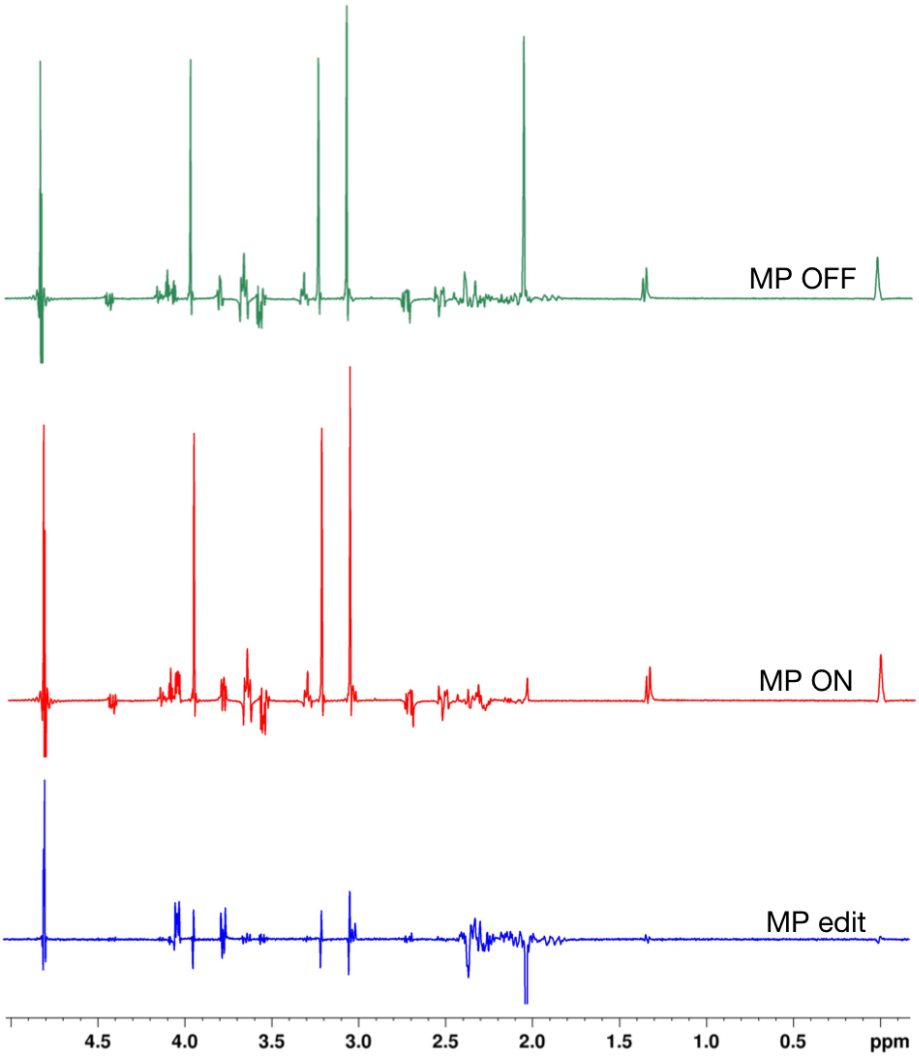

D.2 Plot of SI vs TE for edited 2HG at 4.02 ppm

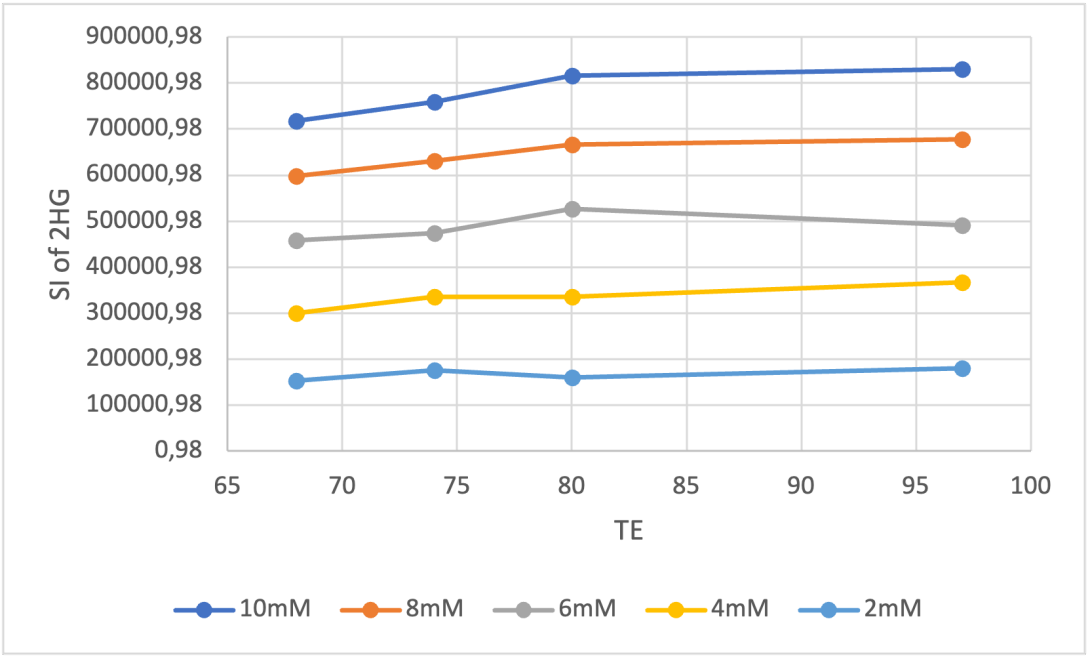

(a)

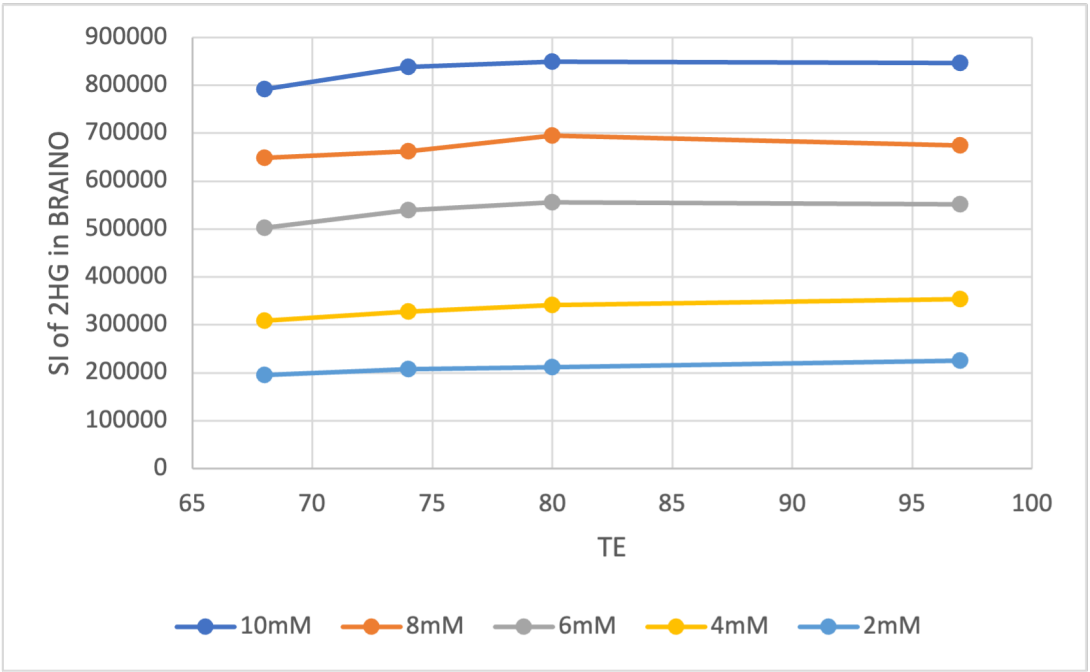

(b)

D.3 The voxel placement inside the large phantom and the ping pong balls

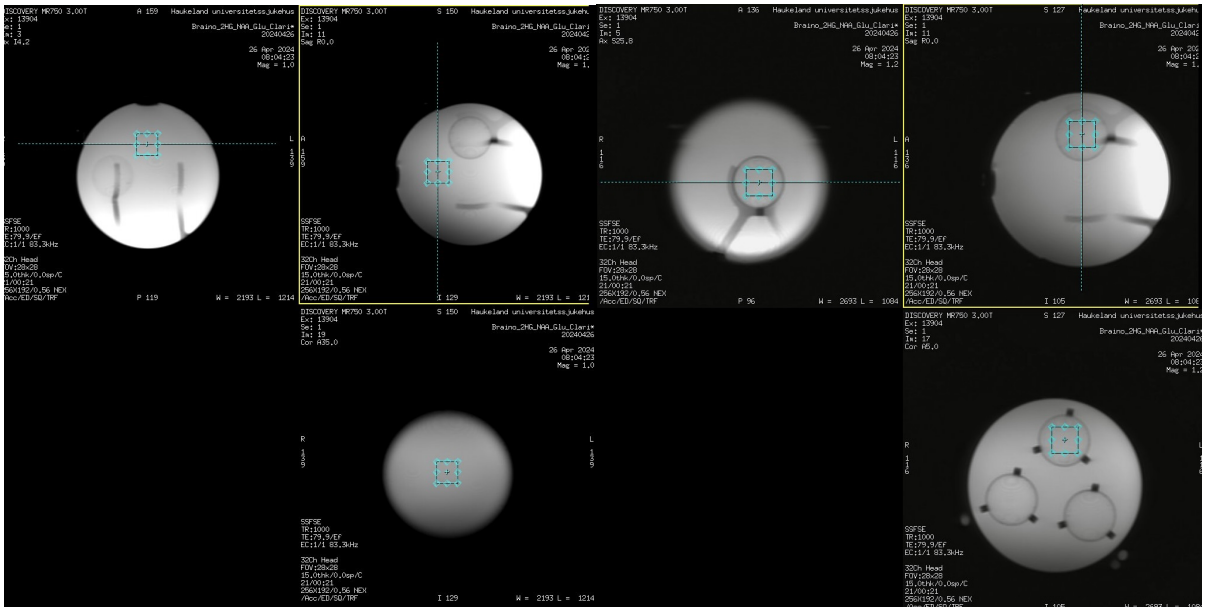

(a)

(b)

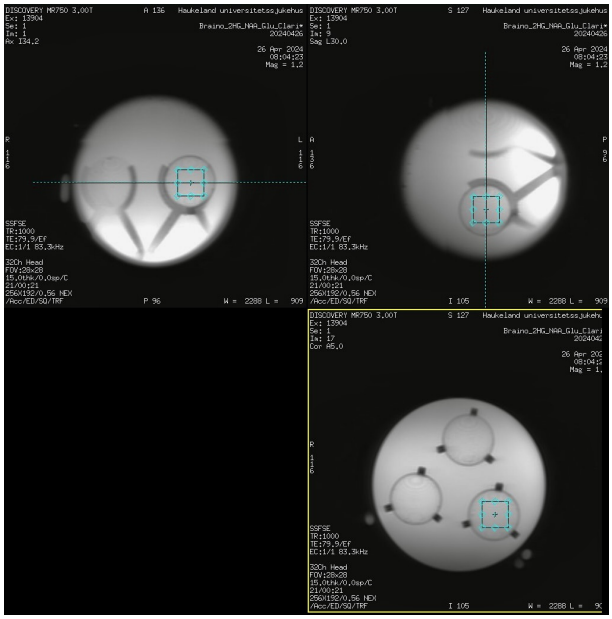

(c)

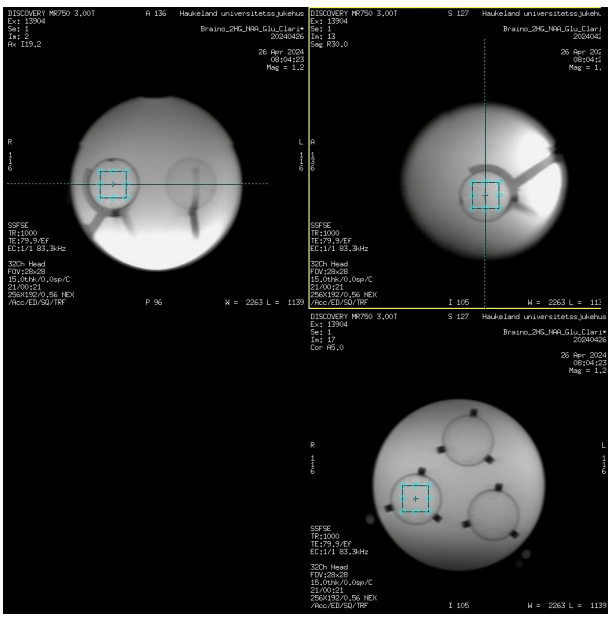

(d)

Appendix E

Poster - MMIV Conference, Dec. 2023

The following poster was presented at the MMIV Conference in December 2023.

Optimizing spectral parameters for quantification of 2-hydroxyglutarate

We have measured the spectrum of 2-hydroxyglutarate, examining the complex J-coupling patterns, and how they are influenced by varying echo time and magnetic field strength.

Celine Skramstad, John Georg Seland
University of Bergen

ABSTRACT

In recent years non-invasive detection of 2-hydroxyglutarate (2HG) with ^{1}H-MRS has shown to be a promising approach for differentiating IDH mutant and wild-type brain tumors [1-3]. However, there is no consensus with respect to optimal choice of pulse sequence, spectral editing, and corresponding echo times for optimal quantification of 2HG. In addition, the impact from higher order J-couplings varies with the magnetic field strength, which must be considered when choosing the optimal parameters. In this study we have measured the spectrum of 2HG phantoms at different magnetic field strength (1.4 T and 14.1 T). This enables a thorough investigation of the complex J-coupling patterns, how they are influenced by varying echo time and magnetic field strength, and how this can be applied to choose the optimal ^{1}H-MRS method for quantifying 2HG, and aid in determining proper basis sets for spectral fitting.

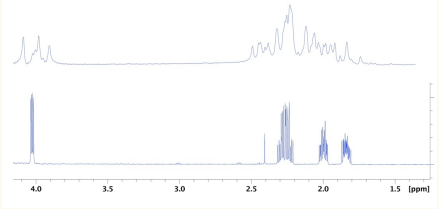

Figure 2: spectra of 2HG at 14.1 T (bottom) and 1.4 T (top)

THEORY

Reliable detection and quantification of 2HG using ^{1}H-MRS is challenging, due to the compound's MR-spectrum that consist of five non-interchangeable protons at 4.02 ppm, 2.27 ppm, 2.22 ppm, 1.98 ppm and 1.83 ppm, with complex higher-order J-coupling patterns, and strong overlap with signals from other brain metabolites. Higher-order J-coupling patterns occur when the difference in chemical shift between coupled protons ($\Delta\nu$) is of the same order as the strength of the J-couplings. This is particularly the case for the coupled signals in the area between 2.4and 1.8 ppm, where $\Delta\nu$ is maximum 30 Hz and 300 Hz at respectively 1.4 T and 14.1 T, while the J-coupling constants are around 5-10 Hz.

METHODS

All phantom solutions consist of 2HG dissolved in phosphate buffer (pH = 4.7) made from D_2O. Experiments were performed using the instruments shown in Figure 1. Simple spin echo experiments with no spatial encoding, and echo spacing varying between 10 and 130 ms, were used on both instruments.

Figure 1: The spectrometers used in this study. Nanalysis 1.4 T (60 MHz) benchtop NMR spectrometer (left). Bruker AVANCE NEO 14.1 T (600 MHz) vertical bore NMR spectrometer (right). 5 mm (o.d.) tubes with a sample volume of 0.6 mL are used on both spectrometers.

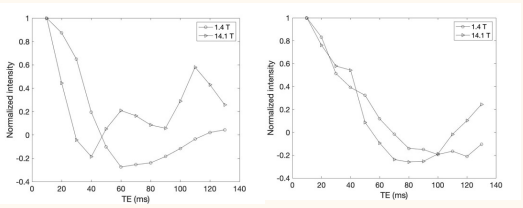

Figure 3: signal intensities (area) for the peaks centered at 2.3 ppm (left) and 4.02 ppm (right) obtained at different echo times (TE).

RESULTS

As expected, there is a clear difference in spectral resolution and peak width when comparing 2HG spectra (Figure 2) obtained at 1.4 T and 14.1 T. Furthermore, the influence from J-modulation with varying TE (Figure 3) is not the same at the two field strengths. For the peak centered at 2.3 ppm, often used in non-edited MRS at short (35 ms) or long (110 ms) TE's, the initial signal intensity decreases faster at 14.1 , and the signal maximum (for long TE) also occur at shorter TE-values (110 ms @ 14.1 T compared to 130-140 ms @ 1.4 T). For the peak centered at 4.02 ppm the J-modulation curves are more alike, as expected for the proton that has a larger separation in chemical shift ($\Delta\nu$) compared to the coupling constant. However, also here the minimum and maximum intensity with respect to TE are different.

In future studies these experimental data will be compared to simulations of spectral intensities at varying TE's.

REFERENCES
[1] Choi C, Raisanen JM, Ganji SK, Zhang S, et al. J Clin Oncol, 2016;34(33):4030–9.
[2] Andronesi OC, Loebel F, Bogner W, et al. Clin Cancer Res, 2016;22(7):1632–41.
[3] Jafari-Khouzani K, Loebel F, Bogner W, et al. Neuro-oncology, 2016;18(11):1569–78.
[4] Shams Z, van der Kemp WJM, Emir U, et al. Frontiers Neurology, 2021;12: 718423.
[5] Prener M, Opheim G, Shams Z, et al. Diagnostics, 2023; 13: 1805.

ACKNOWLEDGEMENTS
This work was partly supported by the Research Council of Norway through the Norwegian NMR Platform, NNP (226244/F50).

John.Seland@uib.no

UNIVERSITY OF BERGEN